Winter 2015

Characterization and mechanical properties of solar grade silicon in granular and nanopowder form

Mohamad Bilal Zbib
Purdue University

Graduate School Form 30
(Revised 08/14)

PURDUE UNIVERSITY
GRADUATE SCHOOL
Thesis/Dissertation Acceptance

This is to certify that the thesis/dissertation prepared

By Mohamad Bilal Zbib

Entitled
CHARACTERIZATION AND MECHANICAL PROPERTIES OF SOLAR GRADE SILICON IN GRANULAR AND NANOPOWDER FORM

For the degree of Doctor of Philosophy

Is approved by the final examining committee:

David F. Bahr

Carlos J. Martinez

Steven Son

Volkan Ortalan

To the best of my knowledge and as understood by the student in the Thesis/Dissertation Agreement, Publication Delay, and Certification/Disclaimer (Graduate School Form 32), this thesis/dissertation adheres to the provisions of Purdue University's "Policy on Integrity in Research" and the use of copyrighted material.

David F. Bahr

Approved by Major Professor(s): _____

_____

Approved by: David F. Bahr 02/10/2015

Head of the Department Graduate Program Date

CHARACTERIZATION AND MECHANICAL PROPERTIES OF SOLAR GRADE SILICON IN GRANULAR AND NANOPOWDER FORM

A Dissertation

Submitted to the Faculty

of

Purdue University

by

Mohamad B. Zbib

In Partial Fulfillment of the

Requirements for the Degree

of

Doctor of Philosophy

May 2015

Purdue University

West Lafayette, Indiana

I dedicate this dissertation to: Bilal, Wafaa, Farah, Mustapha, Hassan, and Lina

To Mira

To Lebanon

أهدي هذه الأطروحة إلى عائلتي: بلال, وفاء, فرح, مصطفى, حسان ولينا

إلى ميرا

إلى لبنان

ACKNOWLEDGEMENTS

I would like to thank everyone who helped in this work to make it successful especially my adviser Professor David F. Bahr that has been very supportive for me during my Ph.D. studies in the past few years. He helped me in building my own research path and getting a stronger personality through my research and academic routes. All the suggestions, discussions, and guidance that I have had from Prof. Bahr are the biggest encouragement for me to be a successful graduate student. I also would like to thank my Ph.D. committee members at Purdue University Professors Steven Son, Carlos Martinez, and Volkan Ortalan, and at Washington State University, Professors David Field and Grant Norton for their valuable comments and helpful experimental work that I gained from their laboratories and their graduate students.

I also would like to thank Wayne Osborne and Mathew Miller at REC Silicon for the great help, discussions and the financial support during my first couple years of my Ph.D. Special thanks for the entire faculty, staff, graduate and undergraduate students who contributed in helping me at Purdue University and Washington State University.

Very special thanks to my parents and my beloved ones that made my life easier in getting my Ph.D. degree.

Further acknowledgment goes to the great community at Pullman, WA and West Lafayette, IN.

TABLE OF CONTENTS

Page

Page

LIST OF TABLES

LIST OF FIGURES

Figure Page

Figure Page

Figure Page

Figure Page

Figure Page

ABSTRACT

Zbib, Mohamad B. Ph.D., Purdue University, May 2015. Characterization and Mechanical Properties of Solar Grade Silicon in Granular and Nanopowder Form. Major Professor: David F. Bahr.

Polycrystalline silicon is mainly used for solar cell applications, structures in micro-electromechanical systems, and production of single crystal Si. One of the relatively new methods for producing large quantities of polysilicon is fluidized bed reactor (FBR), where two main morphologies are produced, granular solid (1-3 mm) and nanopowders (30-300 nm). Grinding and fracture occurs in the granular solid during shipping and handling which can affect the final product properties and create safety issues. The microstructure and the morphology of both the granular and the nanopowder forms of Si were examined using scanning and transmission electron microscopes (SEM and TEM).The fracture toughness of the granular silicon was studied, using microindentation and nanoindentation techniques, at different annealing processes, and with different hydrogen concentrations during production. Hydrogen defects in silicon were analyzed using infrared spectroscopy to develop a new relationship between hydrogen and toughness. Based on the microstructural analysis it was shown that the granular Si are mostly crystalline with some amorphous regions linked to small pores, while the nanopowders are mostly amorphous with some crystalline bits; the porosity in the granular Si ranges between 1-4 volume percentage. It was proposed that the primary

mechanism in FBR for the granular Si formation is chemical vapor deposition with minor agglomeration associated with pores. It was found that the lower the hydrogen in the production, the higher the fracture toughness where it can be improved up to 45% (from 0.6 to 0.86 $MPa.m^{0.5}$), and lead for less dust during physical contact. New attrition parameters were proposed in order to better understand the fracture mechanisms of Si granules and other brittle microspheres. These parameters provide a relationship between the mechanical properties (indentation techniques), fracture behavior and failure mechanisms using both crushing tests and impact tests. Part of this thesis also focused on making a beneficial use of the Si nanopowders that are considered secondary products from FBR. The powders were processed into metal-coated carbon composites, using electroplating to improve electrical resistivity. This method can be used to enhance light trapping of solar cells in coated composites.

CHAPTER 1. INTRODUCTION

Polycrystalline silicon is used for solar cell applications, production of single crystal silicon, and structures in micro-electro-mechanical systems (MEMS). To produce large quantities of silicon, chemical vapor deposition (CVD) is used by growing silicon solids from the decomposition of trichlorosilane ($SiHCl_3$) or silane (SiH_4) gas. A relatively new method that has been used to produce silicon, for high demand for photovoltaic materials, is fluidized bed reactor (FBR) process [1]. The FBR process has advantages compared to the traditional Siemens process, because it has a lower cost, is more productive, and is less energy intensive. However, FBR silicon has small pores (on the order of 5 μm) that are not present in Siemens process which produce pore-free materials. In general, solar silicon products can tolerate slightly higher impurities compared to electronic grade because of the melting process that occurs after production. Typical FBR plants can produce up to 13,500 tons of high purity polysilicon per year.

The FBR process produces silicon in hydrogen rich environment with isothermal beds. Two main morphologies (shown in Fig. 1-1) are produced: a granular solid (1-3 mm in diameter) with a grain size in the regime of 10's nm [2,3], and nanopowders (80-300 nm) that are assumed to be nucleated homogeneously or heterogeneously on other particles in the reactor [1,4,5]. Also, the granules have small pores, on the order of 5 μm, these pores don't appear in other conventional methods. The nanopowders are found on

the walls of reactor and are carried in the gas stream, and are assumed to form due to thermal decomposition of silane [6,7]. The CVD growth of silicon occurs at temperatures between 650 and 750 ºC for time ranging from several hours to several days depending on the desired final granule size. The polysilicon materials produced are feedstock polysilicon that are generally transported to other facilities for melting and manufacturing for commercial purposes such as ingots for solar cells. During handling and shipping tons of bags of polysilicon, the granules are in physical contact, where beads might fracture and produce fine silicon dust that creates some changes in the materials properties, the ability to process the solids, and safety issues.

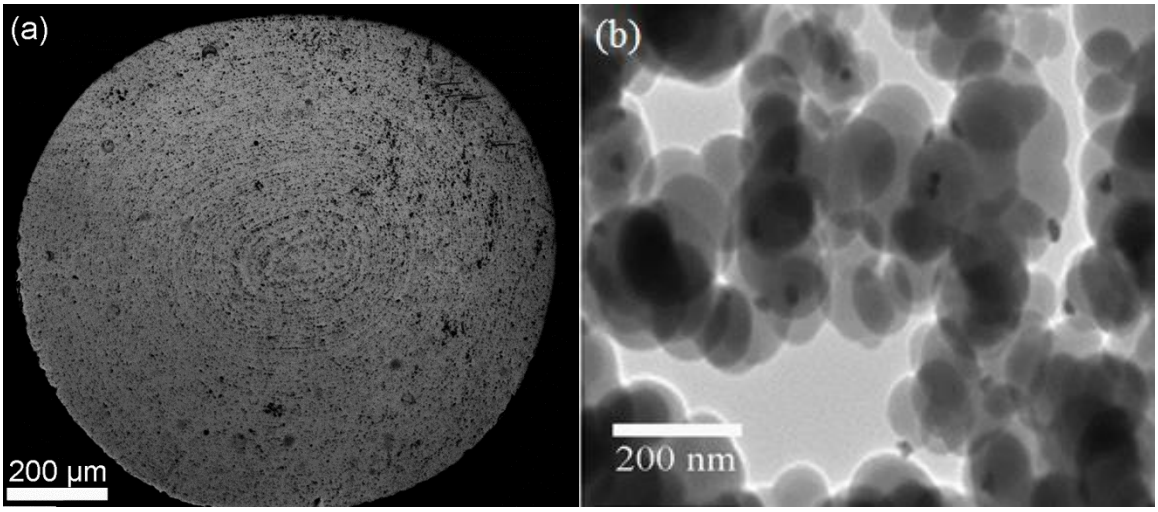

Figure 1-1 (a) Optical microscopy image showing cross-sectional view of granular FBR Si. [8]. (b) TEM image of the amorphous Si nanopwders [9].

Many groups have reported either toughness, strength, or fracture resistance measurements using double cantilever beam or indentation techniques, with results of fracture toughness, *T*, in the range of 0.6 – 0.95 MPa $m^{1/2}$ [11-15]. Cook suggests that using indentation, reasonable toughness value range between 0.73 and 0.89 MPa $m^{1/2}$ for (001) single crystals [16]. Most of the reported toughness values were done on single

crystal Si, where not many were tested for polycrystalline Si. Using double cantilever beam or compact tension requires machining that cannot be done on small granular materials. Using combination of nanoindentation and microindentation is more useful for measuring the toughness of small granular materials.

Processing temperatures tend to have some effects on the mechanical properties of bulk polysilicon. Previous work in our group has reported that for as grown material with a grain size of 3 μm, T was 0.81 MPa $m^{1/2}$, while for annealed materials, the toughness values altered between 0.57 to 1.11 MPa $m^{1/2}$ [16]; there was no clear trend in toughness with grain size in this material. Experimental measurements of toughness were also done for polysilicon by Chen and Leipold where they include precipitates and residual stress for large grains (2mm); their system had a fracture toughness of 0.75 MPa $m^{1/2}$ [13]. Polysilicon grown via the Siemens process showed values of toughness on the order of 1.5 – 1.8 MPa $m^{1/2}$ at room temperature, using disk-shaped compact tension samples [18]. The toughness values of polysilicon films for MEMS were reported to range between 0.9 and 1.9 MPa $m^{1/2}$ using micro-machined samples and indentation induced fracture [19-21]. The variety of reported toughness values for polysilicon is due to heat treatment conditions and deposition methods, where they lead to different grain sizes and residual stresses. Also, most of the measurements that were done using micro-machined structures cannot achieve a fine notch, and flaw distribution may dominate the results [17].

The FBRs are rich in hydrogen, which is used to control pyrolysis in the chamber, and large amounts of residual hydrogen have been shown to affect the mechanical properties of the final product [4,22,23]. Fourier transform infrared (FTIR) spectroscopy is a useful technique to identify hydrogen content in silicon is [24]. Recent work has

shown, through FTIR, that hydride stretching modes in silicon thin films affects solar cell performance [25,26]. FTIR spectra has shown different characteristic peaks that correlate to hydrogen in silicon, classified as a surface impurity, an interstitial impurity, and to oxidized Si. Si bond peaks range between 600 to 2400 cm^{-1}, while peaks at higher wavenumbers represent water contamination [27-31].

Literature example of hydrogen effects include that H can create vacancies in Si after growth, which can become voids [32]. Solute hydrogen can partially control the activation energy required to crystallize amorphous Si [33]. Also, B and P dopants can change the solute atoms in the structure [34]. Annealing Si in hydrogen rich environment can remove Si dangling bonds in the solid, and removing H-Si bonds can cause increase in toughness in amorphous Si [35,36].

Another issue that might occur to the produced silicon is the formation of agglomerates of Si nanopowders. Agglomeration could form due to the decrease in the solid mobility and at high silicon deposition rates [37]. Another study showed that when exceeding a critical value of initial concentration of silane (>20%), parasitic formation of nanopowders could occur, and powder particles agglomerate [1]. Other studies showed that the particle size of the bed material can have some effect on the agglomeration temperature [38]. This occurs in other FBR materials, like biomass fuel in a sand bed, where the combustor size, the sand size, and the internal reactor geometry affected the agglomeration mechanism [39]. Other agglomerates can be found for fabricated pharmaceuticals on the order of microns [40].

A study has used Transmission electron microscope (TEM) to examine the microstructure of polysilicon films produced by low-pressure CVD (LPCVD). The

results showed that films deposited between 550 and 590 ºC were partially amorphous and began to crystallize during the final stages of deposition. However, for deposition at initial temperature of 615 ºC, the films are crystalline with highly textures microstructure [41]. The reported sizes of nanopowders range between 5 to 100 nm for individual particles and aggregates up to 10 μm [23,42].

The Si nanopowders are secondary products, but they can be used for useful applications, as enrichment component to enhance the performance of electronic devices. Also, to improve the photocurrent in silicon solar cells, nanoparticles can be induced into coated composites. The light absorption of solar cells has been shown to improve by surface plasmon resonances in metal nanoparticles [43-47]. To tolerate the weak absorption areas in silicon, the shape, size, and dielectric environment can be controlled. Another example of enhancing photocurrent in crystalline silicon solar cells is by embedding gold nanoparticles (15 to 150 nm) into SiNx coatings [48]; for better light trapping, the distance between the Si photovoltaic layer and the nanoparticles can be controlled. The FBR Si nanoparticles can be embedded in carbon composites as carbon fibers or carbon nanotubes with electrodeposited Ni or Cu.

The main objectives of my dissertation are to:

- Study the morphology and microstructure of Si granules and powders
- See if there is any evidence of agglomeration in FBR granules by comparing the microstructure of the nanopowders and the granular materials
- Determine the mechanical properties of as grown and annealed polysilicon produced via FBR
- Study the effects of heat treatment processes on the fracture behavior

- Study the effects of solute hydrogen on the fracture behavior
- Propose new attrition and pulverization models for brittle microspheres
- Process Si nanoparticles into metal-coated carbon composites, using electroplating, to see if there any improvement in electrical resistivity

This dissertation consists primarily of work published over the past three years in the open literature; prior publication will be noted when appropriate at the start of each chapter.

Bibliography

1. Caussat B., Hemati M., Couderc J.P. Silicon deposition from silane or disilane in a fluidized bed-Part I: Experimental study. *Chemical Engineering Science.* 50, 3615-3264 (1995).
2. Dahl M.M., Bellou A., Bahr D.F., Norton M.G., and Osborne E.W. Microstructure and grain growth of polycrystalline silicon grown in fluidized bed reactors. *Journal Crystal Growth.* 311, 1496-1500 (2009).
3. Filtvedt W.O., Javidi M., Holt A., Melaaen M.C., Marstein E., Tathgar H., Ramachandran P.A. Development of fluidized bed reactors for silicon production. *Solar Energy Materials & Solar Cells.* 94, 1980-1995 (2010).
4. Qian Z.M., Michiel H., Van Ammel A., Nijs J., Mertens R. Homogeneous gas phase nucleation of silane in ow pressure chemical vapor deposition (LPCVD) *Journal of Electrochemical Society*. 135, 2378-2379 (1988).
5. Iya S.K., Flagella R.N., DiPaolo F.S. Heterogeneous decomposition of silane in a fixed bed reactor. *Journal of Electrochemical Society.* 129, 1531-1535 (1982).
6. Onischuk A.A., Strunin V.P., Ushakova M.A., Samoilova R.I., Panfilov V.N. Analysis of hydrogen and paramagnetic defects in a-Si : H aerosol particles resulting from thermal decomposition of silane. *Physica Status Solidi (b).* 193, 25-38 (1996).
7. Hsu G., Hogle R., Rohatgi N., Morrison A. Fines in Fluidized Bed Silane Pyrolysis. *Journal of Electrochemical Society*. 131, 660-663 (1984).
8. Zbib M.B., Sahaym U., Bahr D.F. Characterization of silicon nanoparticles formed from a fluidized bed reactor and their incorporation onto metal-coated carbon fibers. *Journal of the Minerals, Metal and Materials Society.* 66, 82-86 (2014).
9. Zbib M.B., Dahl M.M, Sahaym U., Norton M.G., Osborne E.W., Bahr D.F. Characterization of granular silicon, powders, and agglomerates from a fluidized bed reactor. *Journal of Materials Science.* 47, 2583–2590 (2012).

10. C. St. John. The brittle-to-ductile transition in pre-cleaved silicon single crystals. *Philosophical. Magazine.* 32, 1193–1212 (1975).

11. Brede M. & Haasen P. The brittle-to-ductile transition in doped silicon as a model substance. *Acta Materialia*. 36, 2003-2018 (1988).

12. Chen C.P., Leipold M.H. Fracture toughness of silicon. *American Ceramic Society. Bulletin*. 59, 469–472 (1980).

13. George A., Michot G. Dislocation loops at crack tips: nucleation and growth-an experimental study in silicon. *Materials Science and Engineering A*. 164, 118-134 (1993).

14. Ericson F., Johansson S., Schweitz J.A. Hardness and fracture toughness of semiconducting materials studied by indentation and erosion techniques. *Materials Science and Engineering A*. 105, 131-141 (1988).

15. Ebrahimi F., Kalwani L. Fracture anisotropy in silicon single crystal. *Materials Science and Engineering A*. 268, 116-126 (1999).

16. Cook, R.F. Strength and sharp contact fracture of silicon. *Journal of Materials Science*. 41, 841-872 (2006).

17. Fancher R.W., Watkins C.M., Norton M.G., Bahr D.F., Osborne E.W. Grain growth and mechanical properties in bulk polycrystalline silicon. *Journal of Materials Science*. 36, 5441-5446 (2001).

18. Brodie R.C., Bahr D.F. Fracture of polycrystalline silicon. *Materials Science and Engineering A*. 351, 166-173 (2003).

19. Sharpe W.N., Yuan B., Edwards R.L. Fracture tests of polysilicon film. *Materials Research Society Symposium Proceeding.* 505, 51–56, Boston, MA, USA, Dec1–5 (1997).

20. Tsuchiya T., Sakata J., Taga Y., Tensile strength and fracture toughness of surface micromachined polycrystalline silicon thin films prepared under various conditions. *Materials Research Society Symposium Proceeding*. 505, 285–290, Boston, MA, USA, Dec 1–5 (1997).

21. Kahn H., Tayebi N., Ballarini R., Mullen R.L., Heuer A.H. Fracture toughness of polysilicon MEMS devices. *Sens. Actuators A*. 82, 274-280 (2000).

22. Slootman F., Parent J.C. Homogeneous gas-phase nucleation in silane pyrolysis. *J. Aerosol Sci*. 25, 15-21 (1994).

23. Eversteijn F.C. Gas-phase decomposition of silane in a horizontal expitaxial reactor. *Philips Res. Repts.* 26, 134-144 (1971).

24. Langford A.A., Fleet M.L., Nelson B.P., Lanford W.A., & Maley N. Infrared absoption strength and hydrogen content of hydrogenated amorphous silicon. *Phys. Rev. B.* 45, 13367-13377 (1992).

25. Smets A.H.M, Matsui T, Kondo M. High-rate deposition of microcrystalline silicon p-i-n solar cells in the high pressure depletion regime. *J. Appl. Phys*. 104, 034508-1 - 034508-11 (2008).

26. Smets A.H.M, Matsui T, Kondo M. Infrared analysis of the bulk silicon-hydrogen bonds as an optimization tool for high-rate deposition of microcrystalline silicon solar cells. *Appl. Phys. Lett*. 92, 033506-1 – 033506-3 (2008).

27. Bronneberg A.C., Smets A.H.M, Creatore M., van de Sanden M.C.M. On the oxidation mechanism of microcrystalline silicon thin films studied by Fourier transform infrared spectroscopy *J. Non-Cryst. Solids.* 357, 884-887 (2011).

28. Kirk C.T. Quantitative analysis of the effect disorder-induced mode coupling on infrared absorption in silica. *Phys. Rev. B.* 38, 1255–1273 (1988).

29. Gupta P., Colvin V.L., George S.M. Hydrogen desorption kinetics from monohydride and dihydride species on silicon surface. *Phys. Rev. B.* 37, 8234-8243 (1988).

30. Stefanov B.B., Gurevich A.B., Weldon M.K., Raghavachari K., Chabal Y.J. Silicon Epoxide: Unexpected Intermediate during Silicon Oxide Formation. *Phy. Rev. Lett*. 81, 3908-3911 (1998).

31. Onischuk A.A., Levykin A.I., Strunin V.P., Ushakova M.A., Samoilova R.I., Sabelfeld K.K., Panfilov V.N. Aerosol formation under heterogeneous/ homogeneous thermal decomposition of silane: experiment and numerical modeling. *J. Aerosol Sci*. 31, 879-906 (2000).

32. Weber J., Fischer T., Hieckmann E., Hiller M., Lavrov E.V. Properties of hydrogen induced voids in silicon. *J. Phys.: Condens. Matter*. 17, S2303–S2314 (2005).

33. Odden J.O., Egeberg P.K., Kjekshus A. From monosilane to crystalline silicon. Part III. Characterization of amorphous, hydrogen-containing silicon products. *J. Non-Cryst. Solids*. 351, 1317–1327 (2005).

34. Saleh R., Nickel N.H., Maydell K.V. Influence of laser annealing on hydrogen bonding in compensated polycrystalline silicon thin films. *Thin Solid Films.* 487, 89–92 (2005).

35. Yamasaki S., Das U.K., Yasuda T. Fast hydrogen diffusion in hydrogenated amorphous silicon observed by in situ ESR. *J. Non-Cryst. Solids.* 299–302, 185–190 (2002).

36. Zajickova L., Bursikova V., Kucerova Z., Franclova J., Stahelb P., Perinac V., Mackova A. Organosilicon thin films deposited by plasma enhanced CVD: Thermal changes of chemical structure and mechanical properties. *J. Phys. & Chem. of Solids.* 68, 1255–1259 (2007).

37. Kato K., and Wen C.Y. Bubble assemblage model for fluidized bed catalytic reactors. *Chem Eng Sci* 24, 1351-1369 (1969).

38. Ohman M, & Nordin A.A New method for quantification of fluidized bed agglomeration tendencies: A sensitivity analysis. *Energy Fuels* 12, 90-94 (1998).

39. Chirone R., Miccio F., Scala F. Mechanism and prediction of bed agglomeration during fluidized bed combustion of a biomass fuel: Effect of the reactor scale. *Chem Eng J.* 123, 71-80 (2006).

40. Cheng H.J., Hsiau S.S. The study of granular agglomeration mechanism. *Powder Technol.* 199, 272-283 (2010).

41. Kahn H., He A.Q., Heuer A.H. Homogeneous nucleation during crystallization of amorphous silicon produced by low-pressure chemical vapour deposition. *Phil Mag A.* 82, 137-165 (2002).

42. Onischuk A.A., Strunin V.P., Ushakova M.A., Panfilov V.N. On the pathways of aerosol formation by thermal decomposition of silane. *J Aerosol Sci*. 28, 207-222 (1997).

43. Atwater H. A. & Polman A. Plasmonics for improved photovoltaic devices. *Nature Mater*. 9, 205-213 (2010).

44. Matheu P., Lim S.H., Derkacs D., McPheeters C., Yu E. T. Metal and dielectric nanoparticle scattering for improved optical absorption in photovoltaic devices. *Appl. Phys. Lett*. 93, 113108-1 – 113108-3 (2008).

45. Chen X., Jia B., Saha J. K., Cai B., Stokes N., Qiao Q., Wang Y., Shi Z., Gu M. Broadband enhancement in thin-film amorphous silicon solar cells enabled by nucleated silver nanoparticles. *Nano Lett*. 12, 2187-2192 (2012).

46. Spinelli P., Hebbink M., de Waele R., Black L., Lenzmann F., Polman A. Optical impedance matching using coupled plasmonic nanoparticle arrays. *Nano Lett*. 11, 1760-1765 (2011).

47. Pillai S., Catchpole K. R., Trupke T., Green M. A. Surface plasmon enhanced silicon solar cells. *J. Appl. Phys*. 101, 093105-1 – 093105-8 (2007).

48. Fahim N., Ouyang Z., Jia B., Zhang Y., Shi Z., Gu M. Enhanced photocurrent in crystalline silicon solar cells by hybrid plasmonic antireflection coatings. *Appl. Phys. Lett.* 101, 261102-1 – 261102-5 (2012).

CHAPTER 2. CHARACTERIZATION OF GRANULAR SILICON, POWDERS, AND AGGLOMERATES FROM A FLUIDIZED BED REACTOR

Previously published by Journal of Materials Science (JMS), *Volume 47, Issue 6, in March 2012.*

M. B. Zbib, M. M. Dahl, U. Sahaym, M. G. Norton, E. W. Osborne, D. F. Bahr

Abstract

Growth of polycrystalline silicon from fluidized bed reactors (FBR) produces two general types of silicon products: *granular material* (diameters on the order of mm) and homogeneously nucleated material often called *nanopowder* (diameters in the range 10-100 nm). Nanopowder particles tend to be amorphous and have a spherical morphology with an average particle diameter of ~80 nm. Granular material is generally spherical, highly twinned, polycrystalline with crystallite sizes that can reach 200 nm, and includes regions of porosity. The porosity is ~ 1-4 volume percent, and only the smallest pores exhibit evidence of amorphous regions along the pore surface. The amount of nanopowder that agglomerates on the granular material has been identified using transmission electron microscopy, but agglomeration plays only a minor role in the overall growth process. Therefore, it is proposed that the primary mechanism for granular formation in commercial FBR is chemical vapor deposition, and the pores are associated with nanopowder agglomeration and incomplete sintering.

2.1. Introduction

Fluidized bed reactors (FBR) are being utilized to manufacture polycrystalline silicon for the photovoltaic industry due to the energy and time saving capabilities of the process [1-3]. The growth uses a feedstock such as trichlorosilane ($SiHCl_3$) or silane (SiH_4) that decomposes via chemical vapor deposition (CVD) into solid silicon. In some commercial reactors this occurs in a hydrogen-rich environment at temperatures between 650 and 750 °C. Typical growth times range from hours to several days, depending on the size of the desired product. FBR silicon primarily forms two main morphologies: a granular solid [1,2] where the granule size is controlled by the fluidization parameters, and fine nanopowders [3] that are often assumed to be nucleated homogenously [4] or heterogeneously on other particles in the reactor [5] The resulting nanopowders can be found on the reactor walls, the silicon granular material, and loose within the chamber. The common assumption is that these particles are formed from the thermal decomposition of silane [6,7]. For the purposes of this paper the terms *granular material* and *nanopowders* will be used to distinguish these two product morphologies; though in the literature the terms fines and powder are sometimes used to describe the nanopowder product.

Synthesis in FBR is a flow process allowing for continuous withdrawal of product and supply of reactants. The beds in FBR are isothermal, that is, there are no local hot or cold spots that could cause damage to the product through thermal shock. In addition, the fluidized beds provide uniform mixing and hence produce consistent reaction products. However, the complex heat and mass transfer processes involved during the reaction in FBR are not completely understood. A number of research efforts have been directed

towards understanding this complex process. Kato and Wen [8] developed a model for growth of silicon in a gas phase fluidized bed that suggests a small bed height is efficient for CVD on existing material, i.e., distributing the flow of the silane over a large area, without exceeding the critical value of agglomeration, would improve yields. They showed that polysilanes were only minimally present at the top of the bed, while there was a sufficient amount at the exit to react heterogeneously to form fines on the walls where the temperature is not high enough; this observation contradicts the homogeneous nucleation models proposed for fines formation. Their experiment showed that agglomeration occurred because of a decrease in the solid mobility and at high silicon deposition rates. Another study [3] showed that when the initial concentration of silane exceeded a critical value, two problems could occur, parasitic formation of fine nanopowders and powder particle agglomeration. The main result of this study was that agglomeration occurred when the inlet concentration of silane gas was > 20%, and the ratio of the mass of fine nanopowder to total mass of product was ≤ 3%. It was proposed that the formation of fine nanopowder resulted from homogeneous nucleation of silane, which leads to the formation of silicon nuclei and subsequent growth of the powder.

Other studies of agglomeration as a primary growth mechanism include *in situ* measurements of pressure or temperature to infer changes in chemistry and material structure within the reactor [9]. The particle size of the bed material can have a small effect on the average agglomeration temperature [10]. This is not unique to silicon, it occurs in a wide range of FBRs, such as studies showing agglomeration of a biomass fuel in a sand bed, where the sand size, the combustor size, and the internal reactor geometry all influenced the agglomeration mechanism[11]. Using fluidized bed combustion, bed

agglomerates were detected on a biomass residue where a typical large agglomerate sample has a particle size of 100s μm [12]. Another study showed granular agglomeration of fabricated pharmaceuticals on the order of microns [13].

A recent study that observed the surface structure of microcrystalline silicon films showed that after columnar growth the conglomerate grains have a large lateral size [14]. The microstructure of polysilicon films produced by low-pressure CVD (LPCVD) has been studied using transmission electron microscopy (TEM) for deposition temperatures between 550 and 615 °C [15]. Films deposited between 550 and 590 °C were partially amorphous and began to crystallize during the final stages of deposition. Heterogeneous nucleation was observed where planar twin boundaries were present. If the deposition starts at a temperature of 615 °C, the films show crystalline phases that have a highly textured columnar microstructure.

Published results report a size distribution of nanopowders between 5 and 100nm for individual particles and up to 10μm for aggregates [7,16,17]. The growth of the particles is dependent on both homogeneous nucleation as well as heterogeneous deposition [7,17,18]. Previous studies have demonstrated that the heterogeneous contribution remains relatively low compared to the homogeneous decomposition portion for nanometer sized particles [16]. However, this does not necessarily identify the main growth mechanism for the granular material.

The objective of this experimental study is to determine if there is evidence of agglomeration in FBR granules by comparing and contrasting the microstructure of the nanopowder and granular material. Other objectives include determining the

crystallization temperatures of the nanopowders, and observations of the changes in particle size before and after crystallization.

2.2. Experimental Procedures

Polycrystalline granular Si beads and nanopowders were acquired from commercially available silane-based FBR material. The nanopowder material was collected using a filter system on the top of the growth chamber. The gaseous products leaving the reactor are run through a cyclone filter, which separates particles greater than approximately 1 μm in diameter from smaller nanopowders. The nanopowders are collected on a sub-μm filter, while the resulting clean gas is blended back into the reactant stream. More explanations about the FBR produced materials are discussed in [7,19]. The bead dimensions ranged from 1 to 5 mm in diameter, and were collected as they fell out of the FBR; these granular solids are the typical product of FBR and were statistically indistinguishable from a commercially available product. Both the granular material and nanopowders were collected while the reactor was producing a steady state product (i.e. several days into the process), and as such the material is felt to be representative of a commercial process. Approximately 500 g of granular material was examined from the middle of a run which produces multiple kilograms of material, and approximately 10 cm^3 of the nanopowders were removed from a filter by washing and then drying the resulting suspension. Both the nanopowders and the material from the cyclone filter are a minor component by weight of the total amount of silicon produced in these reactors.

The as-received granular and nanopowder materials were examined using scanning electron microscopy (SEM) and transmission electron microscopy (TEM) in order to

determine their microstructure. SEM analyses were conducted using an FEI Sirion field emission SEM operated at 20 kV. The Si beads were prepared using conventional techniques of grinding and polishing. Beads were mounted in epoxy and polished with a series of SiC and alumina grinding media, with final polishing using a colloidal silica media with a particle size 0.05 μm. The average diameter of the pores in the granular material was measured from three SEM images with a total of 295 counts of four different samples that were selected randomly from the sampled material, the similarity between the morphology of the random samples suggested that this was a representative sampling. The nanopowder samples were prepared by dry dispersing on double-stick carbon tape. Quantitative measurements of the microstructures were conducted using the commercially available image analysis software *Image J*.

TEM analyses were conducted using a Phillips CM-200 TEM operated at 200 kV for determining the overall structure of the material, and a JEOL 2100 HR operated at 200 kV for high-resolution imaging. For TEM preparation, beads with a nominal diameter of 3 mm were ground to a thickness of approximately 200 μm using a Gatan Model 623 Disc Grinder, with the section being primarily at the center of the bead. The samples were polished on both faces using water and lapping films of 30 μm, 15 μm, 6 μm, and 1 μm, successively to reach a sample thickness of 100 μm. The discs were dimpled using a VCR500i Dimpler to a thickness on the order of nanometers around a small hole that was formed in the center of the sample. The discs were thinned to electron transparency by etching in a solution of 93% nitric acid and 7% hydrofluoric acid.

To study the crystallization behavior, powder material was annealed at temperatures between 400 and 750°C. Prior to annealing, the powder samples were encapsulated in

evacuated quartz tubes. Zirconium ribbons were used as a getter for hydrogen and oxygen during annealing, and heating and cooling rates of 8 C/s were used to reach any given specific annealing temperature. The microstructure of the annealed powder samples was examined using TEM. Exact crystallization temperatures were determined using a differential scanning calorimeter (DSC) at a rate of 9.7 C/min.

2.3. Results and Discussion

Microstructural analysis revealed that the granular material is porous. The general position and arrangement of the pores is shown in a representative optical micrograph of a cross section of a granular bead in Figure 2-1(a). Pores in the granular material vary in size between 0.1 to 5 μm, as shown in the secondary electron micrograph in Figure 2-1(b). Since the pores are not spherical, we selected the largest lateral dimension observed in the random section to denote the maximum size of the pore. The pores generally form a series of concentric "onion-like" layers separated by rings consisting of higher concentration of pores with a complex pore morphology as shown in the SEM image in Figure 2-1(c). Detailed microstructural analysis of the pores in the granular material was conducted in a prior work by our group [20]. Quantitative examination of these layers showed that each layer has approximately the same radial separation from the previous layer and that all specimens examined share comparable ring and pore dimensions. The number of these concentric layers was also found to vary linearly with the granule diameter. It is assumed that a layer forms via some reproducible motion of the granular solid within the FBR [20]. This suggests that growth rate of the layers is dependent on the exposed surface area of the bead and not the volume of material deposited in any given layer. However, this does not definitively determine if pores are formed from the

agglomeration of homogenously nucleated nanopowders or are a product of chemical vapor deposition.

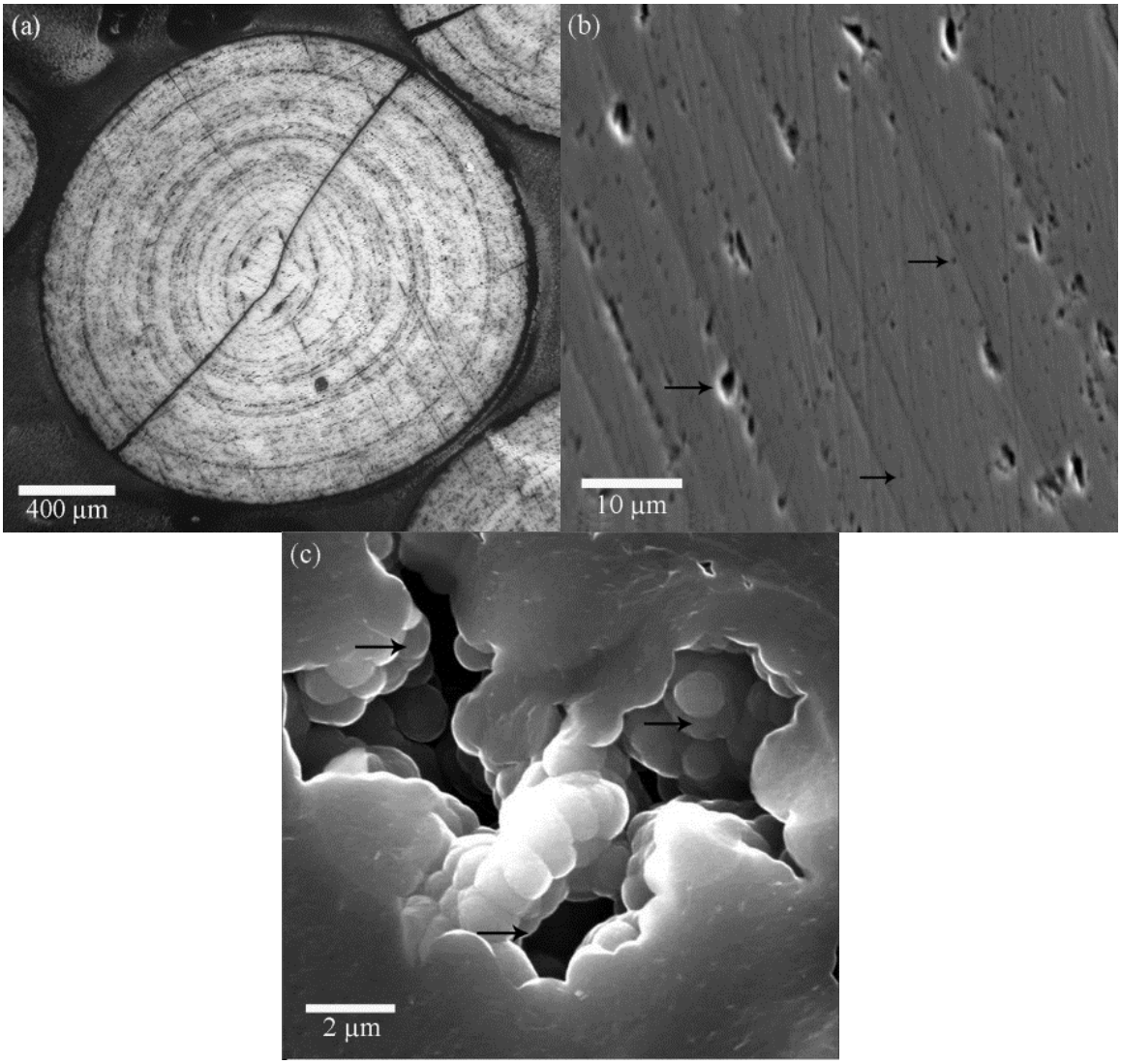

Figure 2-1. (a) Optical micrograph of cross section of a typical granular silicon bead showing onion like pore structure. (b) SEM micrograph that shows the layer-like arrangement of different sized pores. (c) SEM micrograph that shows the typical morphology of pores in 2 to 5 μm size range.

The volume fraction of porosity ranges between 1.5% and 4.0%, for a given granular bead. A given bead's porosity content did not have any direct relationship to the

diameter of the bead. The histogram in Figure 2-2 shows the frequency of the measured pores in a typical bead. The average percentages were divided into three main categories: pores < 0.5μm; pores between 0.5μm and 1.0μm; pores > 1.0μm. Each size range was represented by averages of 0.29%, 0.78%, and 1.42% of the total volume, respectively. The large pores occur less frequently than the small pores, but represent a greater percentage of the total pore volume in the bead.

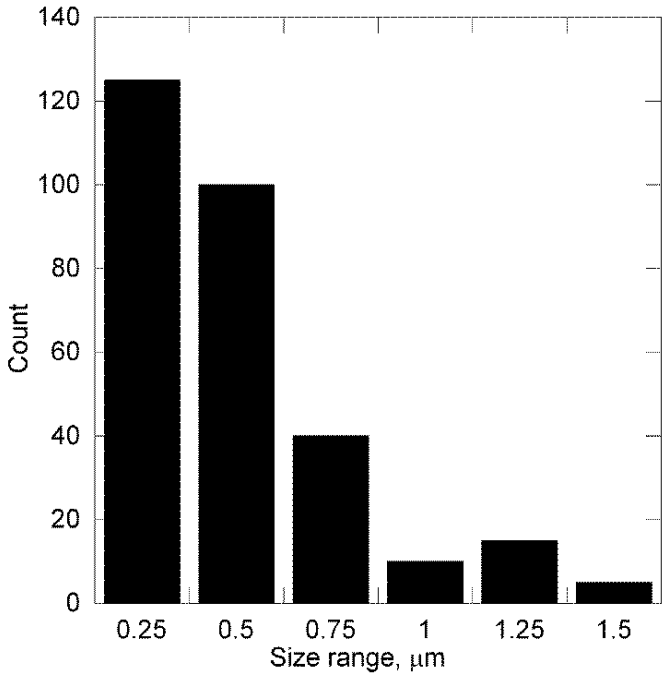

Figure 2-2. Pore size distribution in granular material.

TEM observations indicate that the granular material is mostly crystalline. Figures 2-3(a) and 2-3(b) show typical bright-field and dark-field TEM images, respectively. The crystallite size in the granular material was found to vary between 50 and 250 nm. Figure 2-3(c) shows a selected area diffraction pattern obtained from the area of the sample in Figure 2-3(a). This diffraction pattern, which can be indexed to Si, indicates that the material is polycrystalline. The dark field image was obtained using the (111) reflections

of Si, and clearly shows that some crystallites have dimensions exceeding 200 nm. Figure 4 shows that the granules consist of crystallites that have a high degree of defects, primarily twins. The overall grain size distribution collected from representative TEM images using the Heyn intercept method is shown in figure 2-5; this corresponds well with previous crystallite size measurements using x-ray diffraction [20] which showed a peak in grain size around 35 nm.

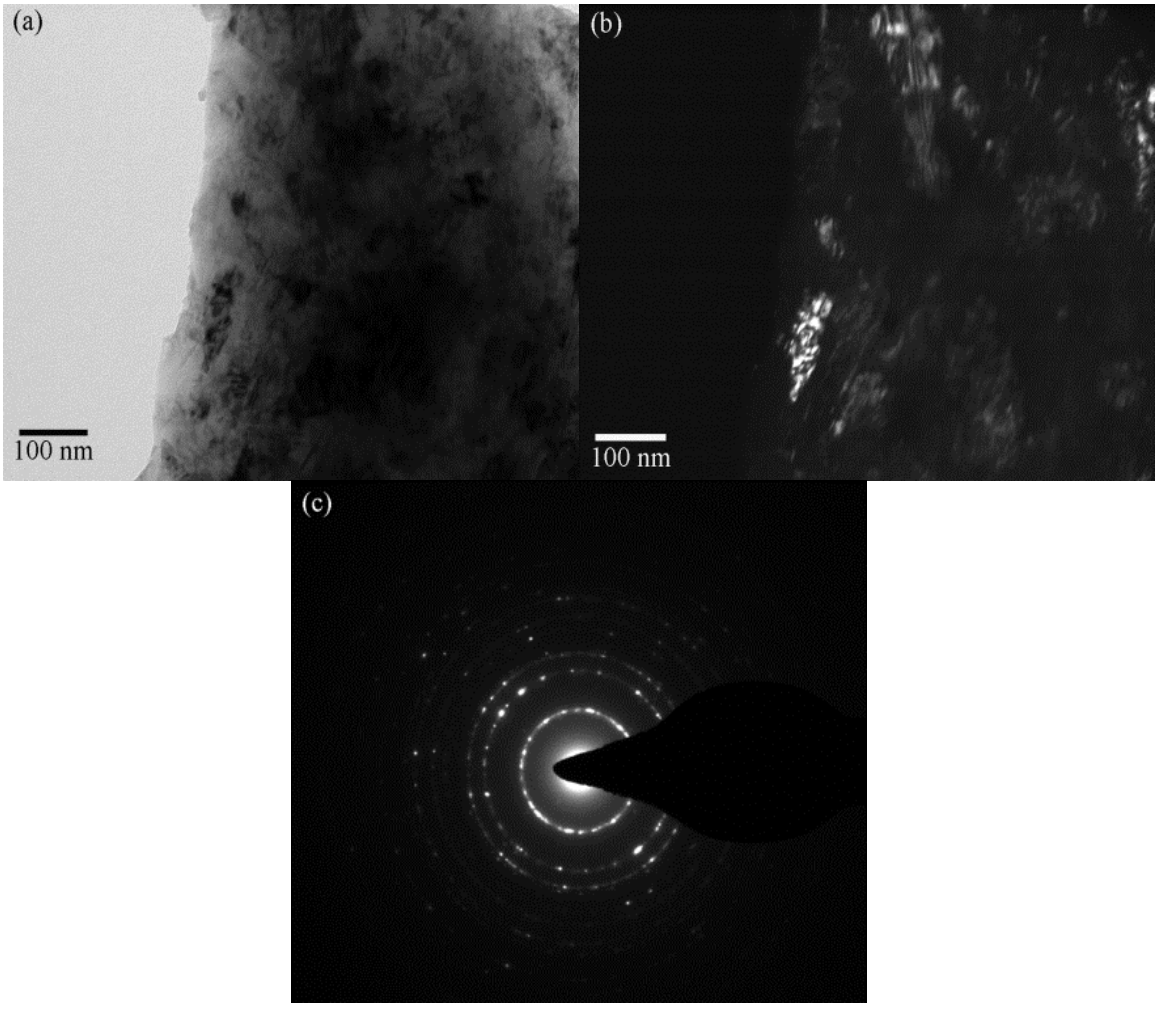

Figure 2-3. (a) TEM BF image and (b) TEM DF image that shows heavily twinned grains that vary in size between 50 to 250 nm. (c) Selected area diffraction pattern that indicates that the Si beads are primarily crystalline.

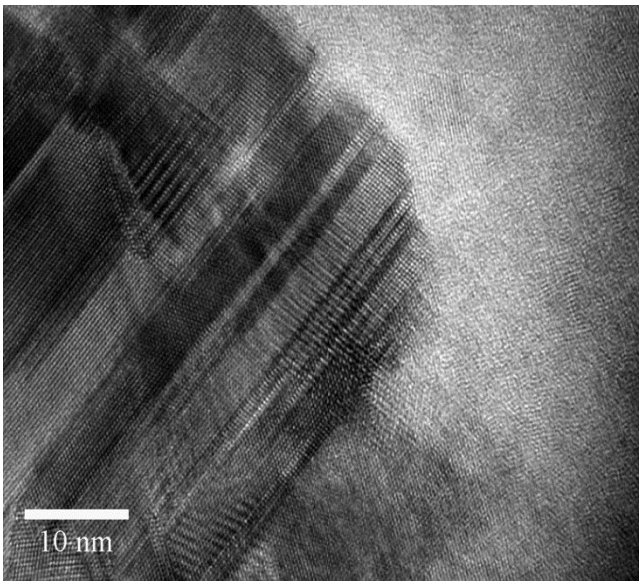

Figure 2-4. High-resolution TEM image of a primarily crystalline region within an individual granule. The crystallite is very heavily twinned.

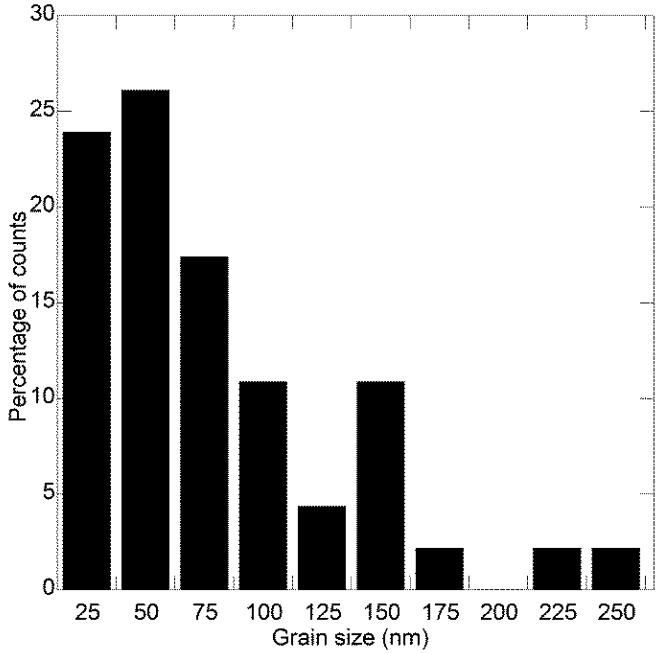

Figure 2-5. Grain size distribution in the granular material using the Heyn intercept method to analyze typical regions observed in the TEM.

It has been proposed in the literature that the fine nanopowders are a major contributor to the growth of granular silicon by means of particle "scavenging" [7]. In

this mechanism the fine powder particles would agglomerate on the granular material leading to growth, as opposed to the classical CVD model where the granular material grows layer-by-layer [21]. To determine if powder agglomeration is a significant growth mechanism in granular material, the morphology and crystallization behavior of nanopowder material was studied in detail. Typical structures of the nanopowder material collected from the FBR exhaust (shown in Figure 2-6) suggest that powder particles can indeed agglomerate. These particles were identified to be spherical in shape and amorphous in nature. A statistical analysis of the particle size distribution reveals that the mean and median diameters of the amorphous particles formed in this reactor are approximately 80 nm (±29nm) as seen in Figure 2-7.

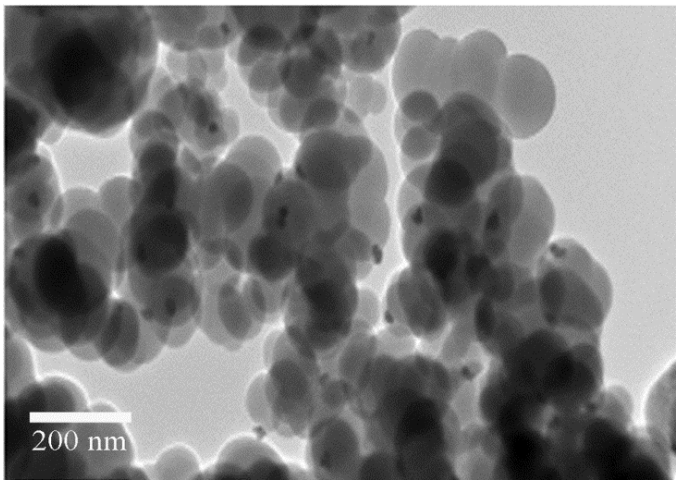

Figure 2-6. Amorphous nanopowders with an average diameter of 80 nm.

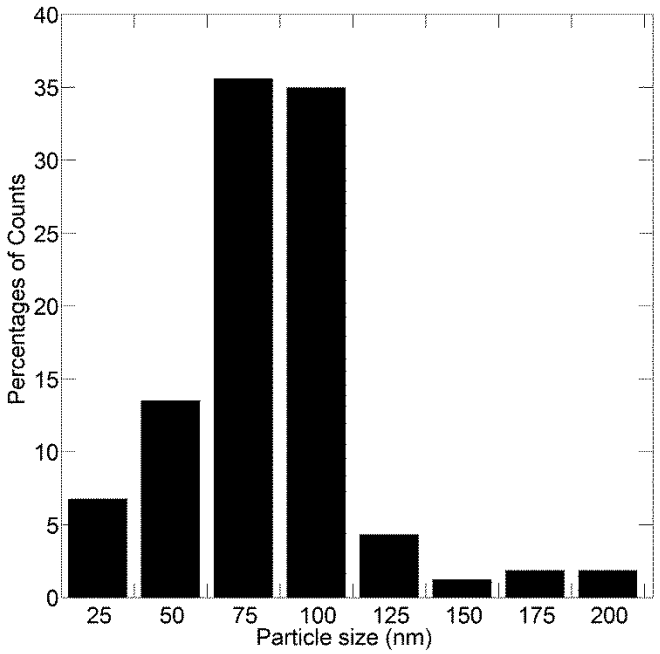

Figure 2-7. Particle size distribution of the nanopowder collected from a commercial FBR.

If the nanopowder particles were agglomerated into the granular material, they would likely be exposed to the growth temperature for a longer time than the as-collected nanopowder (i.e. we assume that the nanopowder in the filter did not spend as long in the FBR as any given granule). In an effort to determine how the structure of nanopowder particles from the FBR reactor is altered during exposure to higher temperatures, the powder was annealed at different temperatures. The representative TEM images of the resulting structure of nanopowder particles annealed for 6 hours at 600°C, 700°C and 750°C are shown in Figures 2-8(a), 2-8(b), and 2-8(c). The annealing used a ramp rate of 8 °C/s for both heating and cooling, the 6 hour time was the soak at maximum temperature. Figure 8 illustrates that as the annealing temperature is increased, a higher percentage of crystalline particles are observed. It was also noted that there was no

partial crystallization within a given spherical nanopowder particle. In addition to the increase in particle crystallinity, a small amount of necking becomes apparent at temperatures ≥700°C. However, statistical analysis confirmed that there is no additional growth in the diameter of the particles. There was no significant change in particle size and size distribution upon annealing. The observed size is in agreement with previously published literature [7,18]. It was also observed that during annealing of nanopowder at elevated temperatures for a given time, smaller powder particles remain amorphous whereas larger diameter particles crystallize first. Differential scanning calorimetry (DSC) analysis of the powder, shown in Figure 9, also revealed that crystallization occurs at ~ 660°C, which corresponds well to the TEM observations in Figure 2-8, where crystallization appears to be significant between 600 and 700°C. This temperature is slightly higher than that noted by Odden and co-workers [22], but it should be noted that the particles studied by this group were formed from pressurized silane, and the amorphous particles formed were about an order of magnitude larger than the particle size in the current study [23].

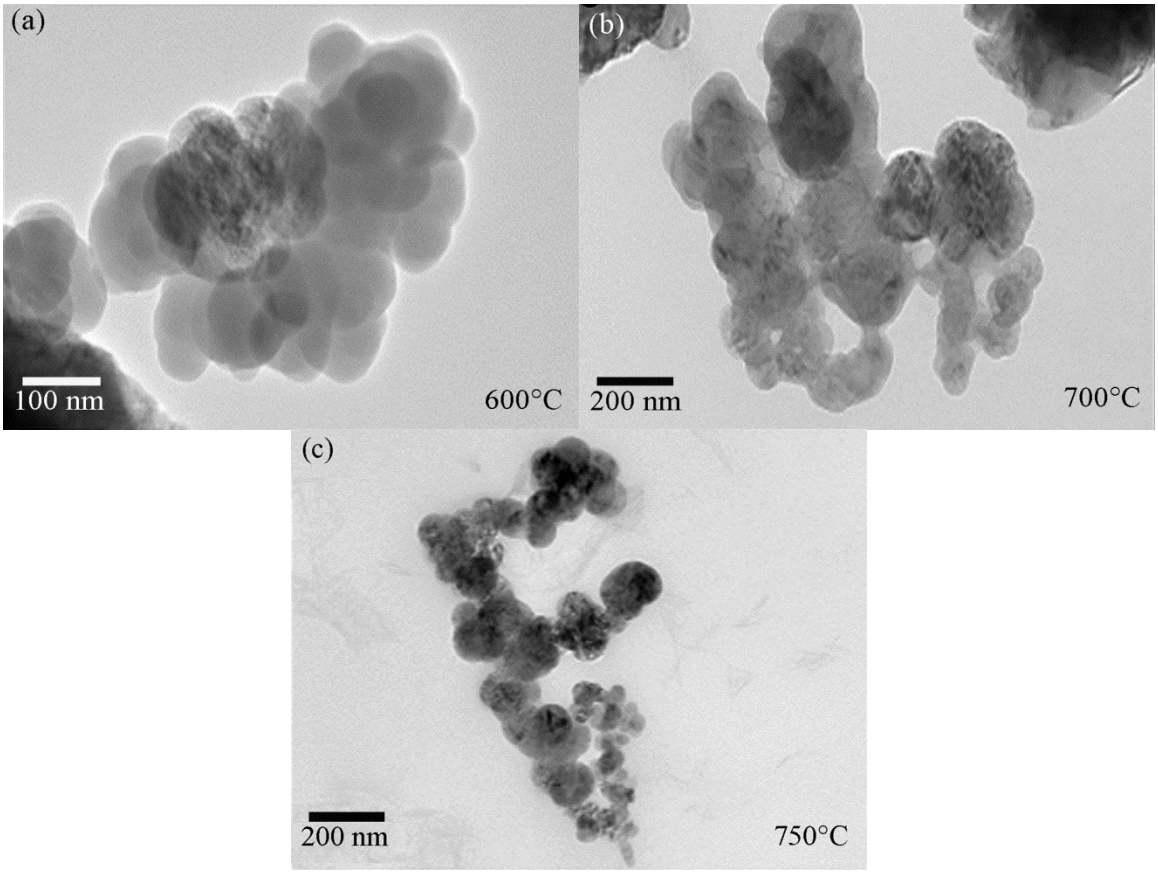

Figure 2-8. TEM micrographs of Aerosol particles formed in a FBR under the following conditions: (a) annealed at 600°C, (b) annealed at 700°C, and (c) annealed at 750°C.

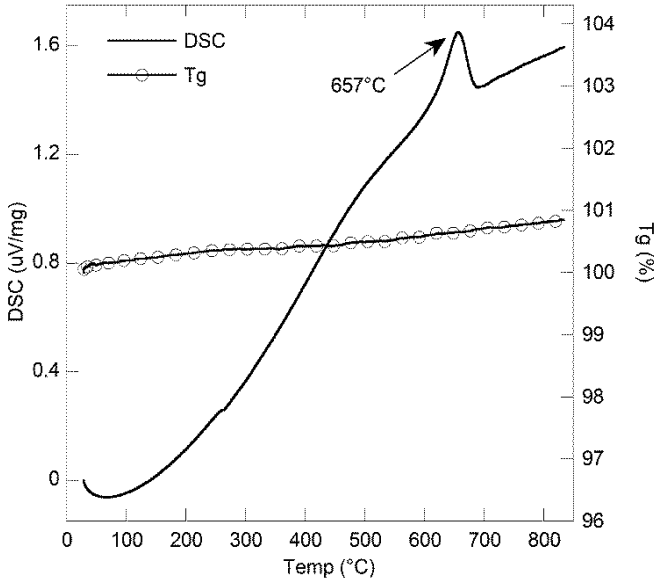

Figure 2-9. DSC results displaying crystallization at 657°C.

The granular material is primarily crystalline, while the fine nanopowders are primarily amorphous and they crystallize at temperatures > 660°C. In order to determine if there are any amorphous areas in the granular material, we examined the microstructure of granular solid in more detail. Samples for TEM imaging were prepared by collecting fractured portions of granular material on carbon coated TEM grids. While the granular bead is mostly crystalline (Figure 2-10a), there does appear to be some agglomerated amorphous particles within the granular solid. The amorphous particles are shown by black arrows in Figure 2-10b. These agglomerated amorphous particles were measured to be approximately 20 nm in size. It is noteworthy that the size of these particles conforms well with the dimensions of the smallest "bumps" that are present inside the pores (see Figure 2-1c)

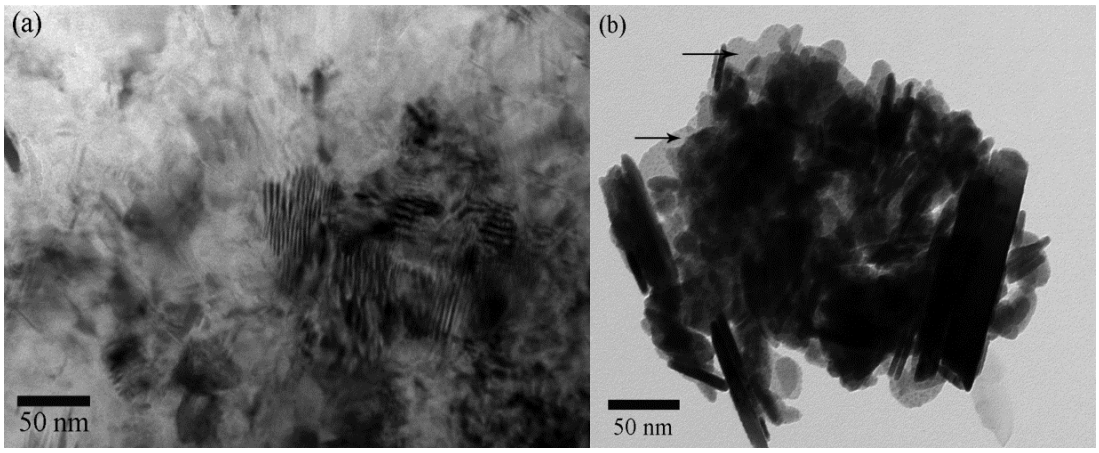

Figure 2-10. TEM images of grains in granular material: (a) Mostly crystalline material. (b) Crystalline material with some amorphous nanopowder that has agglomerated around the edges. The amorphous nanopowders are indicated by arrows.

Since some pores are present throughout the bulk material (as seen in Figures 2-1a and 2-1b), it was possible to analyze cross sections of the pores by TEM using thin foil TEM samples prepared from the granular material. Some amorphous regions appear

around the smallest pores as shown in Figure 2-11(a). The large pores that range between 0.5 μm and 3 μm have edges that are crystalline as illustrated in Figure 2-11(b). It must be noted here that since these images were taken from thin sections of the granular material, the pore dimensions do not correspond directly to those observed in the SEM. However, the pore dimension noted in the TEM would correspond to a lower bound estimate of pore size.

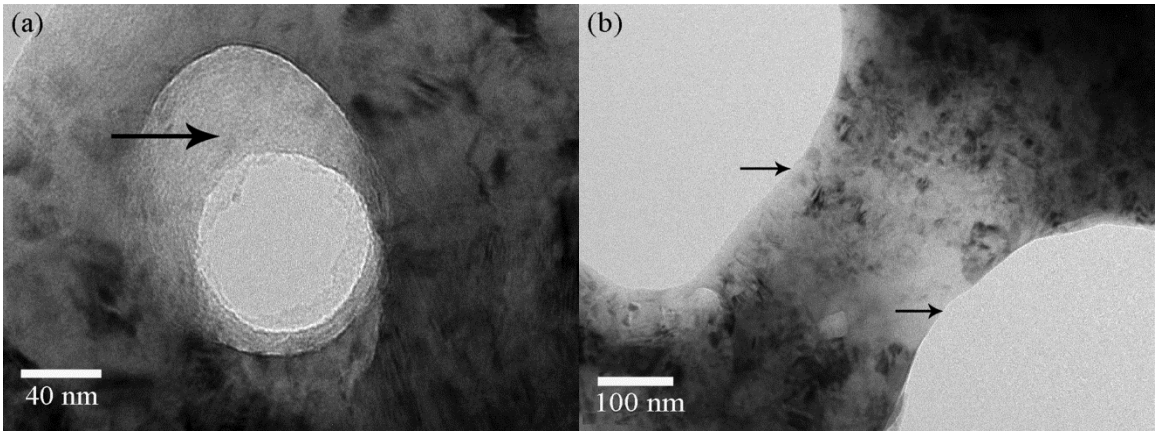

Figure 2-11. TEM images of pores in granular material: (a) Small pore with an amorphous periphery. (b) Large pores with crystalline edges.

As discussed in preceding paragraphs, the amorphous nanopowder particles crystallize at temperatures of about 650°C. Theoretically, there could be two scenarios associated with crystallization of agglomerated nanopowder particles. The first scenario is that heavily twinned grains form, and the crystallized and agglomerated nanopowder particles retain a grain size similar to the initial amorphous particle size. The second scenario is that the crystallized particles undergo substantial grain growth and maintain high density of twins. Since the results obtained in the present study show no significant change in the average particle size upon annealing the first scenario is most likely. The microstructural analysis of the granular material shows that it consists of heavily twinned

grains with sizes up to 250 nm. If the granular material in a commercial FBR grows primarily by agglomeration of nanopowder particles, it would require substantial grain growth after agglomeration and crystallization. Therefore, it is suggested here that although some agglomeration of nanopowder particles is evident in the vicinity of porosity in granular silicon formed in a FBR, it is not the major contributor to the growth of granular material in a FBR, since the pores account for only a maximum of 4 % of the total volume of the granules.

The other possible mechanism for the growth of the granular material would be CVD growth onto the granular solid. This process would require an initial seed material, such as a pre-seeded crystalline particle or a crystallized agglomerate of nanopowder particles. Further growth involves decomposition of Si-containing gas on the surface of the crystalline solid and partial crystallization of any agglomerated amorphous particles. We have shown that the final granular material that is formed is a bead that has concentric ring-like features in the cross section. Higher concentration of pores along the rings (shown in Figure 2-1a) is indicative of some agglomeration of nanopowder particles that slows or alters the subsequent deposition, possibly due to their amorphous nature. It is also possible that the ring of pores form when silane concentration in the fluidized bed is lower than some critical value resulting in more agglomeration and reduced CVD growth. A CVD growth hypothesis matches the observed and analyzed microstructures of the granular FBR material, suggesting that CVD growth is the primary mechanism of formation of the studied granular FBR silicon and that agglomeration plays a more minor role in the production of commercial FBR silicon.

2.4. Conclusions

Granular polycrystalline silicon grown with a commercial FBR is crystalline, with crystallite sizes reaching 250 nm and a high twin density. Spherical nanopowder particles formed in the FBR are mostly amorphous with an average diameter of 80 nm. Observations of the resulting microstructure suggest the primary mechanism for granular material formation in FBR is CVD growth, and that agglomeration may be related to the small pores found throughout the granular solid. This further suggests that while some agglomeration may exist it is not a major growth mechanism for the total mass of polycrystalline granular silicon produced in commercial FBR. The structure of the nanopowder particles formed in this study during post growth annealing suggests amorphous nanopowders will crystallize at around 650 °C, with no relatively change in particle size. Annealing nanopowders at these temperatures does not cause significant grain growth, and the dissimilarity of the grain size distribution in the granular solid from the particle size distribution in the nanopowder is suggested to be indicative that agglomeration is an unlikely mechanism for the majority of the growth of granular silicon.

Acknowledgements

We would like to acknowledge Mary Sandstrom of Los Alamos National Laboratory for carrying out the DSC experiments.

Bibliography

1. Zbib M.B., Tarun M.C., Norton M.G., Bahr D.F., Nair R., Randall N.X., Osborne E. Mechanical properties of polycrystalline silicon solar cell feed stock grown via fluidized bed reactor. *J. Mater. Sci.* 45, 1560-1566 (2010).
2. Filtvedt W.O., Javidi M., Holt A., Melaaen M.C., Marstein E., Tathgar H., Ramachandran P.A. Development of fluidized bed reactors for silicon production. *Solar Energy Materials & Solar Cells.* 94, 1980-1995 (2010).
3. Caussat B., Hemati M., Couderc J.P. Silicon deposition from silane or disilane in a fluidized bed-Part I: Experimental study. *Chemical Engineering Science.* 50, 3615-3264 (1995).
4. Qian Z.M., Michiel H., Van Ammel A., Nijs J., Mertens R. Homogeneous gas phase nucleation of silane in ow pressure chemical vapor deposition (LPCVD) *Journal of Electrochemical Society*. 135, 2378-2379 (1988).
5. Iya S.K., Flagella R.N., DiPaolo F.S. Heterogeneous decomposition of silane in a fixed bed reactor. *Journal of Electrochemical Society.* 129, 1531-1535 (1982).
6. Onischuk A.A., Strunin V.P., Ushakova M.A., Samoilova R.I., Panfilov V.N. Analysis of hydrogen and paramagnetic defects in a-Si : H aerosol particles resulting from thermal decomposition of silane. *Physica Status Solidi (b).* 193, 25-38 (1996).
7. Hsu G., Hogle R., Rohatgi N., Morrison A. Fines in Fluidized Bed Silane Pyrolysis. *Journal of Electrochemical Society*. 131, 660-663 (1984).
8. Kato K., and Wen C.Y. Bubble assemblage model for fluidized bed catalytic reactors. *Chem Eng Sci* 24, 1351-1369 (1969).
9. Nijenhuis J., Korbee R., Lensselink J., Kiel J.H.A, van Ommen J.R. A method of agglomeration detection and control in full-scale biomass fired fluidized beds. *Chem Eng Sci*. 62:644-654 (2007).

10. Ohman M, & Nordin A.A New method for quantification of fluidized bed agglomeration tendencies: A sensitivity analysis. *Energy Fuels* 12, 90-94 (1998).

11. Chirone R., Miccio F., Scala F. Mechanism and prediction of bed agglomeration during fluidized bed combustion of a biomass fuel: Effect of the reactor scale. *Chem Eng J.* 123, 71-80 (2006).

12. Scala F., and Chirone R. Characterization and Early detection of bed agglomeration during the fluidized bed combustion of olive husk. *Energy Fuels* 20, 120-132 (2006).

13. Cheng H.J., Hsiau S.S. The study of granular agglomeration mechanism. *Powder Technol.* 199, 272-283 (2010).

14. Toyama T, Sobajima Y, Okamoto H. Fractal study of surface nanostructures of microcrystalline silicon films: from growth kinetics to electronic transport. *Phil Mag*. 89,2491-2504 (2009)

15. Kahn H., He A.Q., Heuer A.H. Homogeneous nucleation during crystallization of amorphous silicon produced by low-pressure chemical vapour deposition. *Phil Mag A.* 82:137-165 (2002).

16. Onischuk A.A., Strunin V.P., Ushakova M.A., Panfilov V.N. On the pathways of aerosol formation by thermal decomposition of silane. *J Aerosol Sci*. 28, 207-222 (1997).

17. Slootman F., Parent J.C. Homogeneous gas-phase nucleation in silane pyrolysis. *J. Aerosol Sci*. 25, 15-21 (1994).

18. Onischuk A.A., Levykin A.I., Strunin V.P., Ushakova M.A., Samoilova R.I., Sabelfeld K.K., Panfilov V.N. Aerosol formation under heterogeneous/homogeneous thermal decomposition of silane: experiment and numerical modeling. *J. Aerosol Sci*. 31, 879-906 (2000).

19. Caussat B., Hemati M., Couderc J.P. Silicon deposition from silane or disilane in a fluidized bed – Part II: Theoretical analysis and modeling. *Chem Eng Sci*. 50, 3625-3635 (1995).

20. Dahl M.M., Bellou A., Bahr D.F., Norton M.G., and Osborne E.W. Microstructure and grain growth of polycrystalline silicon grown in fluidized bed reactors. *Journal Crystal Growth.* 311, 1496-1500 (2009).

21. Ohring M. Materials Science of Thin Films, Second Ed., *Academic Press*, San Diego, 277-279 (2002).

22. Odden J.O., Egeberg P.K., Kjekshus A. From monosilane to crystalline silicon. Part III. Characterization of amorphous, hydrogen-containing silicon products. *J. Non-Cryst. Solids*. 351, 1317–1327 (2005).

23. Odden J.O., Egeberg P.K., Kjekshus A. From monosilane to crystalline silicon. Part I: Decomposition of monosilane at 690-830 K and initial pressure 0.1-6.6 MPa in a free-space reactor. *Sol Energy Mater & Sol Cells*. 86:165–176 (2005).

CHAPTER 3. EFFECT OF SOLUTE HYDROGEN ON TOUGHNESS OF FEED STOCK POLYCRYSTALLINE SILICON FOR SOLAR CELL APPLICATIONS, PART 1

Previously published by Scripta Materialia, *Volume 67, Issue 9, in November 2012.*

M.B. Zbib, M.G. Norton and D.F. Bahr

Abstract

Three commercial polysilicon materials (1mm - 1 cm granular beads) produced from different fluidized bed reactors (FBR) were examined to determine the relationship between solute hydrogen and toughness. Infrared spectroscopy was used to identify hydrogen, and indentation was used to determine mechanical properties. Annealing the beads decreased solute hydrogen and increased toughness by 20%, from 0.74 to 0.97 MPa $m^{1/2}$. However, annealing also increased the crystallite size by as much as 50%, which can lower the toughness.

3.1. Introduction

Polycrystalline silicon (polysilicon) is used for production of silicon wafers, solar cells, and structures in micro-electro-mechanical systems (MEMS). One increasingly common method of producing polysilicon is the fabrication of granular products in fluidized bed reactors (FBRs) using trichlorosilane ($SiHCl_3$) or silane (SiH_4) via a chemical vapor deposition (CVD) process at temperatures between 650-750°C (SiH_4) or

950-1050°C ($SiHCl_3$). The reaction takes place over times ranging from several hours to days, and the primary product from these reactors is granular polysilicon with sizes on the order of mm's [1]. Silicon nanopowders with diameters from 10-100 nm are also produced through homogeneous and heterogeneous nucleation [2-4]. The reactors are rich in hydrogen, which is used to control pyrolysis and large amounts of residual hydrogen have been shown to affect the mechanical properties of the final product [3-5].

One useful technique to identify hydrogen content in silicon is infrared (IR) spectroscopy [6]. Some relatively recent work using Fourier transform IR (FTIR) spectroscopy has shown that hydride stretching modes in silicon thin films affects solar cell performance [7,8]. There are several characteristic peaks in FTIR spectra that have been linked to hydrogen in silicon, both as an interstitial impurity, a surface impurity, and related to oxidized Si. Peaks related to Si bonds range between 600 to 2400 cm^{-1} and peaks at higher wavenumbers are due to water contamination [9-13]. A summary of the FTIR peaks reported in the literature and their assignments are shown in Table 3-1.

Table 3-1. Summary of FTIR absorption frequencies for various Si bonds

Peak wave-number (cm^{-1})	Assignment
600-680	Si-H_x wagging [9]
1000-1200	Si-O-Si [10]
1900-2400	Hydrogen defects [11-13]

Literature examples of hydrogen effects in Si are prevalent. The implantation of H into Si after growth can create vacancies that eventually coalesce into voids [14]. Incorporation of H during growth is often used to form amorphous Si; the H forms Si-H bonds [15]. The activation energy required to crystallize amorphous Si is partially

controlled by solute hydrogen [16]. In addition, dopants such as B and P can alter the location of the solute atoms in the structure [17]. Annealing amorphous Si grown in a H-rich environment can remove Si dangling bonds within the solid [15,18] and the removal of hydrogen in complex H-Si structures causes toughness to increase in amorphous Si [19]. Most of these studies have examined H removal from small Si structures such as thin films and particles (with ~ 3 μm diameter) [20]. It may be more difficult to remove H from larger samples where diffusion path lengths to the free surface are longer.

With the advent of industrial scale FBR silicon production, large volumes of granular products must be handled during fabrication and transport, leading to the possibility of fracture of the bead-like granules. Determining the fracture response of the product is of interest in developing processing procedures to reduce the friability of the beads. Indentation-based fracture tests are commonly used to determine the fracture toughness of silicon. The fracture toughness of single crystal silicon lies between 0.73-0.89 MPa $m^{1/2}$ [21]. The toughness of single crystal silicon decreases with an increase in solute hydrogen concentration [22]; this has been ascribed to the formation of point defects within the lattice. Polysilicon films have fracture toughness that ranges between 0.9-1.9 MPa $m^{1/2}$ [23-26]. The toughness of polysilicon made by the Siemens process is approximately 0.8 MPa $m^{1/2}$, but annealing processes that alter the grain structure can lead to toughness values between 0.57-1.11 MPa $m^{1/2}$ [27]. For polysilicon grown using a FBR our group has measured the fracture toughness to be 0.6 MPa $m^{1/2}$ for the as-grown material and between 0.41-0.93 MPa $m^{1/2}$ for samples annealed between 600-1100°C [1].

Based on the range of defects that may be present when hydrogen dissolves in silicon, there is a need to determine the effects of these defects on the resulting mechanical

response of polysilicon. Of particular interest is the effect of hydrogen and hydrogen-related defects on the toughness. Previous work in our group has demonstrated that decreasing the amount of hydrogen, via annealing, can increase fracture toughness [1]. However, this earlier study did not identify the location of the hydrogen and did not look at a broad range of microstructures. Thus, the objective of this present work is to identify the location of hydrogen in a variety of commercially available FBR polysilicons and determine its effect on fracture toughness.

3.2. Experimental Procedures

The polycrystalline silicon materials used in this research are granular products from three different commercial manufacturers; these are products that could be purchased commercially in 2010. The three different granular products will be referred to as A, B, and C. These all represent feedstock materials grown via CVD at relatively high temperatures (more than 650°C). Polysilicon A is a silane-based material grown in a hydrogen-rich reactor. Polysilicon B is a quartz-based material with lower concentrations of hydrogen used in the production. Polysilicon C is a trichlorosilane-based material with almost no hydrogen used in the deposition procedure.

All experiments were performed on both as-grown and annealed materials. Granular solids were annealed in evacuated quartz tubes. Freshly cut zirconium ribbons were placed in the encapsulated tube to absorb any outgassing of oxygen and hydrogen from the samples. The annealed samples were held at the desired temperature for 6 h and then furnace cooled. Preparation of specimens for mechanical testing was done using conventional grinding and polishing. The cross-section microstructures of the three products are shown in figure 3-1. The dark regions refer to the pores present in the

materials. Polysilicon A shows a tree-ring like structure with higher pore density compared to polysilicons B and C. The difference in the microstructures is due to the growth conditions of each product.

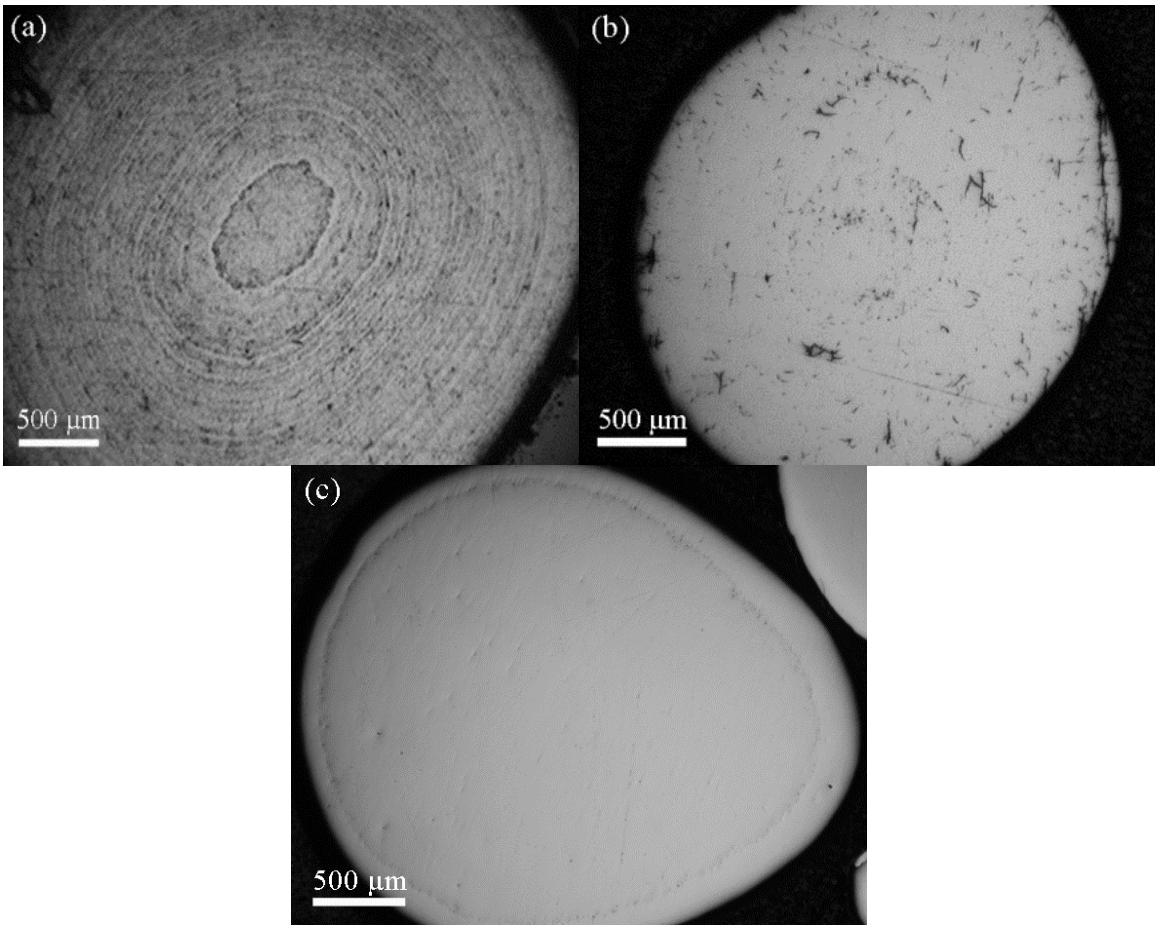

Figure 3-1. Optical micrographs showing polished cross-sections of the three polysilicon products, A (a), B (b) and C (c).

Hydrogen identification was performed using IR spectroscopy in the spectral range 400 – 5000 cm^{-1} with a Bomem DA8 spectrometer having a KBr beam splitter. The liquid nitrogen-cooled mercury cadmium telluride detector had a resolution of 4 cm^{-1}. The granular materials were ground using a mortar and pestle, mixed with potassium bromide (KBr) powder, and pressed into 0.3mm diameter pellets. The hydrogen content in the

polysilicon samples (wt.%) was measured using LECO experiment at NSL Analytical Services (Cleveland, Ohio).

The hardness and elastic modulus were measured using a Hysitron Tribondenter 900. The measurements were done at areas smaller than the pore spacing in the granular material to avoid any influence on the properties of the samples. The quasi-static test was done with maximum applied loads between 1800 and 9000 μN, where the hardness and modulus were calculated using the Oliver and Pharr method [28]. Fracture behavior was examined using a Vickers microhardness tester; loads between 0.49 and 4.9 N were applied and the resulting cracks measured using optical microscopy. The resulting relationship between applied load and crack size was used to determine the toughness of the material [29].

The crystallite sizes of the granular materials were measured using a Siemens D-500 X-ray powder diffractometer. The samples were ground to fine powder and attached to small glass plate with a few drops of ethanol. Diffractograms were obtained over the range $2\theta = 20° - 65°$, with a step of 0.02° and dwell of 1.0s. Data analysis was done using the program MDI Jade 8 and the crystallite sizes were determined using the method described by Williamson and Hall [30].

Transmission electron microscopy (TEM) was used to examine the microstructure of the polysilicon samples. A Philips CM-200 and a JEOL 2100 HR both operated at 200 kV were used. The granular materials were crushed to fine powders for testing. Sample preparation techniques are similar as described elsewhere [31].

3.3. Results and Discussion

FTIR was used to identify the existence of H in the material. A typical background subtracted FTIR spectrum, for sample grown in similar conditions to polysilicon A, is shown in figure 3-2 for wavenumbers between 500 and 5000 cm^{-1}. As identified earlier, Si-H_x wagging and bending exists at peaks between 600 and 900 cm^{-1}, and Si-O-Si bonds absorb between 1000 and 1200 cm^{-1}. Hydrogen defect bonds are identified by peaks between 1900 and 2400 cm^{-1}. At 1700-1730 cm^{-1} Si-Si bonds appear in the sample. Peaks higher than 2400 cm^{-1} are due to hydrolysis that occurs during sample preparation.

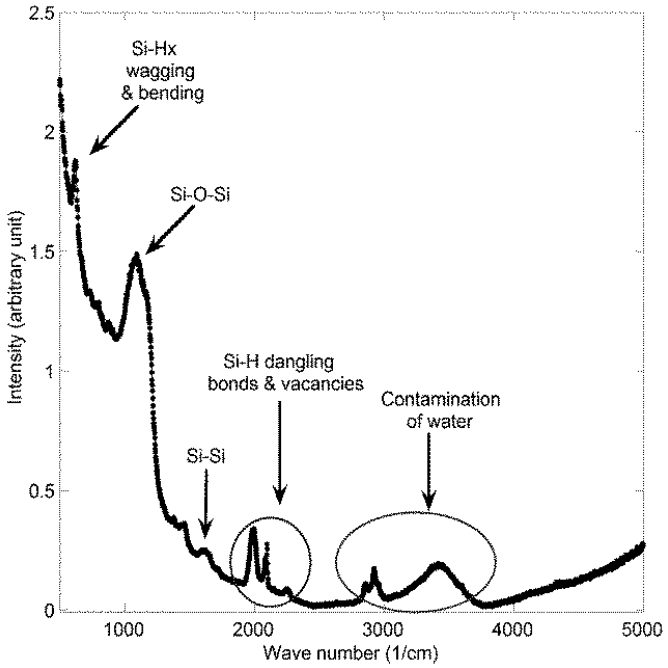

Figure 3-2. A normalized FTIR spectra of sample grown at similar conditions of polysilicon A that shows all types of bonds and defects with Si.

An FTIR spectrum identifying bonded hydrogen defects in the polysilicon samples is shown in figure 3-2. Peaks around 2030-2050 cm^{-1} represent Si-H dangling bonds and vacancies, peaks around 2110-2150 cm^{-1} are due to Si-H bonds on the surface of the

material. Isolated Si-H bonds also absorb at 2160 cm^{-1}, and Si-O-H bonds on the free surface give absorption peaks around 2300 cm^{-1}. Figure 3-3 shows no H in the as grown and annealed polysilicon C, while the other materials have H present in the as grown samples, but the H content decreases during annealing at 1000°C.

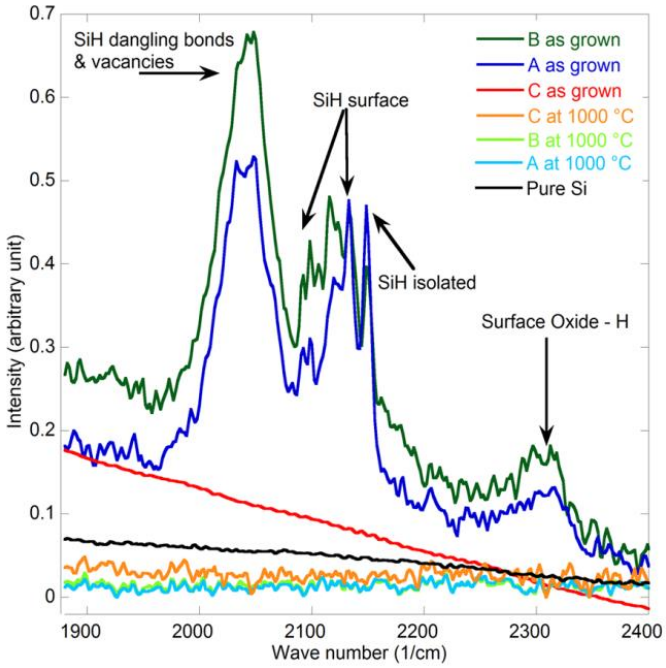

Figure 3-3. Normalized FTIR spectra between 1900-2400 cm^{-1} of as grown and annealed polysilicon materials A, B, and C.

LECO testing was done to determine the total amount of H present in each sample. The H content ranges between 0.010 % to 0.056%. The measurements show that after annealing, the percentage of H increases between 31% and 64% for polysilicon C and A, respectively. The increase in the amount of H corresponds to the IR analysis where the heights of the peaks at high wavenumbers, which are due to hydrolysis of the samples, increase after annealing. This increase is not indicative of solute H.

The hardness and elastic modulus values of the three FBR products did not show major changes before and after annealing. The hardness ranged between 9.7 and 11.3 GPa, and the elastic modulus was determined to be between 136 and 164 GPa. All the values of hardness and elastic modulus are shown in Table 3-2.

For indentations made at different loads, the resulting crack size can be related to the toughness by

$$T = \frac{\chi_r P}{c^{3/2}} \qquad \text{(Eq. 3-1)}$$

where P is the applied indentation load, c is the average crack size, and χ_r is a constant dependent on the specific indenter-material system, which is determined for each sample using

$$\chi_r = \xi\sqrt{\frac{E}{H}} \qquad \text{(Eq. 3-2)}$$

where E is the measured elastic modulus, H is the measured hardness of the material, and ξ is the indenter invariant constant, equal to 0.016 for experiments with a Vickers tip [29].

Figure 3-4 shows the size of the resulting cracks as a function of applied load for all the materials tested in this study; a minimum of 25 indentations were made for each material to determine the average crack size. The toughness was subsequently determined by curve fitting these data. The toughness values of all samples are listed in Table 3-2.

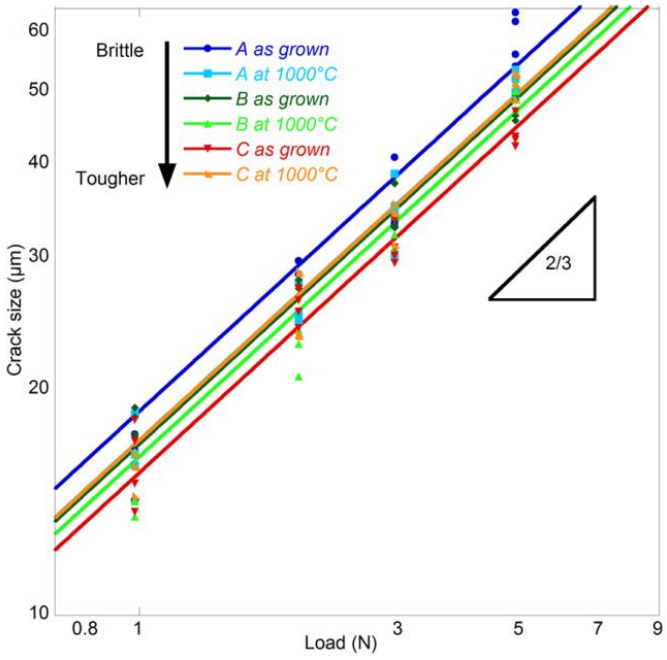

Figure 3-4. Average crack size vs. applied loads for polysilicon materials A, B, and C, as grown and annealed at 1000°C.

Table 3-2. Mechanical properties and crystallite sizes of all tested polysilicon materials measured using indentation techniques and XRD, respectively.

Polysilicon	Hardness (GPa)	Elastic Modulus (GPa)	Toughness ($MPa.m^{0.5}$)	Crystallite sizes (nm)
A: as grown	11.2±0.7	157±6	0.74±0.03	30.0±1.7
A: annealed	10.4±0.6	151±4	0.86±0.02	64.0±2.3
B: as grown	11.3±0.9	136±9	0.79±0.02	41.3±2.0
B: annealed	10.7±0.5	158±5	0.94±0.02	66.3±2.3
C: as grown	11.1±0.9	148±7	0.97±0.02	39.9±2.0
C: annealed	10.8±0.9	141±13	0.82±0.02	47.0±2.0

All samples of polysilicon that contained solute hydrogen in the as-grown state (A and B) showed an increase in toughness after annealing and a decrease in the FTIR peaks associated with solute hydrogen, while the toughness of material C decreases after annealing. Since polysilicon C has no measurable solute hydrogen before and after annealing, the resulting toughness change is most likely due to changes in the grain size.

XRD was used to determine the crystallite sizes of the polysilicon materials. These measurements are listed in table 3-2, where the crystallite sizes of materials A, B, and C increased after annealing by 53%, 38%, and 16%, respectively. From TEM analysis, it appears that commercially available granular polysilicon (irrespective of the precursor growth conditions) are 100% crystalline when grown, and therefore there is no concern that these materials undergo an amorphous to crystalline transformation during the annealing process.

3.4. Conclusions

In conclusion, solute hydrogen has a clear detrimental effect on the toughness of granular polysilicon grown with an FBR process. Additionally, the crystallite size of the structure is inversely related to the toughness. Removing solute hydrogen and increasing crystallite size exhibit competing effects on the toughness of FBR silicon. These results are important to the solar cell industry because of the need to handle and transport the polycrystalline product.

Acknowledgements

We thank Marianne Tarun at Washington State University for help with FITR measurements and Dr. Uttara Sahaym for help with initial instrument training. This work was supported by REC Silicon, Moses Lake, WA, 98837, United States, and we wish to thank E. Wayne Osborne and Matt Miller from REC with helpful discussions.

Bibliography

1. Zbib M.B., Tarun M.C., Norton M.G., Bahr D.F., Nair R., Randall N.X., Osborne E. Mechanical properties of polycrystalline silicon solar cell feed stock grown via fluidized bed reactor. *J. Mater. Sci.* 45, 1560-1566 (2010).
2. Hsu G., Hogle R., Rohatgi N., Morrison A. Fines in Fluidized Bed Silane Pyrolysis. *Journal of Electrochemical Society*. 131, 660-663 (1984).
3. Slootman F., Parent J.C. Homogeneous gas-phase nucleation in silane pyrolysis. *J. Aerosol Sci*. 25, 15-21 (1994).
4. Eversteijn F.C. Gas-phase decomposition of silane in a horizontal expitaxial reactor. *Philips Res. Repts.* 26, 134-144 (1971).
5. Qian Z.M., Michiel H., Van Ammel A., Nijs J., Mertens R. Homogeneous gas phase nucleation of silane in ow pressure chemical vapor deposition (LPCVD) *Journal of Electrochemical Society*. 135, 2378-2379 (1988).
6. Langford A.A., Fleet M.L., Nelson B.P., Lanford W.A., & Maley N. Infrared absoption strength and hydrogen content of hydrogenated amorphous silicon. *Phys. Rev. B.* 45, 13367-13377 (1992).
7. Smets A.H.M, Matsui T, Kondo M. High-rate deposition of microcrystalline silicon p-i-n solar cells in the high pressure depletion regime. *J. Appl. Phys*. 104, 034508-1 - 034508-11 (2008).
8. Smets A.H.M, Matsui T, Kondo M. Infrared analysis of the bulk silicon-hydrogen bonds as an optimization tool for high-rate deposition of microcrystalline silicon solar cells. *Appl. Phys. Lett*. 92, 033506-1 – 033506-3 (2008).
9. Bronneberg A.C., Smets A.H.M, Creatore M., van de Sanden M.C.M. On the oxidation mechanism of microcrystalline silicon thin films studied by Fourier transform infrared spectroscopy *J. Non-Cryst. Solids.* 357, 884-887 (2011).

10. Kirk C.T. Quantitative analysis of the effect disorder-induced mode coupling on infrared absorption in silica. *Phys. Rev. B.* 38, 1255–1273 (1988).

11. Gupta P., Colvin V.L., George S.M. Hydrogen desorption kinetics from monohydride and dihydride species on silicon surface. *Phys. Rev. B.* 37, 8234-8243 (1988).

12. Stefanov B.B., Gurevich A.B., Weldon M.K., Raghavachari K., Chabal Y.J. Silicon Epoxide: Unexpected Intermediate during Silicon Oxide Formation. *Phy. Rev. Lett*. 81, 3908-3911 (1998).

13. Onischuk A.A., Levykin A.I., Strunin V.P., Ushakova M.A., Samoilova R.I., Sabelfeld K.K., Panfilov V.N. Aerosol formation under heterogeneous/homogeneous thermal decomposition of silane: experiment and numerical modeling. *J. Aerosol Sci*. 31, 879-906 (2000).

14. Weber J., Fischer T., Hieckmann E., Hiller M., Lavrov E.V. Properties of hydrogen induced voids in silicon. *J. Phys.: Condens. Matter*. 17, S2303–S2314 (2005).

15. Camargo S.S. Jr., Carreno M.N.P., Pereyra I. Hydrogen effusion from highly-ordered new-stoichiometric *J. Non-Cryst. Solids*. 338, 70–75 (2004).

16. Odden J.O., Egeberg P.K., Kjekshus A. From monosilane to crystalline silicon. Part III. Characterization of amorphous, hydrogen-containing silicon products. *J. Non-Cryst. Solids*. 351, 1317–1327 (2005).

17. Saleh R., Nickel N.H., Maydell K.V. Influence of laser annealing on hydrogen bonding in compensated polycrystalline silicon thin films. *Thin Solid Films.* 487, 89–92 (2005).

18. Yamasaki S., Das U.K., Yasuda T. Fast hydrogen diffusion in hydrogenated amorphous silicon observed by in situ ESR. *J. Non-Cryst. Solids.* 299–302, 185–190 (2002).

19. Zajickova L., Bursikova V., Kucerova Z., Franclova J., Stahelb P., Perinac V., Mackova A. Organosilicon thin films deposited by plasma enhanced CVD: Thermal changes of chemical structure and mechanical properties. *J. Phys. & Chem. of Solids.* 68, 1255–1259 (2007).

20. Odden J.O., Egeberg P.K., Kjekshus A. From monosilane to crystalline silicon. Part I: Decomposition of monosilane at 690-830 K and initial pressure 0.1-6.6 MPa in a free-space reactor. *Sol Energy Mater & Sol Cells*. 86:165–176 (2005).

21. Cook, R.F. Strength and sharp contact fracture of silicon. *Journal of Materials Science*. 41, 841-872 (2006).

22. Zhao X.W., Su Y.J., Qiao L.J., Chu W.Y. Environment-assistant cracking of silicon single crystals. *Electrochem. & Solid-State Lett*. 9, B43-B46 (2006).

23. Ballarini R., Mullen R.L., Yin Y., Kahn H., Stemmer S., Heuer A.H.. The fracture toughness of polysilicon microdevices. *J. Mater. Res.* 12, 915-922 (1997).

24. Sharpe W.N., Yuan B., Edwards R.L. Fracture tests of polysilicon film. *Materials Research Society Symposium Proceeding.* 505, 51–56, Boston, MA, USA (1997).

25. Tsuchiya T., Sakata J., Taga Y., Tensile strength and fracture toughness of surface micromachined polycrystalline silicon thin films prepared under various conditions. *Materials Research Society Symposium Proceeding*. 505, 285–290, Boston, MA, USA (1997).

26. Kahn H., Tayebi N., Ballarini R., Mullen R.L., Heuer A.H. Fracture toughness of polysilicon MEMS devices. *Sens. Actuators A*. 82, 274-280 (2000).

27. Fancher R.W., Watkins C.M., Norton M.G., Bahr D.F., Osborne E.W. Grain growth and mechanical properties in bulk polycrystalline silicon. *Journal of Materials Science*. 36, 5441-5446 (2001).

28. Oliver W.C., Pharr G.M. An improved technique for determining hardness and elastic modulus using load and displacement sensing indentation experiments. *J. Mater. Res.* 7, 1564-1583 (1992).

29. Morris D.L., Cook R.F. Radial fracture during indentation by acute probes: I, description by an indentation wedging model. *Int. J. Fract.* 136, 237-264 (2005).

30. Williamson G.K., Hall W.H. X-ray line broadening from filed aluminum and wolfram. *Acta Metall.* 1, 22-31 (1953).

31. Zbib M.B., Dahl M.M, Sahaym U., Norton M.G., Osborne E.W., Bahr D.F. Characterization of granular silicon, powders, and agglomerates from a fluidized bed reactor. *Journal of Materials Science.* 47, 2583–2590 (2012).

CHAPTER 4. EFFECTS OF SOLUTE HYDROGEN ON THE TOUGHNESS OF POLYCRYSTALLINE SILICON, PART 2

Previously published by Proceedings of the 2012 International Hydrogen Conference, *WY, USA in 2014.*

M.B. Zbib and D.F. Bahr

Abstract

Polycrystalline silicon (polysilicon) produced using the fluidized bed reactor method was examined to study the effect of solute hydrogen on toughness in this material. Hydrogen was identified using infrared spectroscopy, and toughness was determined using indentation techniques. Polysilicon with almost no hydrogen in the production process has toughness of 0.97 MPa.$m^{1/2}$, while samples with increased hydrogen have toughness between 0.74-0.79 MPa.$m^{1/2}$. Annealing polysilicon to remove solute hydrogen increased the toughness at least 13%, but also leads to an increase in the grain size.

4.1. Polysilicon Background

Polycrystalline silicon (polysilicon) grown via fluidized bed reactor (FBR) is mainly used in subsequent growth of melt grown solar cells and production of single crystal silicon. The FBR method produces polysilicon as granules (mm's sizes) and nanopowders (10-100 nm diameters) [1] through the decomposition of trichlorosilane ($SiHCl_3$) or silane (SiH_4) via chemical vapor deposition (CVD) in a hydrogen rich environment, at temperatures between 650-750°C (SiH_4) or 950-1050°C ($SiHCl_3$).

Hydrogen is used to control pyrolysis, but an unintended consequence of using hydrogen is that incorporation of solute hydrogen can impact the subsequent mechanical properties of the polysilicon product.

Infrared (IR) Spectroscopy is a useful technique to identify hydrogen in silicon; Fourier transform IR spectra show peaks that identifies the bonds between hydrogen and silicon. Literature shows that peaks related to hydrogen defects in solution in silicon are found in the wavenumber range between 1900 to 2400 cm^{-1} [2-4]. Researchers showed that toughness of amorphous Si can increase due to elimination of hydrogen [5], and other work has shown that the performance of solar cell is affected by hydride stretching modes in silicon thin films [6,7]. While additional issues of hydrogen in this material may occur, such as hydrogen incorporation in a native oxide on the surface or as absorbed water on the surface, this work will focus only on the incorporation if hydrogen as solute in the silicon material.

4.2. Hydrogen and Mechanical Properties in Silicon

The purpose of this paper is to study the effects of solute hydrogen on the toughness of polysilicon by combining mechanical testing with the structure and concentration of hydrogen determined using Fourier transform infrared (FTIR) spectroscopy. Mechanical properties of polysilicon impact the overall viability of the process because bead fracture during handling is a problem for solar cell growth when shipped in tons of bags where unintended grinding occurs. The resulting friable product creates substantial dust that can adversely impact the material processing methods.

Previous work has detected that the toughness values of polysilicon produced by the Siemens process (with little if any solute hydrogen) is approximately 0.8 $MPa.m^{1/2}$, and

ranges between 0.57-1.11 MPa $m^{1/2}$ after annealing [8]. Our earlier studies showed that polysilicon grown via FBR process has toughness values of 0.6 MPa.$m^{1/2}$, and after annealing ranges between 0.41-0.93 MPa $m^{1/2}$ [1], but were not linked directly to hydrogen in a design of experiments.

In this current study indentation techniques were used to examine the mechanical properties of the produced polysilicon, and optical microscope and scanning electron microscope (SEM) were used to study its structure. Heat treatments were done to study the effect of thermal processing on the amount of hydrogen presented in the materials and their values of toughness.

4.3. Samples Tested

Three sets of samples were examined in this paper. The first set includes products from three different manufacturers; Polysilicon A is silane based (SiH_4), polysilicon B is quartz based (SiO_2), and polysilicon C is trichlorosilane based ($SiHCl_3$). This set was studied because each manufacturer has different amount of hydrogen present in the production processes with A exposing the samples to the most hydrogen during growth, B less hydrogen, and C has the least amount of hydrogen used in the growth process. The second set of polysilicon samples tested includes as grown and annealed samples grown from SiH_4 in order to study the effects of the amount of hydrogen in a given polysilicon microstructure. The third set includes three batches from same manufacturer produced with changes in hydrogen concentration and temperature at their production, growth conditions 1,2, and 3 were grown with decreasing H_2 respectively.

The as received samples were then annealed at temperatures between 800-1100°C. Prior to annealing, samples were encapsulated in evacuated quartz tubes, and zirconium

ribbons were used as a getter for hydrogen and oxygen during annealing. Samples were heated at a rate of 8°C/min and then were held at the peak temperature for 6 h, followed by furnace cooling back to room temperature.

4.4. Structure and Morphology of Polysilicon

Cross sections of the as-grown polysilicon beads form a ring structure visible using optical microscopy that consists of pores that range between 0.1 to 5 μm in diameter; the volume fraction of porosity ranges between 0.5 and 4 % in the granular materials. A byproduct of granular growth is the formation of powders with sub-micron dimensions. The granular polysilicon product is primarily crystalline while the nanopowders are mostly amorphous [9]. Fig. 4-1 shows the granular beads (4-1a), an optical image (4-1b) of the cross-section with the rings of voids present, and an SEM image (4-1c) demonstrating the different sizes of the pores that form the rings.

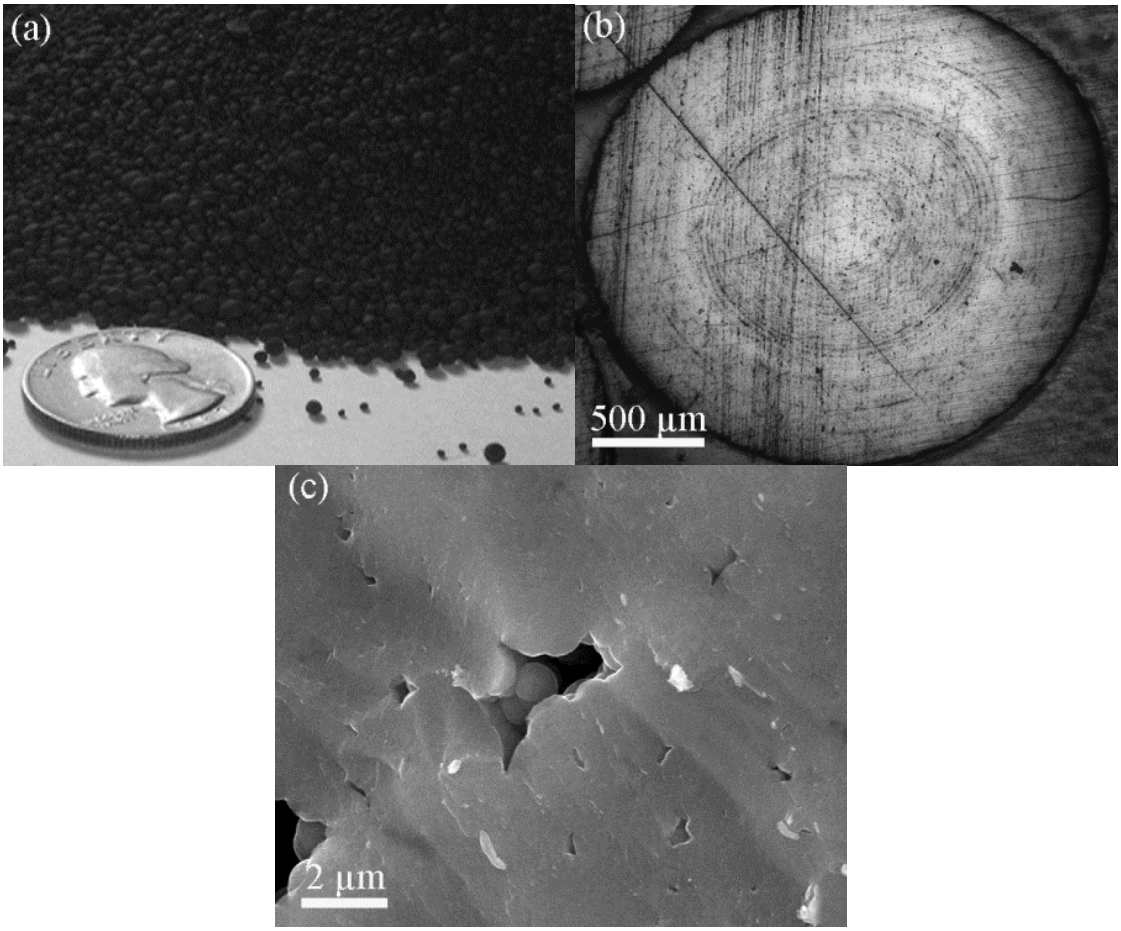

Figure 4-1. (a) Granular polysilicon; beads between 1 and 8 mm's in diameter, (b) optical micrograph of a cross-sectioned bead, and (c) SEM showing pores which made up the rings visible in (b).

4.5. Effects of Hydrogen on Toughness

Hydrogen was identified in silicon using FTIR spectroscopy. Hydrogen impurities within the Si structure manifest in the FTIR spectra between 1900-2400 cm^{-1}, while there are other FTIR peaks associated with H and silicon they can be ascribed to contamination of Si with H2O or Si-Si bonds. The fracture behavior was examined using a Vickers microhardness tester; granular material was mounted in epoxy and then ground and polished to expose cross sections of the material. Then, loads between 0.49 and 4.9 N

were applied with the microhardness tester and the diameter of the resulting cracks in the Si were measured. The hardness and modulus of grannular polysilicon were measured using a Hysitron Triboindenter 900. The toughness (*T*) was determined using

$$T = \frac{\chi_r P}{c^{3/2}} \qquad \text{(Eq. 4-1)}$$

where *P* is the applied load, *c* is the average crack size, and is a χ_r constant dependant on the specific indenter-material system, that can be determined using

$$\chi_r = \xi \sqrt{\frac{E}{H}} \qquad \text{(Eq. 4-2)}$$

where *E* is the measured elastic modulus, *H* is the measured hardness of the material, and ξ is the indenter invariant constant, equal to 0.016 for Vickers tip experiments [10]. We specify toughness at *T* rather than a specific mode of toughness because of the complexity of using indentation induced fracture and the inherent uncertainty related to the lack of a pre-crack [10].

The first set that includes 3 different manufacturers with different amount of hydrogen during production showed that all the samples have no hydrogen after annealed at 1000° C. Two products that have certain amount of hydrogen in the production showed an increase in toughness after being annealed (13 to 16 %), while the one with no hydrogen showed a decrease (15%). This decrease is related to the slight increase in the grain sizes, where the first two products showed a larger increase.

The batch that was tested to compare the as grown and annealed polysilicon showed that after annealing at 1100° C all hydrogen defects in silicon were gone, and the toughness was increased in about 13 %, with an increase in grain size. Polysilicon grown

with different amounts of hydrogen during production showed that toughness was increased as hydrogen was decreased. The increase went from first production to the second up to 23%, and to the third up to 43%, which indicated how solute hydrogen can affect the toughness polysilicon.

Figure 4-2 shows an FTIR spectrum between 1900-2400 cm^{-1} of as grown and annealed polysilicon, where all hydrogen defects were removed after annealing at 1000°C. Peak height tracks with concentration of H in the material, so we can nominally differentiate between low and high concentrations. After annealing, the toughness increased as shown in Fig. 4-3 where average crack size vs. applied load has been plotted. Figures 4-2 and 4-3 show a typical behavior of hydrogen defects and their effects on the toughness of polysilicon. All measurements of the mechanical properties for all tested samples are summarized in Table 4-1.

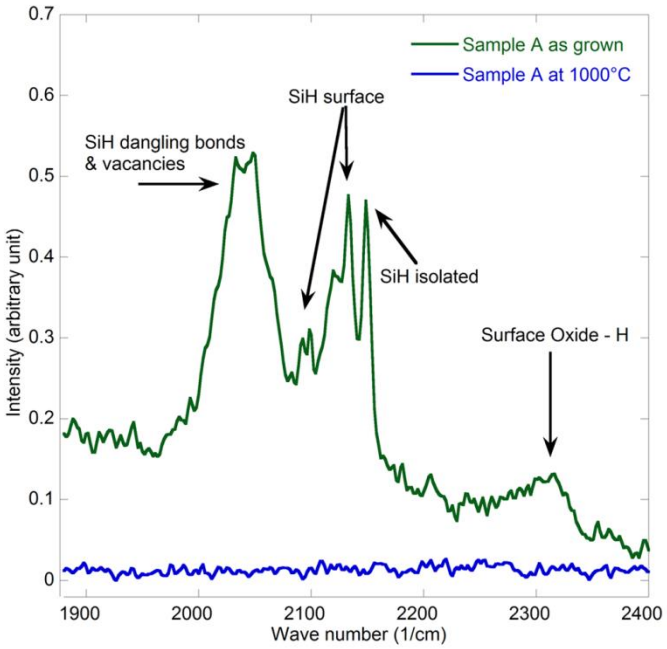

Figure 4-2. Normalized FTIR spectra of as grown and annealed polysilicon material A.

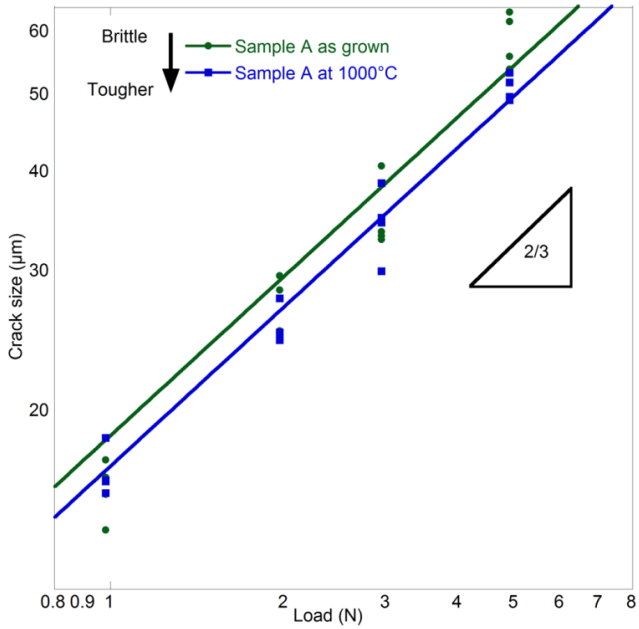

Figure 4-3. Average crack size vs. applied loads for polysilicon material A, as grown and annealed at 1000°C.

Table 4-1. Mechanical properties and crystallite sizes of all tested polysilicon materials measured using indentation techniques and XRD, respectively; some of these measurements were previously determined [1.11].

	Polysilicon	Hardness (GPa)	Modulus (GPa)	Toughness ($MPa.m^{0.5}$)	Crystallite sizes (nm)
1st set	*A:* as grown	11.2±0.7	157±6	0.74±0.03	30.0±1
	A: annealed	10.4±0.6	151±4	0.86±0.02	64.0±2
	B: as grown	11.3±0.9	136±9	0.79±0.02	41.3±2
	B: annealed	10.7±0.5	158±5	0.94±0.02	66.3±2
	C: as grown	11.1±0.9	148±7	0.97±0.02	39.9±2
	C: annealed	10.8±0.9	141±13	0.82±0.02	47.0±2
2nd set	As Grown	9.7 ± 0.4	164 ±3	0.60 ± 0.05	30±1.8
	800°C	9.1 ±0. 7	159 ± 7	0.60 ± 0.08	22±1.6
	900°C	9.5 ± 0.4	142 ± 3	0.41 ± 0.05	38±2.0
	1050°C	9.4 ±0. 6	166± 3	0.45 ± 0.06	60±2.1
	1100°C	9.9 ± 0.8	149 ± 3	0.69 ± 0.13	63±1.9
3rd set	Growth cond. 1	9.7 ± 0.4	164 ± 3	0.60 ± 0.05	30.0 ± 2.0
	Growth cond. 2	11.2 ± 0.7	157 ± 6	0.74 ± 0.03	30.0 ± 1.7
	Growth cond. 3	11.3 ± 0.8	145 ± 5	0.86 ± 0.03	31.3 ± 1.5

Crystallite sizes were determined using peak broadening during X-ray diffraction (XRD), and the values are listed in Table 4-1. It is shown that crystallite size increase after annealing with various ranges, where it can also affect the toughness values of polysilicon.

Another fracture test was done in order to check for an easier way to rapidly study bulk fracture behavior. Rockwell hardness tests were performed on granular material; the beads were placed in an aluminum tray with impressions in -which the beads were conformally supported, and then a Rockwell test was performed on individual granular products by applying loads between 15 and 75 Kg on the as-grown silicon beads with no prior preparations. Rockwell hardness tests showed that granular polysilicon with highest hydrogen failed at 45 Kg, samples with less hydrogen failed at 55 Kg, and samples with lowest hydrogen failed at 60 Kg. These results have the same trend as the small fracture scale using the Vickers indentation. Figure 4-4 shows that samples grown with lower hydrogen have small crack when tested at 45 Kg (Fig. 4-4a), while samples with higher hydrogen were broken into pieces at the same load (Fig. 4-4b).

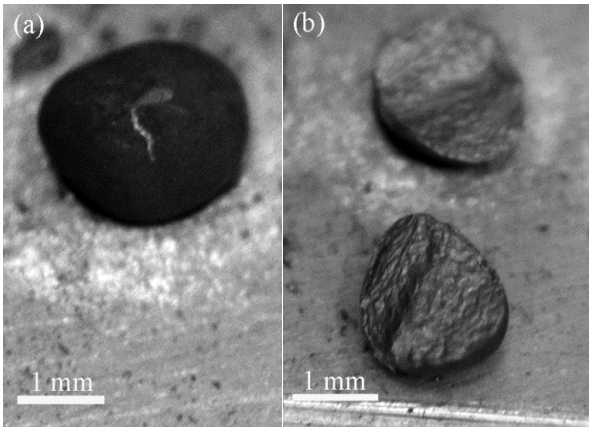

Figure 4-4. Optical images showing Rockwell hardness test applied using 45 Kg load; granular polysilicon with (a) lower hydrogen has small crack only, while (b) the one with higher hydrogen fractured into two pieces.

4.6. Conclusions

The toughness of granular polysilicon grown via FBR is affected by the amount of solute hydrogen present in the material. Using less hydrogen in the production process, and annealing at temperatures above 1000°C can increase the toughness of the final product between 13% to 43%. The presence of pores in the material has no effect on the crack morphology, while increased grain sizes appear to adversely affect the toughness. Removing solute hydrogen is the main key to increased toughness in FBR polysilicon. A simple indentation using a Rockwell hardness test qualitatively matched with the quantitative indentation measurements, showing that it can be used as a simple and quick technique to determine the relative fracture behavior of polysilicon under contact loading conditions.

Acknowledgments

We would like to thank REC Silicon, Moses Lake WA, for the financial support of this research, and in particular Matthew Miller for his helpful discussions of the FBR process.

Bibliography

1. Zbib M.B., Tarun M.C., Norton M.G., Bahr D.F., Nair R., Randall N.X., Osborne E. Mechanical properties of polycrystalline silicon solar cell feed stock grown via fluidized bed reactor. *J. Mater. Sci.* 45, 1560-1566 (2010).
2. Gupta P., Colvin V.L., George S.M. Hydrogen desorption kinetics from monohydride and dihydride species on silicon surface. *Phys. Rev. B.* 37, 8234-8243 (1988).
3. Stefanov B.B., Gurevich A.B., Weldon M.K., Raghavachari K., Chabal Y.J. Silicon Epoxide: Unexpected Intermediate during Silicon Oxide Formation. *Phy. Rev. Lett*. 81, 3908-3911 (1998).
4. Onischuk A.A., Levykin A.I., Strunin V.P., Ushakova M.A., Samoilova R.I., Sabelfeld K.K., Panfilov V.N. Aerosol formation under heterogeneous/homogeneous thermal decomposition of silane: experiment and numerical modeling. *J. Aerosol Sci*. 31, 879-906 (2000).
5. Zajickova L., Bursikova V., Kucerova Z., Franclova J., Stahelb P., Perinac V., Mackova A. Organosilicon thin films deposited by plasma enhanced CVD: Thermal changes of chemical structure and mechanical properties. *J. Phys. & Chem. of Solids.* 68, 1255–1259 (2007).
6. Smets A.H.M, Matsui T, Kondo M. High-rate deposition of microcrystalline silicon p-i-n solar cells in the high pressure depletion regime. *J. Appl. Phys*. 104, 034508-1 - 034508-11 (2008).
7. Smets A.H.M, Matsui T, Kondo M. Infrared analysis of the bulk silicon-hydrogen bonds as an optimization tool for high-rate deposition of microcrystalline silicon solar cells. *Appl. Phys. Lett*. 92, 033506-1 – 033506-3 (2008).
8. Fancher R.W., Watkins C.M., Norton M.G., Bahr D.F., Osborne E.W. Grain growth and mechanical properties in bulk polycrystalline silicon. *Journal of Materials Science*. 36, 5441-5446 (2001).

9. Zbib M.B., Dahl M.M, Sahaym U., Norton M.G., Osborne E.W., Bahr D.F. Characterization of granular silicon, powders, and agglomerates from a fluidized bed reactor. *Journal of Materials Science.* 47, 2583–2590 (2012).

10. Morris D.L., Cook R.F. Radial fracture during indentation by acute probes: I, description by an indentation wedging model. *Int. J. Fract.* 136, 237-264 (2005).

11. Zbib M.B., Norton. M.G., Bahr D.F. Effect of solute hydrogen on toughness of feedstock polycrystalline silicon for solar cell applications. Scripta Mater. 67, 756-759 (2012).

CHAPTER 5. FRACTURE BEHAVIOR OF GRANULAR POLYCRYSTALLINE SILICON USING MICRO-SCALE AND MACRO-SCALE INDENTATION TECHNIQUES

Previously published by Metallurgical and Materials Transactions E (MMTE), *Volume 1, Issue 1, in March 2014.*

M.B. Zbib and D. F. Bahr

Abstract

Three batches of polycrystalline silicon (polysilicon) produced with the fluidized bed reactor method were used to study the fracture behavior using micro-scale and macro-scale indentation techniques. The fracture toughness was determined to be 0.60, 0.74, and 0.86 MPa.m$^{0.5}$ using Vickers micro-hardness tests for three samples with high, medium and low hydrogen content respectively. In the same order of the samples, Rockwell hardness tests showed they failed at applied loads of 45, 55, and 60 kg respectively. These results show that the fracture behaviors of both techniques are in agreement; the highest toughness materials can withstand higher loads prior to fracture in the Rockwell hardness test. The microstructure of the granular product has been documented and the only significant difference between the samples is the solute hydrogen content. Therefore, a Rockwell hardness instrument can be used as a rapid way to assess the

relative fracture toughness of as-grown polysilicon for solar applications, and the technique is insensitive to small amounts of porosity in these materials.

5.1. Introduction

Polycrystalline silicon (polysilicon) produced using the fluidized bed reactor (FBR) method is mainly used in solar cell applications and the production of single crystal silicon. Granules (mm's size) and nanopowders (10-100 nm in diameter) [1] of polysilicon are produced from the FBR process using chemical vapor deposition (CVD)of silane (SiH_4) at temperatures between 923 to1023 K (650 to 750 °C), or trichlorosilane ($SiHCl_3$) at temperatures between 1223 to1323 K (950 to 1050 °C), in a hydrogen rich environment. The produced polisilicon has grain sizes in the 10's of nm regime [2].

Bead fracture during handling is a problem in processing this material for subsequent solar cell growth because dust can result from grinding while shipping the material in large quantities, which can be hazardous to subsequent users and handling. Most of the fracture behavior studies that have been done on polysilionuse nanoindentation, microindentation, or four point and cantilever beam techniques. Our previous work has determined the fracture toughness of as grown FBR polysilicon ranges between 0.6-0.97 $MPa.m^{0.5}$, usingVickers microhardness tests and nanoindentation tests [1,3]. These values will be compared to the new data presented in this paper using the same techniques, and compared to a new macro-scale technique for assessing fracture behavior. Other polysilicon produced from the Siemens process has toughness values of approximately 0.8 $MPa.m^{0.5}$ [4] for as-grown materials. Other research groups have determined the fracture toughness of polysilicon to range between 0.6-0.95 $MPa.m^{0.5}$ [5-11]. In general,

it is reasonable to assume that the toughness of as-grown polysilicon is on the order of 1 $MPa.m^{0.5}$.

Studying the mechanical properties using impact or compression tests for brittle materials has not been used as much as the indentation techniques. Different types of single particle tests (crushing tests and impact tests) have been done to investigate the breakage of other hard particle materials and to analyze the distribution of fracture energy under controlled loading conditions [12]. A study has been done to study the milling behavior of crystalline organic substances using single particle impact tests and compared them to the material properties from indentation techniques; those results showed that there is a relationship between indentation and bulk milling behavior, where the resistance of particulate material against fracture and the absorption energy are related to a brittleness index (ratio of hardness to fracture toughness) [13]. Another research group has developed a theoretical and experimental model of impact attrition of particulate solids for semi-brittle failure mode which provide an identification of impact mechanical properties; they defined a dimensionless attrition propensity parameter, η, that is related to impact conditions and material properties [14,15]. The parameter is

$$\eta = \frac{\rho v^2 l H}{K_c^2} \qquad \text{(Eq. 5-1)}$$

where *Kc* is the fracture toughness, *H* is the hardness, *l* is a characteristic particle size, *v* is the impact velocity, and ρ is the particle density.

Assessing the fracture behavior of polysilicon can be challenging according to the techniques used, and their associated sample preparation, handling, and testing. The purpose of this paper is to develop a new method to have a rapid assessment of fracture

behavior of polysilicon fabricated for the solar industry using a Rockwell hardness test to do a single particle test. This work will compare the fracture behavior of polysilicon using micro-scale technique (Vickers microhardness test) and macro-scale technique (Rockwell hardness test).

5.2. Experiment

Three batches of polysilicon were examined in this study; all of them were produced from the same manufacturer (REC Silicon Inc.), but with modest proprietary changes in hydrogen concentrations and temperatures during their production. We will refer to these batches as samples 1, 2, and 3 with decreasing H_2 during growth respectively. All these materials are silane-based feedstock materials grown via CVD at temperatures greater than 923K (650 °C). All experiments were done for as-grown granular polysilicon samples that are shown in Fig. 5-1.The samples were selected randomly from growth batches; all sample diameters ranged between 1 and 3 mm. The micromechanical properties (Vickers and nanoindentation) were measured on approximately 45 samples for each batch in order to study their fracture behavior and relate this to their morphologies.

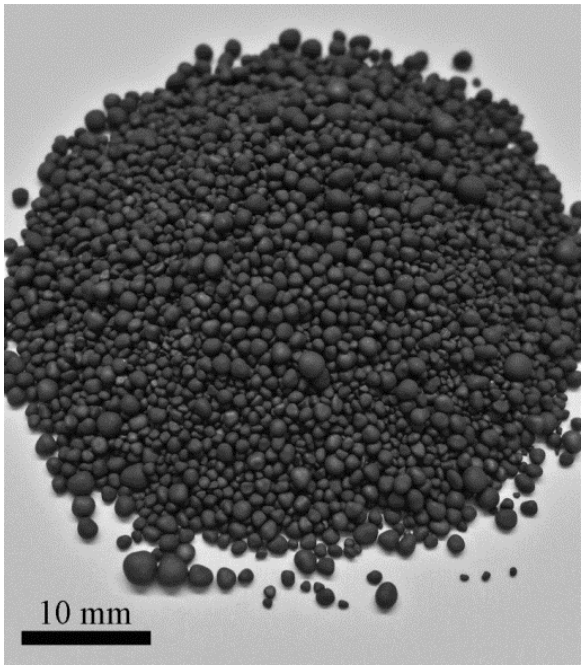

Figure 5-1. As grown FBR granular polysilicon (1-3 mm in diameter).

The fracture behavior was determined using a Vickers microhardness test, where loads between 0.49 and 4.9 N were applied, and the sizes of the cracks were measured using an optical microscope. The toughness of the material was then determined by the relationship between the applied load and the crack size [16].

The hardness and elastic modulus were measured using a Hysitron Triboindenter 900, where a quasi-static test was performed with maximum applied loads between 1800 and 9000 μN. In order to avoid any influence on the properties of the materials, all measurements were done at areas much smaller than the pore spacing in the granular material. Hardness and modulus were calculated using the Oliver and Pharr [17] method where they account for the curvature during unloading and the contact area at the peak load by determining the depth that is related to the indenter shape function. Preparation of specimens for measuring the mechanical properties was done using conventional grinding

and polishing methods. Representative granular samples were mounted in epoxy, and ground with 240 to 1200 grit silicon carbide abrasive paper. They were then polished using diamond paste from 3 to 0.25 μm. Note that these sample preparation methods are done only for Vickers and nanoindentation techniques, while macro-indentation tests were done with no prior sample preparation.

The impurities of hydrogen in silicon were identified using a Bomem DA8 Fourier transform infrared (FTIR) spectroscopy with a KBr (potassium bromide) beam splitter. The granular FBR Si was ground with a mortar and pestle and mixed with KBr powder, then pressed into pellets of 0.3 mm diameter. A liquid-nitrogen-cooled mercury cadmium telluride detector was used at a resolution of 4 cm^{-1} and spectral range of 400–5000 cm^{-1} wavenumbers.

A commercial Rockwell hardness tester (Wilson 3JR) was used to study bulk fracture behavior on the granular polysilicon of the three batches. An indent, with the size of the granular material, was made on an aluminum tray with circular impressions on the order of the granule size. The granular Si particles were then placed in these impressions prior to indentation. Rockwell tests were performed using a standard "B" steel spherical tip on individual granular polysilicon particles by applying loads between 15 and 75 kg with no prior sample preparation; the individual granule is tested as a whole sample, and not as a cross-sectioned sample. Approximately 35 samples were selected at random from each batch of the material; the nominal granule diameter was noted for each sample (all samples tested were close to spherical morphology, as are the vast majority of the product as noted in Fig. 5-1).

A Siemens D-500 X-ray powder diffractometer was used to measure the crystallite sizes of the granular material. Granules of polysilicon were ground to a fine powder and samples were prepared on small glass plate with few drops of ethanol. Diffractograms were obtained within the range of 2θ = 20° - 65°, with a step of 0.02° and dwell of 1.0s. The program MDI Jade 8 was used to perform the data analysis, and the crystallite sizes were determined using the method described by the Williamson and Hall [18] equation:

$$B\cos\theta = \frac{k\lambda}{D} + \alpha\sin\theta \qquad \text{(Eq. 5-2)}$$

where B is the peak width difference, k is a constant (~1), λ is the X-ray wavelength, D is the average grain size, and α is the strain. Optical microscopy and a scanning electron microscope (SEM) operated at 20 kV were used to study the microstructure of the samples.

5.3. Results

The hardness and elastic modulus of the three different batches of polysilicon did not show very significant changes; they ranged between 9.7-11.3 GPa and 145-164 GPa respectively. These hardness and modulus values are considered reasonable for sample-to-sample comparison within this study. The elastic modulus was calculated using the Oliver and Pharr method [17]:

$$\frac{1}{E_R} = \frac{1-v_i^2}{E_i} + \frac{1-v_s^2}{E_s} \qquad \text{(Eq. 5-3)}$$

where E_R is the reduced modulus of the unloading slope, E_s is the elastic modulus of the sample, E_i is the modulus of the diamond indenter tip that is equal to 1249 GPa, v_s and v_i are the Poisson's ratio of the sample (0.27) and the diamond indenter tip (0.07)

respectively. E_r is related to the stiffness (S) and the known projected area function (A) of the elastic contact by

$$S = \frac{2}{\sqrt{\pi}} E_r \sqrt{A} \qquad \text{(Eq. 5-4)}$$

while the hardness (H) is related to the peak indentation load (P_{mzx}) and was calculated using

$$H = \frac{P_{max}}{A} \qquad \text{(Eq. 5-5)}$$

The fracture toughness (T) was determined by

$$T = \frac{\chi_r P}{c^{3/2}} \qquad \text{(Eq. 5-6)}$$

where P is the applied load using a Vickers microhardness tester, c is the average crack length (Fig. 2a), and χ_r is a constant dependent on the specific indenter-material system:

$$\chi_r = \xi \sqrt{\frac{E}{H}} \qquad \text{(Eq. 5-7)}$$

where H is the measured hardness, E is the measured elastic modulus, and ξ is the indenter invariant constant which is equal to 0.016 for Vickers tip experiments [16]. In our measurements we use toughness T rather than using mode I fracture toughness K_{IC} because of the absence of pre-cracks and the indistinct use of indentation induced fracture. Fig. 5-2b shows the average crack vs. applied load where equation 5-6 was curve-fitted for each sample to determine T. The toughness behaviors that are shown in Fig. 5-2b are fitted to 2/3 power relationship according to Eq. 5-6. Deviations at low loads are likely due to some inhomogeneity of the product and the difficulty in assessing the crack distances at the shallowest loads used in the study. Table 5-1 uses the best fit assuming a

2/3 power. As noted in Fig. 5-2b there can be significant variation among the samples. Note that in Fig. 5-2a the cracks do not show any deviation effects from the pores; the variation in properties may be due to variations in grain size or sub-surface texture.

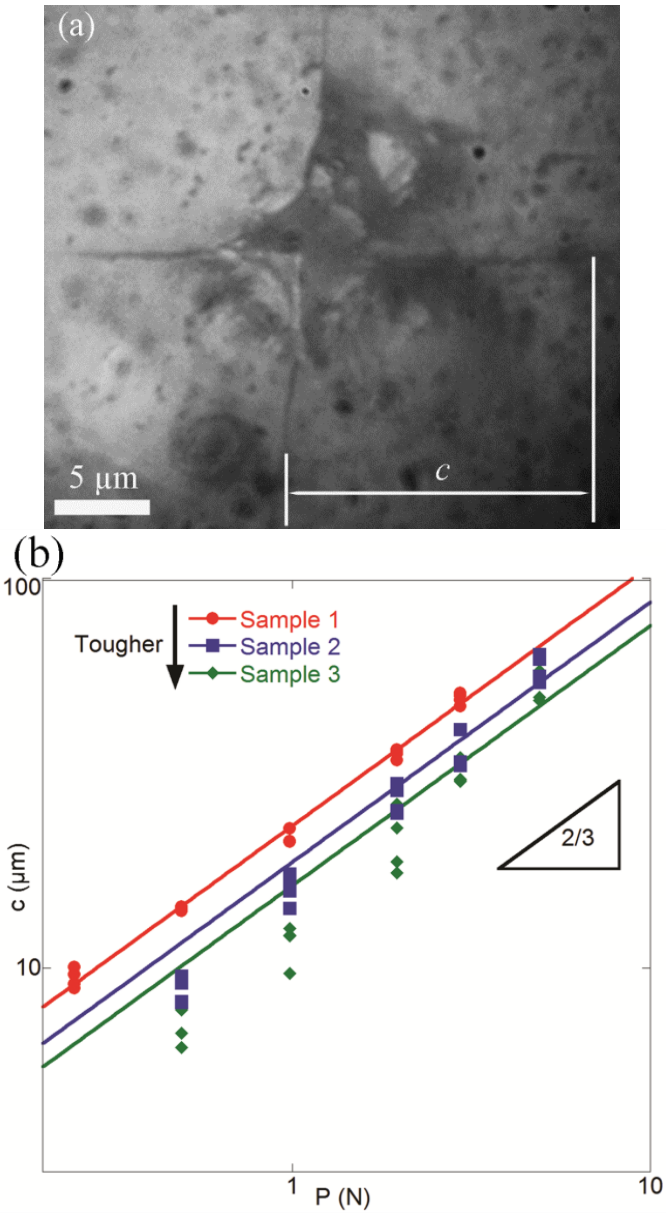

Figure 5-2. (a) Cracks formed around Vickers indentation and (b) average crack size vs. applied loads for all polysilicon materials.

The results showed that the fracture toughness ranges between 0.60 and 0.86 $MPa.m^{0.5}$ for polysilicon with highest hydrogen content (sample 1), and lowest hydrogen content respectively (sample 3); all mechanical properties for all tested samples are listed in Table 5-1. The change in toughness between the three batches is related to the amount of hydrogen in the production process, as mentioned in our earlier studies, where less solute hydrogen leads to higher toughness [1,3]. In these prior studies, it was shown that the hydrogen peak heights in FTIR spectrum are proportional to the amount of solute hydrogen present in the sample. Fig. 5-3 shows the FTIR spectrum, with the background subtracted, for wavenumbers between 1800-2400 cm^{-1}. The relative hydrogen peak heights are normalized by sample 1 with the highest hydrogen content, normalized hydrogen contents are 0.7 for sample 2 and 0.1 for sample 3 (the lowest hydrogen content); these values are reported in Table 5-1. The FTIR spectrum corresponds to hydrogen defects in Si, where four types of bonding occur. Si-H dangling bonds and vacancies have the highest concentration, and other types being less concentrated as Si-H bonds on the surface, isolated Si-H, and Si-O-H present on free surfaces. Other peaks of Si bonding that are not in 1800-2400 cm^{-1} range were identified to be Si-Si bonds or contamination of H_2O with Si [3].

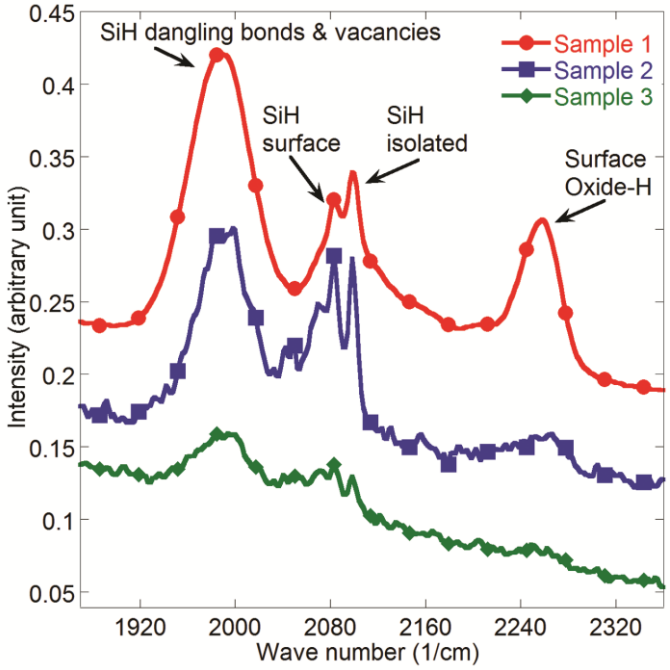

Figure 5-3. FTIR spectrum that shows hydrogen defects in silicon.

Table 5-1. Mechanical properties and crystallite sizes of all tested polysilicon materials measured using indentation techniques and XRD, respectively; about 45 tests were performed for each batch to calculate the average values and standard deviations.

Sample	Hardness (GPa)	Modulus (GPa)	Toughness ($MPa.m^{0.5}$)	Crystallite sizes (nm)	Relative hydrogen peak height
1	9.7 ± 0.4	164 ± 3	0.60 ± 0.05	30.0 ± 2.0	1
2	11.2 ± 0.7	157 ± 6	0.74 ± 0.03	30.0 ± 1.7	0.7
3	11.3 ± 0.8	145 ± 5	0.86 ± 0.03	31.3 ± 1.5	0.1

Peak broadening during X-ray diffraction was used to determine the crystallite sizes of polysilicon, and these values are listed in table 5-1. The three batches have the same crystallite size; thus this structural feature should have no impact on the change in fracture toughness in this current study.

For Rockwell hardness tests about 35 random tests were performed for each batch to have a rapid assessment of the fracture behavior on the granular polysilicon. Rockwell

failure load (RFL) was determined for each sample as the granule starts to fails at an applied load. This was done by visually examining all the samples at different applied loads, ranging from 15 to 75 kg. Granular polysilicon with the lowest toughness (sample 1) failed at applied loads of 30-45 kg, the one with medium toughness (sample 2) failed at 45-55 kg, and the one with the highest toughness failed at 55-60 kg. Rockwell hardness results and Vickers indentation results match with each other regarding the fracture behavior of the three polysilicon batches. Granular polysilicon with an average diameter of 1.8-1.9 mm failed at lower loads than the ones with an average diameter of 2.0-2.5 mm. All Rockwell test results are summarized in table 5-2. Within a given batch the failure on all tested beads occurred in the range reported; there was no evidence of failure in a small number of beads at a lower load (or a higher load).

Table 5-2. Minimum Rockwell failure load for tested samples at certain range of granular diameter.

Granular diameter (mm)	Rockwell failure load (kg)		
	Sample 1	Sample 2	Sample 3
1.8-1.9	30	45	55
2.0-2.5	45	55	60

Fig. 5-4 shows optical images of different crack and failure morphologies at specific applied loads using the Rockwell test. A small crack is initiated on sample 3 when 30 kg load is applied (Fig. 5-4a), a bigger crack is elongated when the load is increased to 45 kg (Fig. 4b), and it finally breaks the particle when a 60 kg load is applied (Fig. 5-4c). For sample 2, which is less tough, the granule fractured at an applied load of 55 kg (Fig. 5-4d), while the least tough material failed at 45 kg (Fig. 5-4e) and extensively shattered, as

in Fig. 5-4f; the granular polysilicon shown in Fig. 5-4(a-f) are in the size range of 2.0-2.5 mm in diameter.

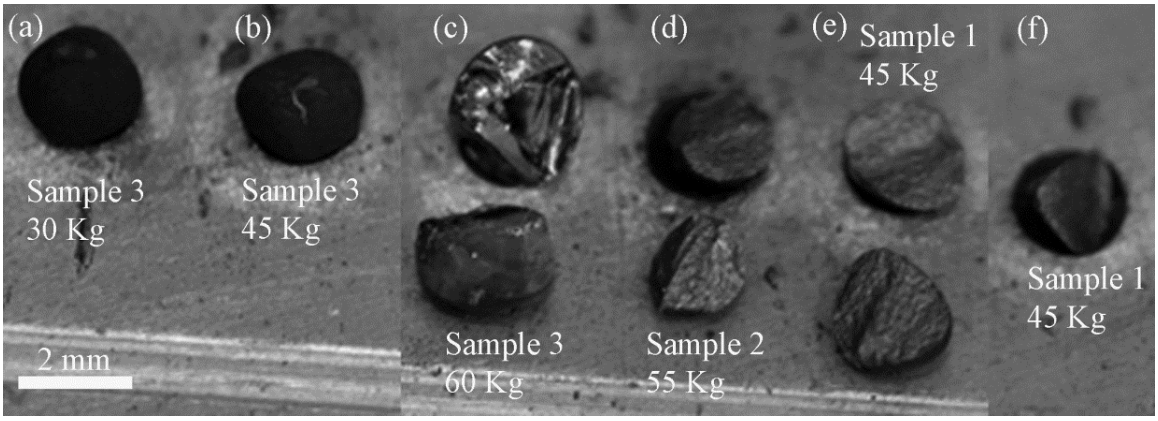

Figure 5-4. Optical images showing Rockwell test, where sample 3 only shows some cracks at 30 and 45 kg (a and b) and breaks at 60 kg (c), sample 2 breaks at 55 kg (d), sample 1 beaks at 45 kg (e and f).

Fig. 5-5 shows the most common fracture behavior that was observed on the different batches when applying a Rockwell test. All samples show a certain path of crack propagation at applied load of 15 kg, where it elongates more while unloading. Samples 1 and 2 break during unloading at 30 kg, while sample 3 has an elongation in the crack. At 45 kg sample 1 breaks during loading, and shatters during unloading, while sample 2 breaks during unloading only. Sample 1 cannot withstand more than 45 kg load without significant fragmentation, while sample 2 fails at 55 kg and fragments at 60 kg, and sample 3 fails at 60 kg and fragments at 75 kg.

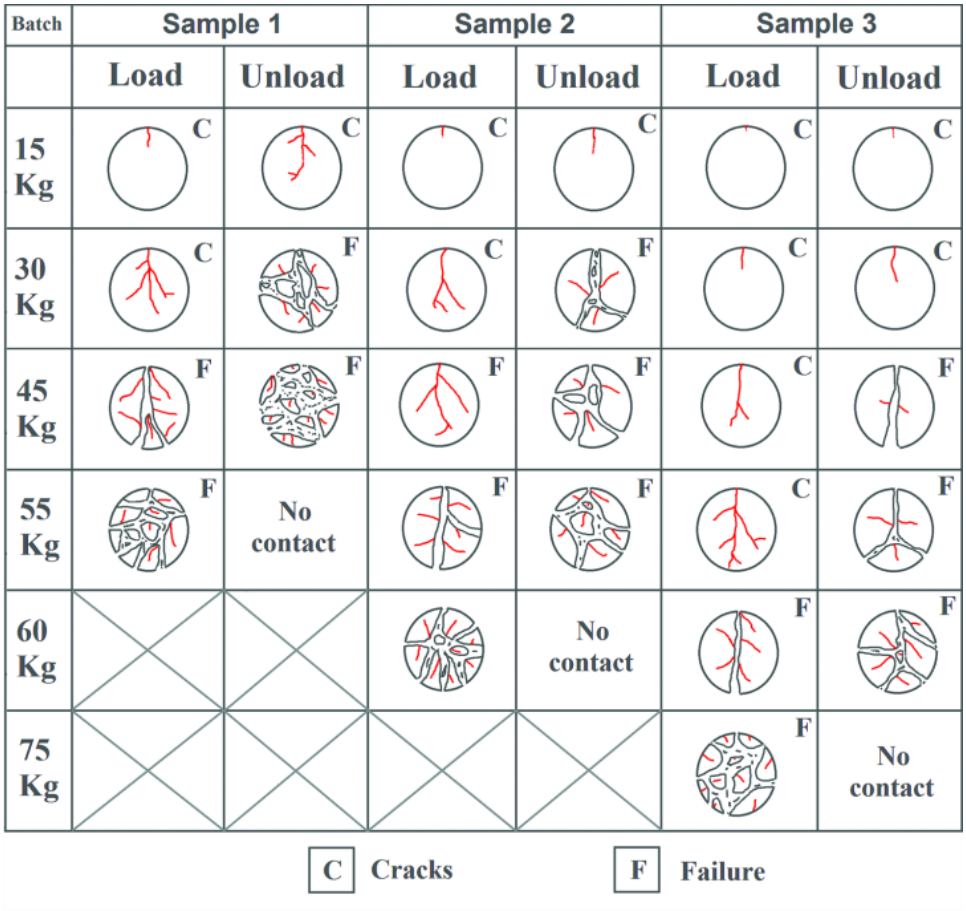

Figure 5-5. Schematic drawing showing the fracture behavior of granular polysilicon using Rockwell test.

In order to express the relationship between the Rockwell hardness test procedure and the toughness values, an approach has been identified similar to that of Ghadiri & Zhang, where they have the attrition parameter identified as in Eq. 1 [14,15]. However, in this case the modified dimensionless attrition propensity parameter (ή) depends only on the diameter of the granular polysilicon (*l*), the measured hardness (*H*), and the fracture toughness calculated above (*T*). This parameter is defined as

$$\acute{\eta} = \frac{lH^2}{T^2} \qquad \text{(Eq. 5-8)}$$

Fig. 5-6 shows the Rockwell failure load vs. the attrition propensity parameter for the three samples at three different granular sizes. Polysilicon with a lower toughness has a higher attrition parameter, and smaller sized granular Si shows lower attrition parameter (as would be expected from [13,14]).

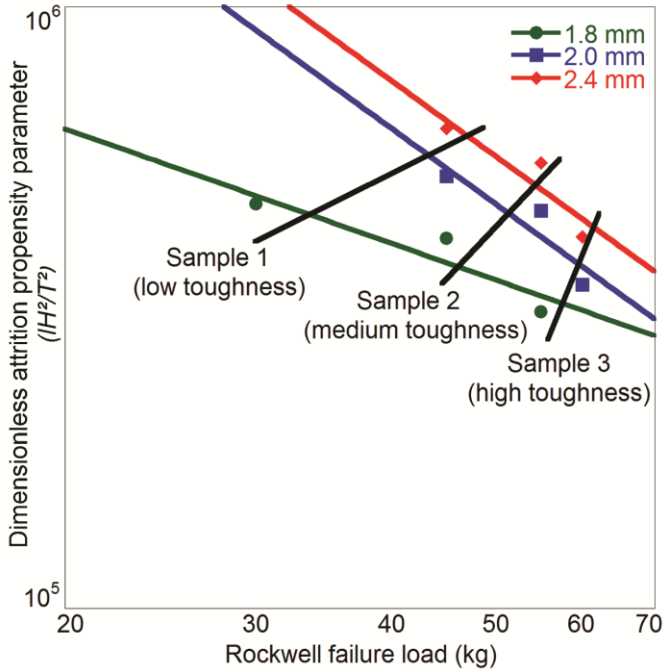

Figure 5-6. Attrition propensity parameter vs. Rockwell failure load. Low toughness polysilicon shows higher attrition compared to high toughness ones, and smaller granular shows lower attrition compared to larger ones.

Another way to show the relationship between toughness measurements and *RFL* is shown in Fig. 5-7, where a linear relationship is expressed by plotting T vs. RFL/l^2. This is shown over a range of granular diameter sizes between 1.8-2.5 mm.

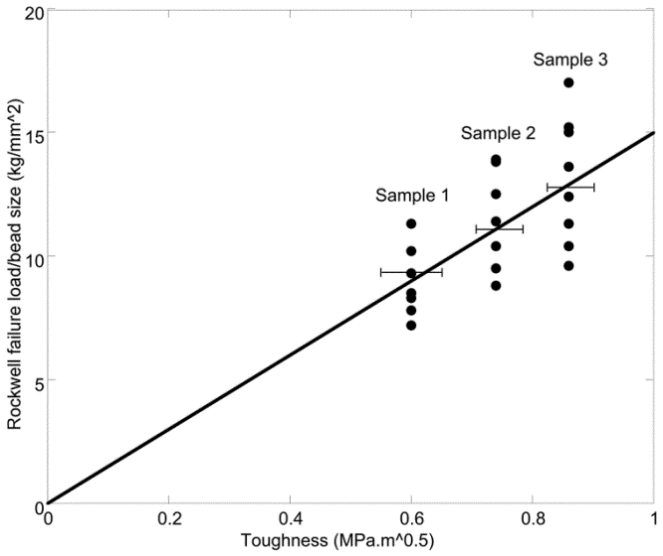

Figure 5-7. Linear relationship between toughness and Rockwell failure load.

SEM was used to study the microstructural behavior of granular polysilicon. The cross-section of polysilicon granular as shown in Fig. 5-8a has ring structure morphology because of the porosity in the material. Fig. 5-8a and 5-8b shows the distribution of the pores forming the rings, where our previous work measured the volume percent of the pores to range between 1 to 4 % in polysilicon and their sizes ranges between 0.1 to 5 μm in diameter [19].

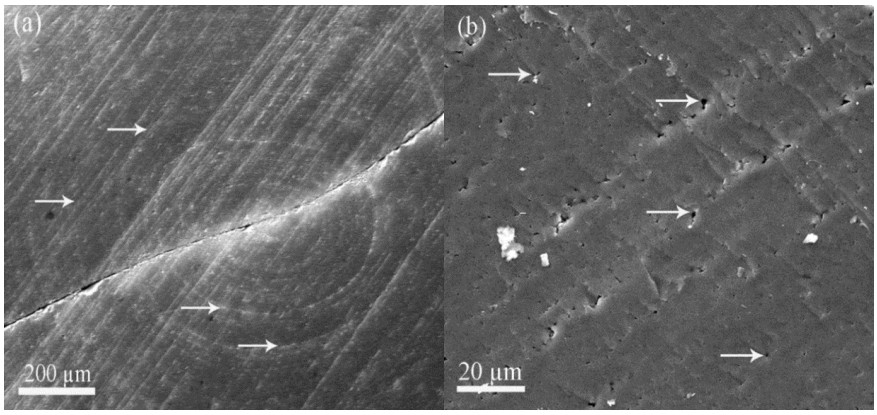

Figure 5-8. SEM images showing rings structure of the formed pores (a), and distribution of pore sizes (b); noted in arrows.

It was verified in our earlier studies that crack morphology in Vickers microindentation is not affected by fine porosity presented in the material [1]; this is also shown in Fig. 5-2a where the cracks are not influenced by any of the pores presented in the sample. In this paper we analyzed the effects of pores on fracture behavior on polysilicon under Rockwell applied load. Fig. 5-9a shows SEM image of a broken granular sample with the propagation of crack from the contact surface to the center with no influence from the pores. The crack continues its path and does not show any significant deviations by any of the pores. Fig. 5-9b with higher magnification shows the formation of rings along the pores with the propagation of the crack that passes through them without any changes in its morphology. This verifies that on both mico-scale and macro-scale load tests, there is no measureable influence of the pores on the fracture behavior of polysilicon.

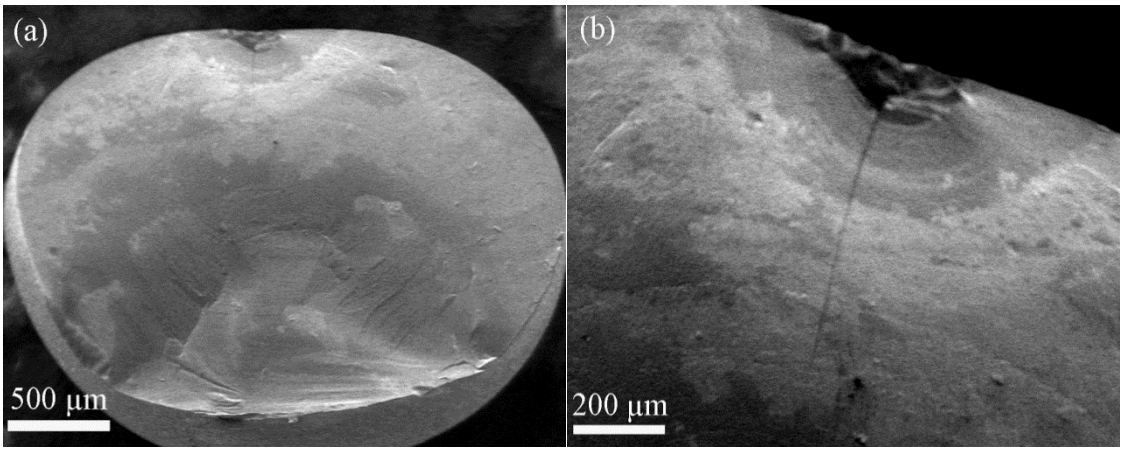

Figure 5-9. SEM images of the fractured beads at the applied Rockwell failure load.

5.4. Conclusions

The fracture behavior of granular polysilicon follows a similar trend when using a mirco-scale (Vickers) and macro-scale (Rockwell) indentation techniques. Materials with low fracture toughness (0.60 $MPa.m^{0.5}$) were able to withstand up to 45 kg load, while

materials with higher fracture toughness (0.86 MPa.$m^{0.5}$) withstood up to 60 kg load. All tested materials have same grain size, and therefore changes in toughness are ascribed solely to changes in solute H content. Porosity on the order of 1-4% does not influence the crack morphology on either the micro or macro-scale tests. The use of a simple Rockwell hardness test is an efficient qualitative technique for the rapid assessment on the fracture behavior of polysilicon used as a precursor to solar cell silicon. Rockwell hardness testing equipment can be used to assess the failure behavior of polysilicon grown for the solar market via fluidized bed reactors by testing individual granules, with no need for any sample preparation. By simply applying different loads and observing the failure mechanism of the material, a correlation to the fracture toughness can be made, and an estimate of attrition behavior determined. This method allows for rapid assessment and quality control of silicon granular products, and could be extended to other brittle granular materials.

Acknowledgments

We would like to thank REC Silicon, Moses Lake WA, for the financial support of this research, and in particular Matthew Miller for his helpful discussions of the FBR process. Also, we thank MM Dahl for the images in Fig 8.

Bibliography

1. Zbib M.B., Tarun M.C., Norton M.G., Bahr D.F., Nair R., Randall N.X., Osborne E. Mechanical properties of polycrystalline silicon solar cell feed stock grown via fluidized bed reactor. *J. Mater. Sci.* 45, 1560-1566 (2010).
2. Dahl M.M., Bellou A., Bahr D.F., Norton M.G., and Osborne E.W. Microstructure and grain growth of polycrystalline silicon grown in fluidized bed reactors. *Journal Crystal Growth.* 311, 1496-1500 (2009).
3. Zbib M.B., Norton. M.G., Bahr D.F. Effect of solute hydrogen on toughness of feedstock polycrystalline silicon for solar cell applications. Scripta Mater. 67, 756-759 (2012).
4. Fancher R.W., Watkins C.M., Norton M.G., Bahr D.F., Osborne E.W. Grain growth and mechanical properties in bulk polycrystalline silicon. *Journal of Materials Science*. 36, 5441-5446 (2001).
5. St. John C. The brittle-to-ductile transition in pre-cleaved silicon single crystals. *Philosophical. Magazine.* 32, 1193–1212 (1975).
6. Brede M. & Haasen P. The brittle-to-ductile transition in doped silicon as a model substance. *Acta Materialia*. 36, 2003-2018 (1988).
7. Hirsch P.B., Roberts S.G., Samuels J. The brittle ductile transition in silicon, 2. Interpretation. *Proc. R. Soc. Lond. A.* 421, 25-53 (1989).
8. Chen C.P., Leipold M.H. Fracture toughness of silicon. *American Ceramic Society. Bulletin*. 59, 469–472 (1980).
9. George A., Michot G. Dislocation loops at crack tips: nucleation and growth-an experimental study in silicon. *Materials Science and Engineering A*. 164, 118-134 (1993).

10. Ericson F., Johansson S., Schweitz J.A. Hardness and fracture toughness of semiconducting materials studied by indentation and erosion techniques. *Materials Science and Engineering A.* 105, 131-141 (1988).

11. Ebrahimi F., Kalwani L. Fracture anisotropy in silicon single crystal. *Materials Science and Engineering A.* 268, 116-126 (1999).

12. Bemrose C.R., Bridgwater J. A review of attrition and attrition test methods. *Powder Technol*. 49, 97–126 (1987).

13. Meier M., John E., Wieckhusen D., Wirth W., Peukert W. Influence of mechanical properties on impact fracture: Prediction of the milling behaviour of pharmaceutical powders by nanoindentation. *Powder Technol.* 188, 301–313 (2009).

14. Ghadiri M. and Zhang Z.. Impact attrition of particulate solids, Part I: a theoretical model of chipping. *Chem. Eng. Sci.* 57, 3659–3669 (2002).

15. Zhang Z. and Ghadiri M. Impact attrition of particulate solids, Part II: experimental work. *Chem. Eng. Sci.*, 2002, vol. 57, pp. 3671–3686.

16. Morris D.L., Cook R.F. Radial fracture during indentation by acute probes: I, description by an indentation wedging model. *Int. J. Fract.* 136, 237-264 (2005).

17. Oliver W.C., Pharr G.M. An improved technique for determining hardness and elastic modulus using load and displacement sensing indentation experiments. *J. Mater. Res.* 7, 1564-1583 (1992).

18. Williamson G.K., Hall W.H. X-ray line broadening from filed aluminum and wolfram. *Acta Metall.* 1, 22-31 (1953).

19. Zbib M.B., Dahl M.M, Sahaym U., Norton M.G., Osborne E.W., Bahr D.F. Characterization of granular silicon, powders, and agglomerates from a fluidized bed reactor. *Journal of Materials Science.* 47, 2583–2590 (2012).

CHAPTER 6. NEW PULVERIZATION PARAMETER DERIVED FROM INDENTATION AND DYNAMIC COMPRESSION OF BRITTLE MICROSHPERES

M.B. Zbib, N.D. Parab, W.W. Chen, D.F. Bahr

Abstract

Particulates may experience dynamic compression loading during materials handling and processing, which in turn can lead to fracture of the particles. In this study, the dynamic fracture behavior of microspherical particles of soda lime glass (SLG), polycrystalline silica, polycrystalline silicon, barium titanate glass (BTG) and yttrium-stabilized zirconia (YSZ) was characterized with high speed, *in situ* X-ray phase-contrast imaging to examine the failure mechanisms *in situ* for spheroidal particles with diameters (d) from 600 to 2000 μm under dynamic compression. Nanoindentation was used to measure the hardness (H) and elastic modulus (E), and microindentation was used to measure the fracture toughness (T) of the materials. Based on the experimental results, a new pulverization parameter was proposed to predict the failure mechanism of the materials given by: $\mathcal{P}=Hd/TE^{5/3}$. Three different failure mechanisms were identified: comminution (pulverization), major cracking, and single cracking corresponding to high, medium, and low $\mathcal{P}$ values respectively.

6.1. Introduction

Particles or granular solids of brittle materials are subjected to self-impact loading during materials processing, transportation, drilling, blasting, and rapid penetration loading such as ballistic impact. The resulting dynamic compressive loading can lead to a wide range of deformation and fracture behaviors in the particles. The integrity of the granular solid after compression plays a significant role in both the subsequent processing and the energy absorption capabilities of the material. There are established methods in the literature to analyze the fracture energy distribution of particles using quasi-static single particle tests (crushing tests) and studying the breakage of hard particles under controlled loading conditions [1]. Single particle testing is not restricted to inorganic solids; testing of crystalline organic substances to study the milling behavior has compared particle fracture to localized indentation fracture techniques. This has shown that the absorption energy and the resistance to fracture of a particulate can be related to a brittleness index (often defined as a ratio of hardness to fracture toughness) [2].

The behavior of spherical particles under impact loading has been studied using various experimental methods. In several studies, a spherical particle was impacted against a rigid target at a high velocity [3-9] Andrews and Kim observed that the particles fracture upon impact only if the impact velocity is higher than a certain threshold velocity [6]. Salman et al. reported the cracking behavior for various brittle particles including PMMA and soda-lime glass using the post-mortem observation of the fragments collected after the impact [9]. *In-situ* observation of failure behavior has been reported for the glass spheres, where they were observed to undergo explosive fragmentation upon impact on a hard anvil [6,7]. Several studies have utilized particle impact experiments to

obtain the probability of particle failure in an aggregate particulate solid [10-12]. Dynamic diametral compression using a drop tower testing machine has also been used to apply impact loading [13,14]. Chau et al. observed plaster particles failing in two hemispheres or three ‘orange slices’ under dynamic diametral compression [13]. In the same paper, Chau et al. reported that the failure modes in the particle under dynamic compression were identical to those observed under static compression [13].

The aforementioned single particle experiments cannot account for the effects of particle-particle contacts which are prevalent in granular solids. Also, it has been impossible to observe the *in situ* failure mechanisms for the opaque particles. However, a high speed X-ray phase contrast imaging (PCI) technique synchronized with Kolsky bar loading mechanism was recently developed to observe the failure modes in two contacting brittle particles under dynamic compression [15,16]. In previous studies, silica sand particles were observed to fracture exclusively in the pulverization failure mode when dynamically compressed [15].

While identifying failure modes using both *in situ* and post-test characterization is beneficial, the ability to predict failure modes provides guidance for designing both energy absorbing systems as well as predicting morphological changes during powder processing. Ghadiri and Zhang established an experimental and theoretical model of impact attrition of particulate solids for semi-brittle failure [17,18]. They identified a dimensionless attrition propensity parameter that is related to impact conditions (impact velocity) and material properties (particle density, particles size, hardness, and fracture toughness) [17,18]. Zbib and Bahr recently identified a similar dimensionless attrition propensity parameter for spherical granular polycrystalline silicon which is related to the

shape (and therefore stresses at a fixed loading condition), hardness, and elastic modulus of the silicon [19], where lower toughness or larger diameter particles exhibited a higher attrition parameter. However, these attrition parameters only discuss the likelihood of particle size reduction through fracture and do not address the particle failure morphology explicitly. Another concern about studying the fracture behavior of brittle microspheres such as silica and silicon is related to safety and health issues. Studies showed that the operators of sand blasters and stone cutting systems can be subjected to fine silica particulates which can lead to silicosis and lung cancer, both deadly lung diseases [20,21]. If the fracture behavior of particles during impact loading and materials processing was better understood, predictions of the dust generated during these processes might be used to limit worker exposure to harmful particulate matter.

In this paper the fracture behavior of micro-spherical particles made up of polycrystalline silica, soda lime glass (SLG), polycrystalline silicon, barium titanate glass (BTG) and yttrium-stabilized zirconia (YSZ) under dynamic compression is discussed. Nanoindentation and microindentation were used to study the quasi-static mechanical properties, while the failure mechanisms under dynamic compression were investigated using high speed X-ray PCI. Using these complementary techniques a new pulverization model is proposed to better describe the fracture behavior of granular solids under self-impact loading.

6.2. Materials and Method

Nominally spherical particles composed of five different brittle materials were chosen for this study. Materials were selected to provide a range of materials properties as well as variations in particle size. Material, size and the vendor for each type of

particle are summarized in Table 6-1. For silicon, BTG, YSZ and silica, both contacting particles were selected from a single monodisperse particle size distribution. For SLG, particles were selected from three different monodisperse particle size distributions. Both contacting particles for a given experiment were chosen from the same distribution. Samples were imaged using scanning electron microscopy to verify they were primarily spherical, with simple aspect ratios of the plan view microscopy used to determine the aspect ratio of several representative particles.

Table 6-1: Material properties, particle size and vendor for each type of particle

Material	Particle size (μm)	Aspect ratio	Number of impact compression experiments	Vendor
Polycrystalline silicon	850-1100	1.02-1.21	27	REC Silicon (Moses Lake, WA)
Soda-lime glass (SLG)	600-2000 1000-1150 1700-2000	1.00-1.02	10 13 13	Cospheric LLC (Santa Barbra, CA)
Barium titanate glass (BTG)	850-1000	1.02-1.18	5	Cospheric LLC (Santa Barbra, CA)
Yttrium stabilized Zirconia (YSZ)	850-1000	1.01-1.05	5	Cospheric LLC (Santa Barbra, CA)
Polycrystalline silica	600-710	1.03-1.18	11	U. S. Silica (Ottawa, IL)

The specimens used for measuring the mechanical properties of individual spherical particles were prepared using conventional grinding and polishing methods. The granular particles were mounted in epoxy and ground with 350 to 1200 grit silicon carbide abrasive paper, and then polished using diamond paste from 6 to 0.5 μm. These sample preparations were done only for Vickers indentation and nanoindentation tests. The high

speed impact experiments were performed on specimens with no prior sample preparation. In all cases the peak to valley roughness of the surface of the spheroidal particles was much less than (<5%) that of the radius, and while some particles are not perfectly spherical, for the purposes of this work a first order spherical radius that averages the diameters from the particle size distributions will be used to define particle size.

The hardness (*H*) and elastic moduli (*E*) of the five materials were determined using a Hysitron Triboindenter TI 950 to perform nanoindentation experiments in which the applied load, *F*, and indenter displacement are recorded throughout the test. Quasi-static testing was performed with maximum applied loads between 5000 and 8500 μN. All measurements (about 15 tests of each material) were done at areas smaller than any pore or defect spacing to avoid morphological influence on the measured materials properties. The Oliver and Pharr method was used to calculate the hardness and the modulus, where the contact area at the peak load and the slope during unloading were taken into consideration [22]. The elastic modulus was calculated using:

$$\frac{1}{E_R} = \frac{1-\nu_i^2}{E_i} + \frac{1-\nu_s^2}{E_s} \qquad \text{(Eq. 6-1)}$$

where E_R is the reduced modulus determined from the Oliver and Pharr analysis of the unloading slope, E_i is the modulus of the diamond indenter tip (1249 GPa), E_s is the elastic modulus of the sample, ν_i and ν_s are the Poisson's ratio of the diamond indenter tip (0.07) and the sample respectively. The hardness (*H*) is the ratio of peak indentation load (F_{max}) and the known projected area function at maximum load (*A*) which can be related

to the indenter displacement during the nanoindentation test. The hardness was calculated using

$$H = \frac{F_{max}}{A} \qquad \text{(Eq. 6-2)}$$

The quasi-static toughness was determined using a Vickers microhardness test, where loads between 0.49 and 4.9 N were applied to the samples, and an optical microscope was used to measure the crack sizes induced from the indentation experiment [23]. About 30 tests were performed on each material. The fracture toughness (*T*) of each material was determined using Vickers indentation induced fracture [23] by

$$T = \frac{\chi_r F}{c^{3/2}} \qquad \text{(Eq. 6-3)}$$

where *c* is the average crack radius, *F* is the applied load using a Vickers microindenter, and χ_r is a constant that depends on the specific material system

$$\chi_r = \xi\sqrt{\frac{E}{H}} \qquad \text{(Eq. 6-4)}$$

where *E* and *H* are the measured elastic modulus and hardness respectively, and ξ is an indenter invariant constant, which is equal to 0.016 for Vickers tip experiments [23].

The failure mechanisms of the particles under dynamic compression were investigated using a combination of a modified Kolsky bar setup and high speed synchrotron x-ray PCI at Advanced Photon Source (APS) beam line 32-ID-B at Argonne National Laboratory, Argonne, IL. This experimental method has been used to study the failure mechanisms in various materials including bone-tissue interfaces, polymer fibers, concrete and rocks, and glass plate [15,16,24]. The schematic of the experimental setup is presented in Figure 6-1.

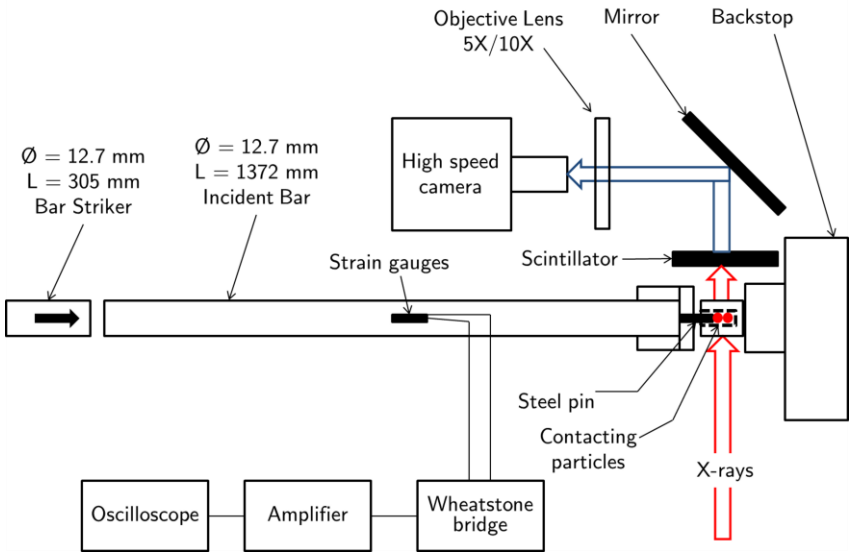

Figure 6-1: Schematic of high speed X-ray PCI experiments to observe the failure modes in contacting spherical particles under dynamic compression.

Kolsky bar is commonly used to characterize material properties at 10^2–10^5 s^{-1} strain rates [25,26]. In this study, a modified Kolsky bar technique was used to impose controlled dynamic compression on two contacting particles. The transmission bar in the conventional Kolsky bar apparatus was replaced with a heavy aluminum backstop due to space constraints in the APS X-ray hutch. A high intensity polychromatic X-ray beam was passed through the particles as they were compressed. After passing through the particles, the X-ray signal was converted to visible light using a scintillator (single crystal $Lu_3Al_5O_{12}$:Ce). The visible light images on the scintillator were relayed to a high speed camera using a 45^0 mirror, a microscope objective, and a tube lens. Photron Fastcam SA1.1 high speed digital camera containing a 12-bit CMOS sensor was used to capture images at various frame rates and frame sizes. One of the limitations of the camera was that the frame size reduced as the frame rate was increased.

Two spherical particles were constrained in a custom made aluminum sample holder with the compression loading imposed on the particles using a flat faced steel gage pin. To prevent the interaction of the particles with holder wall, the aluminum holder was machined with a slightly larger inner diameter than the nominal diameter of the particles. The experimental sequence started with a manual start signal that launched the striker bar towards the incident bar. The impact of the striker with the incident bar generated a compressive stress wave in the incident bar. The compressive wave was sensed by the strain gauges on the incident bar that subsequently triggered the camera. The stress wave continued to propagate to the end of the incident bar where it pushed the steel pin onto two contacting particles at a constant speed of 4.9 – 5.1 ms^{-1}. The high intensity x-ray beam passes through the particles as they were being compressed. Subsequently, the deformation and damage of the particles was recorded by the scintillator-camera system. For all particles, at least 5 experiments were conducted to ensure repeatability. Numbers of experiments for each particle type are presented in Table 6-1.

6.3. Results and Discussion

6.3.1. Particle Shapes

The aspect ratio of the particles was measured to better identify their shapes. This ratio was identified as the ratio of the largest projected diameter to the smallest projected diameter of the particle that could be imaged using scanning electron microscopy of at least 5 representative particles. SLG and YSZ have aspect ratios that range between 1.00 and 1.05; they are effectively spherical. However, the aspect ratios of silicon & silica can reach up to 1.21, showing a larger deviation which may be present in the projected x-ray imaging used to examine *in situ* particle fracture. The aspect ratios of BTG range

between 1.02 and 1.18. The ranges of aspect ratios measurements of each material are listed in Table 6-1. The roughness of all particles was ignored in the current study as in all cases it is ~ 5% of less of the radius or the nominal diameter of the particle.

6.3.2. Mechanical Properties

Both hardness and elastic modulus of each material did not vary significantly within a batch; the values are listed in Table 6-2. We have chosen to present the measure of material toughness as T, rather than reporting a mode I fracture toughness (K_{IC}) because well-defined pre-cracks and pure mode I opening are not present in the indentation fracture method. For further details, Morris and Cook describe how T is an appropriate surrogate for using indentation induced fracture in place of a more well defined stress state during pure mode I or II toughness testing [23]. The average crack size vs. applied load was plotted as shown in Figure 6-2, where equation 3 was used to fit the data for each material to determine T. The deviations at low loads are likely due to the difficult evaluation of the crack sizes at small loads, and the inhomogeneity of the product. One of the materials, polycrystalline silicon, does exhibit approximately 4% porosity, however prior studies have shown that the pores present in this material did not show any significant effect on the crack morphology nor the measured toughness [19]. The measured toughnesses of all the materials are listed in Table 6-2.

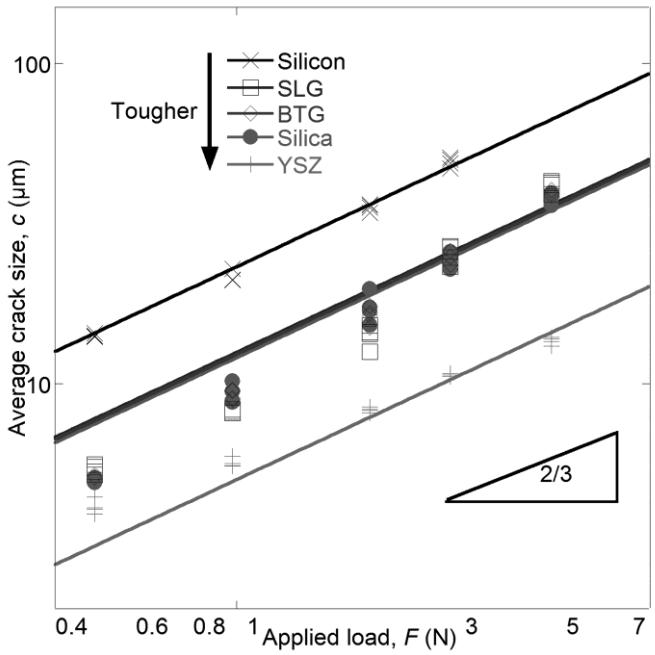

Figure 6-2: Average crack size *c* (μm) vs. applied loads (*F*) using Vickers indentation test for all materials in the current study, where equation 3 is fit to the 2/3 power. Note that this is a logarithmic scale.

6.3.3. Failure Modes

The high speed X-ray PCI technique was used to identify the failure modes in different particles. The scintillator-high speed camera setup captured the images in 16-bit greyscale format. The raw images were adjusted for the contrast and brightness such that cracks can be easily identified using ImageJ software [27]. Following contrast and brightness adjustment, images were colorized using a native colorization scheme in the ImageJ software package (Look up table: Fire) to make the failure process easier to visualize. Figures 6-3 to 6-7 show the failure process in various particles under dynamic compression. The glass particles and silica sand particles showed what is more commonly observed in comminution failure mode, with a significant decrease in particle size after impact. Polycrystalline silicon and barium titanate glass particles showed major

cracking between contacts prior to failure, with a particle size reduction after impact to approximately 10% of the initial particle size. YSZ particles displayed a single crack in one of the particles which separated the particle into two parts, effectively only reducing the particle size by 50%.

Figure 6-3 shows the failure modes for the soda lime glass particles. Initially, two particles were touching and no compression was applied. As the pin compressed the particles, conical cracks initiated from the contact (Figure 6-3, t = 22.1 μs). As the particles were compressed further, one of the particles pulverized violently (Figure 6-3, t = 66.3 μs). Silica sand particles displayed similar behavior (Figure 6-4). Interfacial cracks initiated at the contact when the particles were compressed (Figure 6-4, t = 37 μs). The cracked particle subsequently pulverized (i.e. resulting powder size less than 1% of the initial radius, more similar to what might be expected through significant comminution during particle size reduction processing) when compressed further (Figure 6-4, t = 74 μs).

Both polycrystalline silicon and BTG particles showed a markedly different failure behavior. The failure process for silicon particles is presented in Figure 6-5, we will refer to this mode as “major cracking”. When the particles were compressed, a finite number of major cracks formed in one of the particles (Figure 6-5, $t \approx$ 18.5 μs). On further compression, the cracked particle fractured into several large fragments and a large number of very small fragments (Figure 6-5, $t \approx$ 37 μs). The second particle remained intact till the cracked particle fractured completely. BTG particles also showed major cracking failure mode under dynamic compression (Figure 6-6). In BTG particle

compression experiments, the second particle also showed major cracking after sufficient compressive loading had been applied (Figure 6-6, $t \approx 100$ μs).

YSZ particles displayed a remarkably different behavior than the other particles examined in this study (Figure 6-7). Upon dynamic compression a single crack developed between the contacts (meridonial crack) in one of the particles (Figure 6-7, $t \approx 56$ μs). This crack fractured the particle into two parts when the particles were compressed further (Figure 6-7, $t \approx 74$ μs). After breaking, one of the parts of the fractured particle was compressed further between the intact particle and the compressing pin.

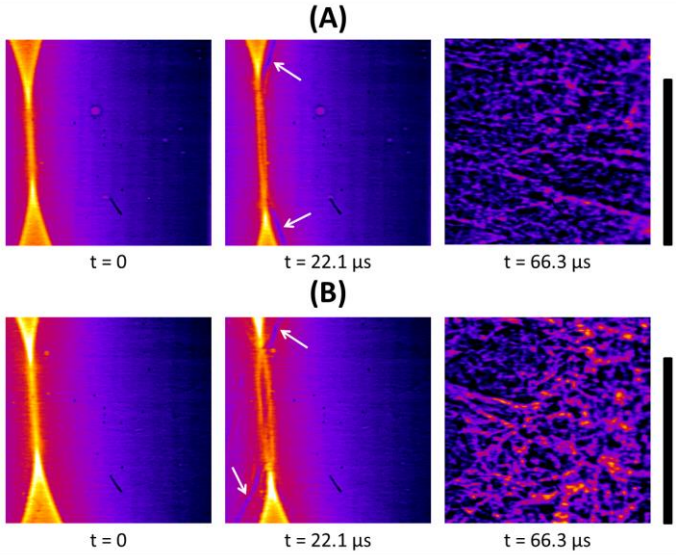

Figure 6-3: X-ray images of two contacting soda-lime glass particles under dynamic compression observed in two different experiments. In both experiments, conical cracks are observed at the contact (shown here with arrows at $t = 22.1$ μs) on compression. As the particles are compressed further, they comminute ($t = 66.3$ μs); t is the time of impact. Scale bars are 500 μm.

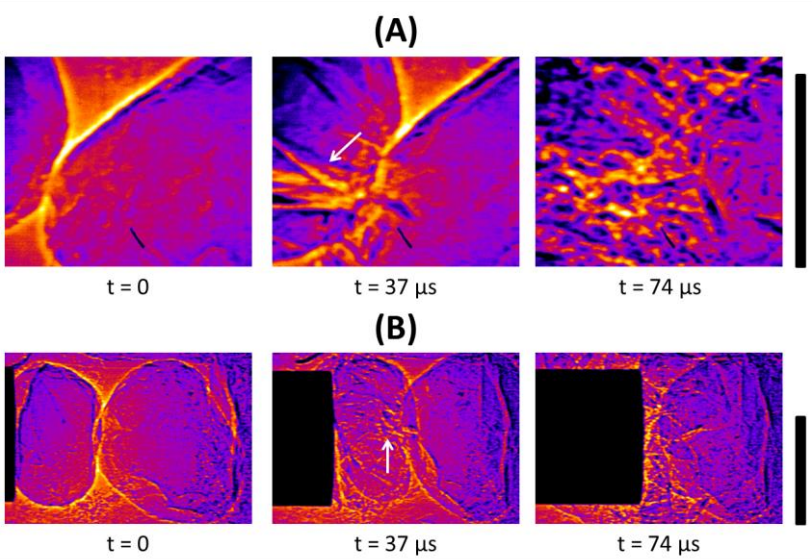

Figure 6-4: X-ray images of two contacting silica sand particles under dynamic compression observed in two different experiments. In both experiments, interfacial cracks are observed to initiate at the contact (shown here with arrows at t = 37 μs). As the particles are compressed further, they comminute (t = 74 μs); t is the time of impact. Scale bars are 500 μm.

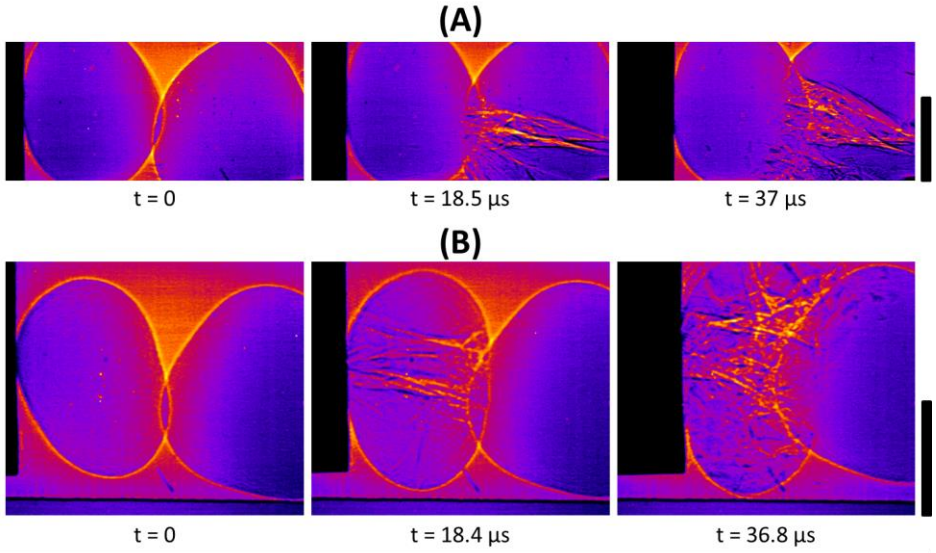

Figure 6-5: X-ray images of two contacting polycrystalline silicon particles under dynamic compression observed in two different experiments. In both experiments, major cracking from contact to contact is observed in one of the particles ($t \approx$ 18.5 μs). As the particles are compressed further, major cracks open up to fracture the particle ($t \approx$ 37 μs); t is the time of impact. Scale bars are 500 μm.

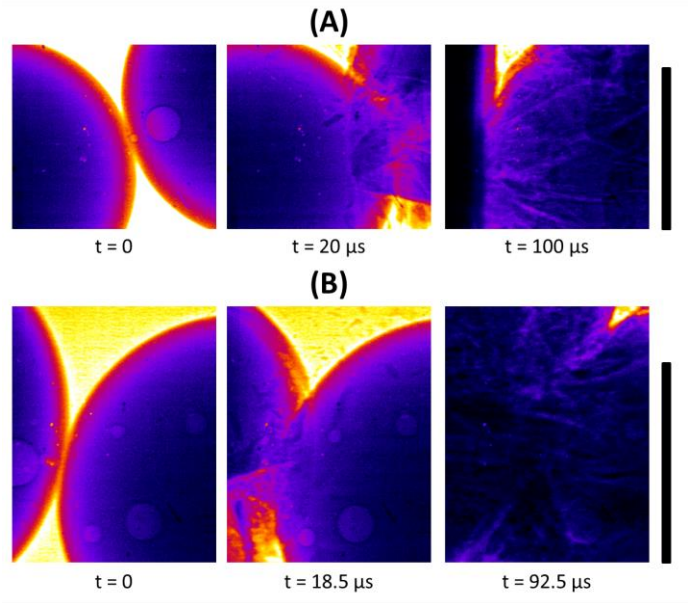

Figure 6-6: X-ray images of two contacting Barium Titanate glass particles under dynamic compression observed in two different experiments. In both experiments, finite numbers of cracks develop in one of the particles ($t \approx 20$ μs). As the particles are compressed further, major cracks open up to fracture the particle along with several cracks in the second particle ($t \approx 100$ μs); t is the time of impact. Scale bars are 500 μm.

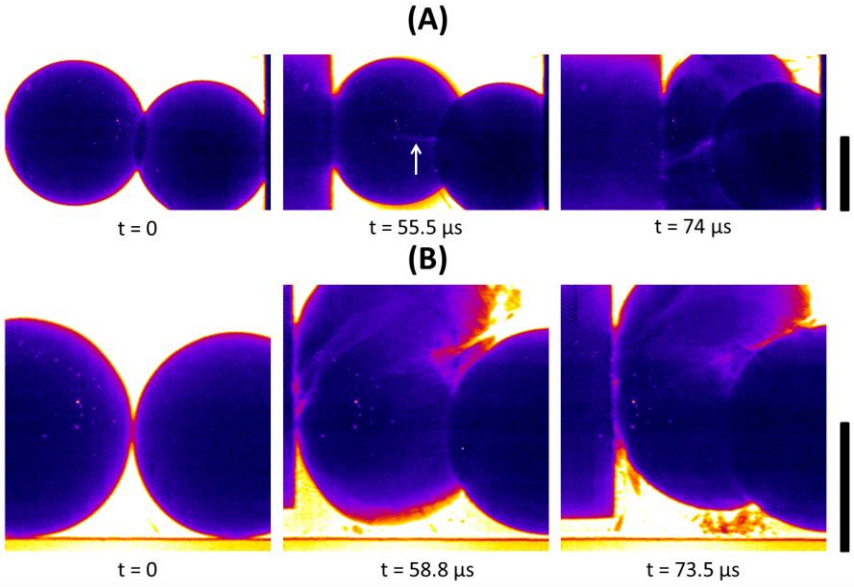

Figure 6-7: X-ray images of two contacting Yttrium stabilized zirconia particles under dynamic compression observed in two different experiments. In both experiments, a single crack propagates in one of the particles (depicted by the arrow at $t \approx 55$ μs). As the particles are compressed further, single crack opens up for break the particle in two parts ($t \approx 74$ μs); t is the time of impact. Scale bars are 500 μm.

6.3.4. Pulverization Parameter

As described in the previous section, different particles display widely different failure mechanisms under similar compressive loading. Here we propose an analytical approach to express the relationship between the properties measured using quasi-static indentation techniques (Hardness, modulus, and toughness) and the dynamic compression experiments (failure mechanism). This approach is similar to the brittleness index (B_i) [2] and to Ghadiri & Zhang's dimensionless attrition parameter (η) [17,18], where different parameters were identified respectively as:

$$B_i = \frac{H}{T} \qquad \text{(Eq. 6-5)}$$

$$\eta = \frac{\rho v^2 l H}{T^2} \qquad \text{(Eq. 6-6)}$$

where T is the fracture toughness, H is the hardness, l is a characteristic particle size, v is the impact velocity (5 m/s for all tests taken from the current X-ray experiments), and ρ is the particle density.

Although these parameters can accurately predict the propensity for particle failure in particulate materials, they are unable to predict the failure modes observed in this study. The brittleness index and Ghadiri and Zhang's dimensionless attrition parameter (η) for the particles used in this study are plotted in Figure 6-8(b). For these parameters to describe the morphological failure process, it is expected that the parameter should show a clear trend as the severity of cracking damage increases in the particle. Hence, if these parameters were sufficient to describe the failure mode, the parameter should show either uniformly increasing or decreasing trend as the material is changed from SLG to silica to

silicon to BTG and finally to YSZ. However, the two parameters defined in the literature are almost equal for SLG and BTG and show a maximum for silicon.

To properly explain the observed trend in comminution behavior across material type, a modified attrition propensity parameter, defined here as the pulverization parameter ($\mathcal{P}$) has been identified which depends on the diameter (d), the hardness (H), elastic modulus (E), and toughness (T) of the spherical particle. The motivation for the parameter is as follows. We begin with the assumption that $\mathcal{P}$ should be larger as the propensity to pulverize and form smaller final particle sizes during particle fracture increases. If H is higher, then dislocations are more difficult to move in the structure of the material (or other plastic processes such as twinning or densification are similarly more difficult to occur) and less energy is expended in plastic deformation, so $\mathcal{P}$ increases and therefore:

$$\mathcal{P} \propto H \qquad \text{(Eq. 6-7)}$$

Similarly, when T is higher, the particles exhibit less fracture, so it is less likely for the particles to pulverize and therefore:

$$\mathcal{P} \propto \frac{1}{T} \qquad \text{(Eq. 6-8)}$$

The strain energy that is added to the particle is proportional to E at a given strain. The strain energy is inversely related to comminution of the material and therefore:

$$\mathcal{P} \propto \frac{1}{E} \qquad \text{(Eq. 6-9)}$$

The relative displacement between the centers of two particles is related to the contact area and the particle radius using standard Hertzian contact mechanics, where the contact area is inversely proportional to the maximum pressure [28]. When the contact area increases, comminution decreases since the maximum pressure also decreases. However,

the contact area is proportional to the displacement which is proportional to ($1/E^{2/3}$) based on the Hertzian equation for the elastic contact of spheres [28], hence the modulus should be related to $\mathcal{P}$ in an additional term:

$$\mathcal{P} \propto \frac{1}{E^{2/3}} \qquad \text{(Eq. 6-10)}$$

Finally, we must consider the method by which the test was run. As this testing geometry is effectively a displacement imposed test with fixed grips (the test is not load controlled; in the impact conditions here, we assume there is overly sufficient loading capability present and the particles deform in a fixed grips condition to conform to the motion of the striker plate) the maximum pressure within a particle should scale with the particle diameter.

$$\mathcal{P} \propto d \qquad \text{(Eq. 6-11)}$$

The mean pressure (p_0) was calculated based on Hertz theory of elastic contact [28], which is related to the contact radius (a) that was measured from the high speed X-ray images when the two particles are in contact; we choose here the frame which exhibits the largest contact area between the particles prior to fracture; obviously this is an underestimate of the maximum mean pressure as the contact radius between the particles may continue to increase in the time interval between frames. However, to first order this should provide a reasonable estimate of pressure prior to fracture and a starting point for future method development. The mean pressure is

$$p_0 = \frac{4aE}{\pi d} \qquad \text{(Eq. 6-12)}$$

Combining equations (6-7) to (6-11), the pulverization parameter is defined as:

$$\mathcal{P} = \frac{Hd}{TE^{5/3}} \qquad \text{(Eq. 6-13)}$$

The results of calculation by equations 6-5, 6-6, 6-12, and 6-13 for each material are listed in Table 6-2.

Table 6-2: Mechanical properties and the comparison of the pulverization model to other models in literature of all tested materials measured using indentation techniques; between 15 and 30 tests were performed for each material to calculate the average values and standard deviations.

	SLG	Silica	Silicon	BTG	YSZ
Hardness, H (GPa)	6.5 ± 0.3	13.8 ± 0.6	9.7 ± 0.4	5.3 ± 0.3	16.0 ± 0.7
Elastic Modulus, E (GPa)	83 ± 6	111 ± 5	164 ± 4	77 ± 5	255 ± 7
Toughness, T (MPa.m^0.5)	1.28 ± 0.08	1.07 ± 0.04	0.60 ± 0.05	1.10 ± 0.07	5.69 ± 0.16
Mean pressure, p_0 (GPa)	19	25	78	13	104
Brittleness index [2]	$5.1x10^{3}$	$1.3x10^{4}$	$1.6x10^{4}$	$4.8x10^{3}$	$2.8x10^{3}$
Ghadiri & Zhang parameter [17,18]	$3.2x10^{8}$	$5.2x10^{8}$	$1.5x10^{9}$	$2.9x10^{8}$	$5.8x10^{7}$
Pulverization Parameter, $\mathcal{P}$ ($m^{0.5}/GPa^{5/3}$)	$4.2x10^{-3} \pm 1.5x10^{-4}$	$3.3x10^{-3} \pm 1.3x10^{-4}$	$3.0x10^{-3} \pm 1.3x10^{-4}$	$2.2x10^{-3} \pm 1.6x10^{-4}$	$2.1x10^{-4} \pm 3x10^{-5}$
Failure mode	Comminution	Comminution	Major cracks	Major cracks	Single crack

The pulverization parameter $\mathcal{P}$ values were divided into three different groups that match the three different failure mechanisms that were identified above. These different thresholds are shown in Figure 6-8a. High $\mathcal{P}$ values (> $3.0x10^{-3}$ $m^{0.5}/GPa^{5/3}$), correspond to comminution failure as seen in SLG and silica particles (i.e. a particle size reduction on the order of more than 95% from the initial spherical particle radius); small values (< $1.0x10^{-3}$ $m^{0.5}/GPa^{5/3}$) correspond to single cracking as seen in YSZ (i.e. the particle splits into two particles); medium $\mathcal{P}$ values correspond to the major cracking failure as seen in silicon and BTG (i.e. a particle size reduction between 50 and 90% from the initial

radius). Fig. 8b shows how other attrition parameters do not follow similar trend to the failure mechanisms under dynamic compression; similarly the mean pressure at failure initiation shown in Table 6-2 is not sufficient to describe the trend. Based on the identified failure mechanisms of the pulverization parameter, it is observed that different shapes exist in each category; for instance, SLG particles that are spherical have similar failure mechanism to silica particles that are more ellipsoidal, suggesting that this newly proposed parameter $\mathcal{P}$ is relatively robust in describing the reduction in particle size during self particle impact and, to first order, not particularly sensitive to the spheriodicity of the sample.

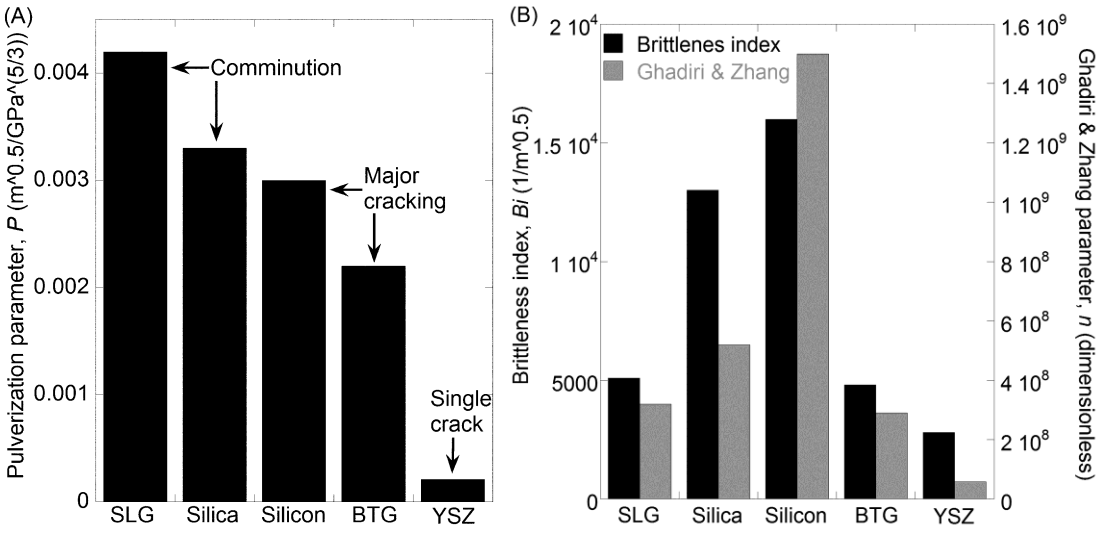

Figure 6-8. (a) Histogram showing the three different failure mechanisms corresponding to the pulverization parameter values for all the materials, and (b) the comparison to other existing parameters that do not match the failure mechanisms results.

The importance of this new pulverization model is to address the influence of strain energy added to the system as particles compress, along with the hardness and toughness of the material on the overall particle failure morphology. The three thresholds that have been identified in this study do not match with the calculations based on the other

published parameters nor the mean pressure at failure; therefore, it would not be possible to predict the observed varied failure mechanisms based on the previously published parameters. Combining indentation techniques and dynamic compression experiments to develop this new model is a valuable way to classify different materials for design and application purposes; the model has predictive capabilities that can be exercised for other brittle spherical particles systems.

6.4 Conclusions

In this study, a new attrition model was proposed to better describe the morphological fracture mechanisms and failure behavior of brittle microspheres under high strain rate dynamic loading. This phenomenological model is represented by a pulverization parameter ($\mathcal{P}$) that is related to the hardness (H), elastic modulus (E), fracture toughness (T), and the size (d) of the particles assuming fixed grips loading conditions with excessive load applied. It is identified as

$$\mathcal{P} = \frac{Hd}{TE^{5/3}} \qquad \text{(Eq. 6-11)}$$

Three different failure mechanisms have been identified based on the relationship between the dynamic compression experiments and the indentation measurements. These mechanisms are comminution, major cracking, and single cracking for high, medium, and low $\mathcal{P}$ values respectively. The model is shown to accurately predict failure morphology for spherical particles undergoing high strain rate compressive loading.

Acknowledgments

We appreciate professional help from A. Deriy with certain technical and safety aspects of our experiments at the APS. Use of the Advanced Photon Source, an Office of Science User Facility operated for the U.S. Department of Energy (DOE) Office of

Science by Argonne National Laboratory, was supported by the U.S. DOE under Contract no. DE-AC02-06CH11357. This research was partially supported by the ONR Grant N00014-14-1-0628 (Program manager: Dr. David Shifler).

Bibliography

1. Bemrose C.R. and Bridgwater J. A review of attrition and attrition test methods. *Powder Technol.* 49, 97–126 (1987).
2. Lawn B. R., Marshall D. B. Hardness, toughness, and brittleness: an indentation analysis. *Journal of the American Ceramic Society*. 62, 347–350 (1979).
3. Shipway P.H. and Hutchings I.M. Attrition of brittle spheres by fracture under compression and impact loading. *Powder Technol.* 76, 23–30 (1993).
4. Shipway P.H. and Hutchings I.M. Fracture of brittle spheres under compression and impact loading II: Results for lead-glass and sapphire spheres. *Philos. Mag. A.* 67, 1405–1421 (1993).
5. Tavares L.M. and King R.P. Single-particle fracture under impact loading. *Int. J. Miner. Process.* 54, 1–28 (1998).
6. Andrews E.W. and Kim K.S. Threshold conditions for dynamic fragmentation of glass particles. *Mech. Mater.* 31, 689–703 (1999).
7. Salman A.D. and Gorham D.A. The fracture of glass spheres. *Powder Technol.* 107, 179–185 (2000).
8. Schonert K. Breakage of spheres and circular disks. *Powder Technol.*143–144, 2–18 (2004).
9. Salman A.D., Reynolds G.K., Fu J.S., Cheong Y.S., Biggs C.A., Adams M.J., Gorham D.A., Lukenics J., Hounslow M.J. Descriptive classification of the impact failure modes of spherical particles. *Powder Technol.* 143–144, 19–30, (2004).
10. Vogel L. and Peukert W. Breakage behavior of different materials - construction of a mastercurve for the breakage probability. *Powder Technol*. 129, 101–110 (2003).
11. Meier M., John E., Wieckhusen D., Wirth W., Peukert W. Characterization of the grinding behavior in a single particle impact device: Studies on pharmaceutical powders. *Eur. J. Pharm. Sci.* 34, 45–55 (2008).

12. Meier M., John E., Wieckhusen D., Wirth W., Peukert W. Influence of mechanical properties on impact fracture: Prediction of the milling behavior of pharmaceutical powders by nanoindentation. *Powder Technol.*188, 301–313 (2009).

13. Chau K.T., Wei X.X., Wong R.H.C., Yu T.X. Fragmentation of brittle spheres under static and dynamic compressions: Experiments and Analyses. *Mech. Mater*. 32, 543–554 (2000).

14. Wu S.Z.and Chau K.T. Dynamic response of an elastic sphere under diametral impacts. *Mech. Mater.* 38, 1039–1060 (2006).

15. Parab N. D., Claus B., Hudspeth M. C., Black J. T., Mondal A., Sun J., Fezzaa K., Xiao X., Luo S. N., Chen W. Experimental assessment of fracture of individual sand particles at different loading rates. *International Journal of Impact Engineering*. 68, 8-14 (2014).

16. Chen W. W., Hudspeth M. C., Claus B., Parab N. D., Black J. T., Fezzaa K., Luo S. N. In situ damage assessment using synchrotron X-rays in materials loaded by a Hopkinson bar. *Philosophical Transactions of the Royal Society A*. 372: 20130191 (2014).

17. Ghadiri M., and Zhang Z. Impact attrition of particulate solids. Part 1: A theoretical model of chipping. Chemical Engineering Science. 57, 3659–3669 (2002).

18. Zhang Z., and Ghadiri M. Impact attrition of particulate solids. Part 2: Experimental work. *Chemical Engineering Science*. 57, 3671–3686 (2002).

19. Zbib M. B. and Bahr D. F. Fracture Behavior of Granular Polycrystalline Silicon Using Micro-scale and Macro-scale Indentation Techniques. *Metallurgical and Materials Transactions E*. 1, 20-26 (2014).

20. Rosner D. The long struggle to protect workers' lungs against silicosis. *The Milbank Quarterly*. 92, 191-194 (2014).

21. de Castro M. C. S., Ferreira A. S., Irion K. L., Hochhegger B., Lopes A. J., Velarde G. C., Zanetti G., Marchiori E. CT Quantification of Large Opacities and Emphysema in Silicosis: Correlations among Clinical, Functional, and Radiological Parameters. *Lung*. 192, 543–551 (2014).

22. Oliver W.C. and Pharr G. M. J. An improved technique for determining hardness and elastic modulus using load and displacement sensing indentation experiments. *Journal of Materials Research*. 7, 1564–1583 (1992).

23. Morris D. J. and Cook R. F. Radial fracture during indentation by acute probes: I, description by an indentation wedging model. *International Journal of Fracture*.136, 237–264 (2005).

24. Hudspeth M., Claus B., Dubelman S., Black J., Mondal A., Parab N., Funnell C., Hai F., Qi M.L., Luo S.N., Chen W. High speed synchrotron x-ray phase contrast imaging of dynamic material response to split Hopkinson bar loading. *Rev. Sci. Instrum.* 84, 025102:1–025102:7 (2013).

25. Kolsky K. An investigation of the mechanical properties of materials at very high rates of loading. *Proc. Phys. Soc. B.* 62, 676 (1949).

26. Chen W.W. and Song B. Split hopkinson (Kolsky) bar: Design, testing and applications. *Springer, New York*. (2011).

27. Rasband W.S. ImageJ. *U.S. National Institutes of Health, Bathesda, Maryland, USA.*

28. Johnson K.L. *Contact Mechanics*. New York: Cambridge University Press. pp. 90–94 (1985).

CHAPTER 7. CHARACTERIZATION OF SILICON NANOPARTICLES FORMED FROM A FLUIDIZED BED REACTOR AND THEIR INCORPORATION ONTO METAL-COATED CARBON FIBERS

Previously published by The Journal of Mineral, Metals and Materials Society (JOM) , *Volume 66, Isuue 1, in January 2014.*

M.B. Zbib, U. Sahaym, D.F. Bahr

Abstract

Enhancing the light trapping using non-woven arrays of fibers has the potential to improve the photocurrent of silicon solar cells. In this work amorphous and crystalline Si nanopowders (30 – 300 nm) were embedded in carbon fibers and fixed in place with electrodeposited nickel. Scanning and transmission electron microscopy techniques have been used to study the morphology of the Si particles and their interactions with the coatings. Two types of nanoparticles are identified, homogeneous nucleated particles (amorphous particles with some crystalline regions) and attrition particles (mostly crystalline products formed from fracture of particles as they grow in a fluidized bed reactor). Using the Brunauer–Emmett–Teller (BET) technique, the surface area and the pore diameter of these agglomerated Si nanoparticles were calculated to be 6.4 m^2/g and 9.8 nm respectively. After embedding the Si particles into the carbon matrix with the metal coatings the electrical resistivity decreases, suggesting it is possible to enhance the light extraction of silicon solar cells using Si nanoparticles.

7.1. Introduction

The fluidized bed reactor (FBR) is one of the main processes used to manufacture bulk polysilicon for solar cell applications. The two main advantages of growing Si using a FBR instead of the more conventional Siemens' process are that FBR has lower energy consumption and shorter times to produce the same volume of Si. The FBR is a chemical vapor deposition (CVD) method that uses trichlorosilane ($SiHCl_3$, TCS) or silane (SiH_4) gas to grow polycrystalline silicon. The growth occurs at temperatures between 923 and 1023 K, where hydrogen is a main component in the pyrolysis process.

FBR chambers produce two main morphologies of polysilicon, grown granular solids (sizes of mm's in diameter), and nano-powder particles (30-300 nm in diameter) that are either attached to the granules or collected from the chamber filters. Two types of the nanoparticles can be classified, homogeneous nucleated particles and attrition products that are observed to form agglomerates.

Silane and TCS can decompose to form solid silicon in several parts of a reactor. The decomposition can occur on the reactor walls, on pre-seeded particles, or as homogeneous particles. It is critical to keep the flow rates, entrance and exit temperatures controlled to reduce formation of particles on the walls [1], as this material is hard to "harvest" and may influence subsequent temperature profiles in the reactor. Agglomeration of particles often occurs at high silicon deposition rates because the solid mobility is decreased. Other studies have shown that parasitic formation and agglomeration of particles occurs when the initial concentration of Si-containing gasses exceeds some critical value [2]. If the ratio of the mass of the nanoparticles to the total mass is less than 3% and the concentration of silane gas is greater than 20%, then

agglomeration occurs. According to this analysis, nanoparticles formed from homogeneous nucleation of silane. FBRs that are used to produce other types of agglomerate products shows that agglomeration of particles can be affected by material structure within the reactor [3], the particle size of the bed material [4], and the reactor geometry [5].

A new technique that has been recently used for enhancing the photocurrent in silicon solar cells is by inducing nanoparticles into coated composites. This has been demonstrated by surface plasmon resonances in metal nanoparticles to improve light absorption of solar cells [6-10]. The weak absorption areas in silicon can be tolerated by controlling the shape, size, and dielectric environment of the nanoparticles. Hybrid plasmonic antireflection coatings have been used as an efficient light trapping technique to enhance photocurrent in crystalline silicon solar cells [11]. In this case, gold nanoparticles (15 to 150 nm size) were embedded into the SiNx coatings and controlling the distance between the Si photovoltaic layer and the nanoparticles for better light trapping.

Nanoparticles can also be used as enrichment components to improve the performance of electronic devices because of their optical properties and easy manufacturing methods. About 40% of the incident light in silicon is reflected back, and in order to increase the light absorption in silicon, the difference in the refractive indices between the solar cells and the ambient medium should be minimized [12]. Some of the techniques that can be used to reduce surface reflection are, destructive interference coatings [13,14], textured structures as nano-holes and nanowires [15-17].

Si nanoparticles can be embedded in carbon composites as carbon fibers or carbon nanotubes with electrodeposited nickel or copper. This will be discussed in this paper, taking into consideration the morphology of the Si particles and the coatings. Both types of the FBR nano-powders, the homogeneous nucleated particles and the attrition products will be characterized. An experiment of incorporating Si nanopowder into carbon fiber matrix will be also discussed.

7.2. Characterization of FBR Polysilicon Powder Products

7.2.1 Granular Solid

All the Si particles that were examined are provided from the same silane-based FBR manufacturer, and were tested in the condition of as-grown materials. Optical microscopy, scanning electron microscopy (SEM) and transmission electron microscopy (TEM) were used to determine the microstructure of the materials. Fig. 7-1(a) is an optical microscope image showing the cross-section microstructural view of a typical granular Si product, with small pores forming rings. Our research group [18] has proved earlier that granular polysilicon products are almost exclusively crystalline materials as shown in the TEM image in Fig. 7-1b. Fig. 7-1c shows the distribution of pores in the granular Si material where their size in diameter ranges between 0.1 to 5 μm which has been reported previously by our group [18].

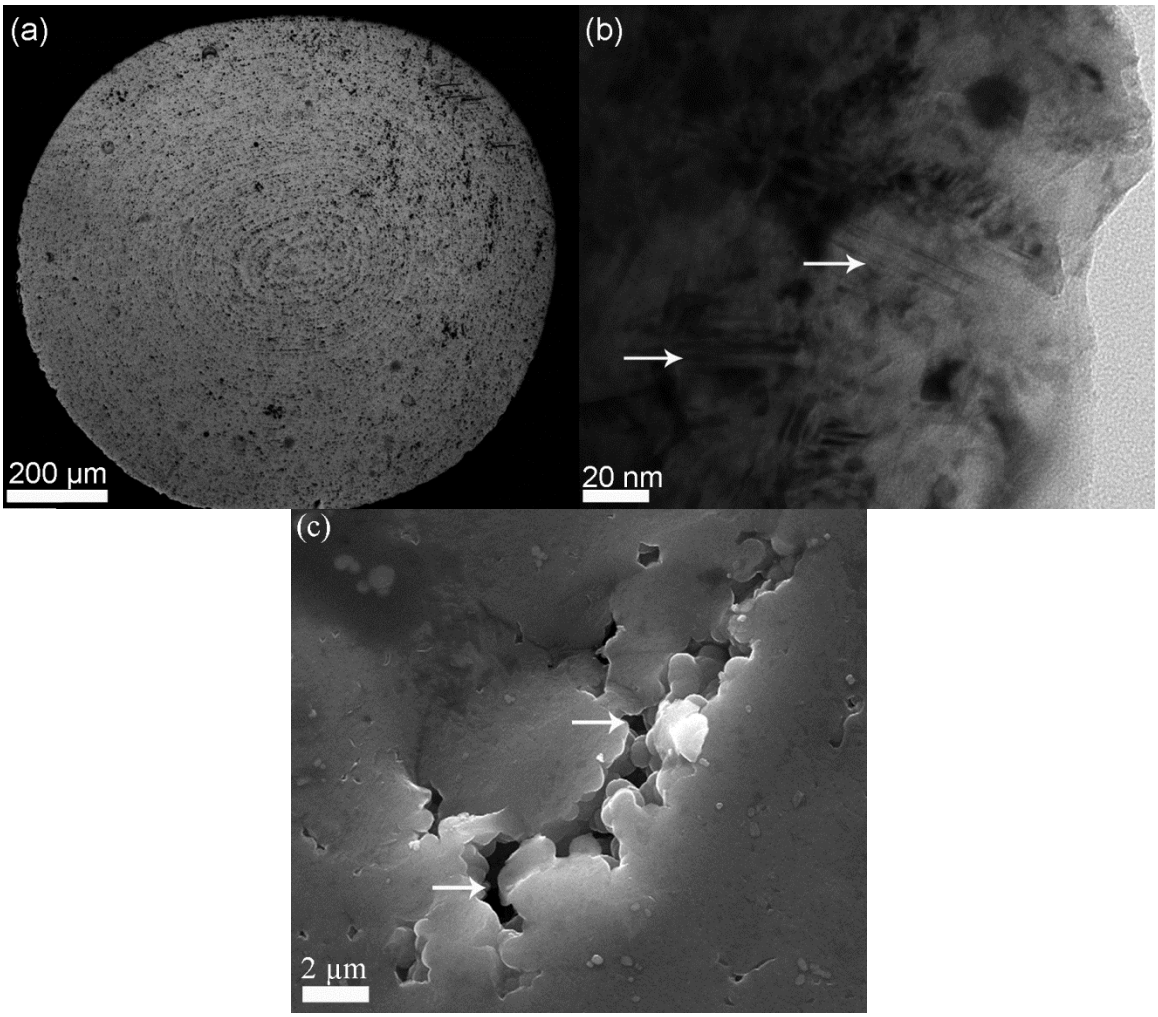

Figure 7-1. (a) Optical microscopy image showing granular FBR Si. (b) TEM image showing the crystallinity of the granular materials (crystalline regions that exhibit twins noted by arrows). (c) SEM image showing the pores (noted by arrows) in the granular Si.

7.2.2 Homogeneous Nucleated Nanoparticles

Nanoparticles grown in the FBR that are found to be homogeneously nucleated are amorphous as shown in the TEM images in Fig. 7-2a and Fig. 7-2b, where they form agglomerates. These amorphous materials are mostly spherical particles as shown in Fig. 7-2c where a typical particle is shown with its corresponding diffraction pattern. Some particles might have crystalline regions and begin to form non-spherical structures, as

shown in Fig. 7-2d along with the diffraction pattern from this particular Si particle. The particles were collected from the gas exit and filters of a commercial FBR. We have previously shown that the amorphous silicon particles can crystallize when heated to temperatures over 940 K [18].

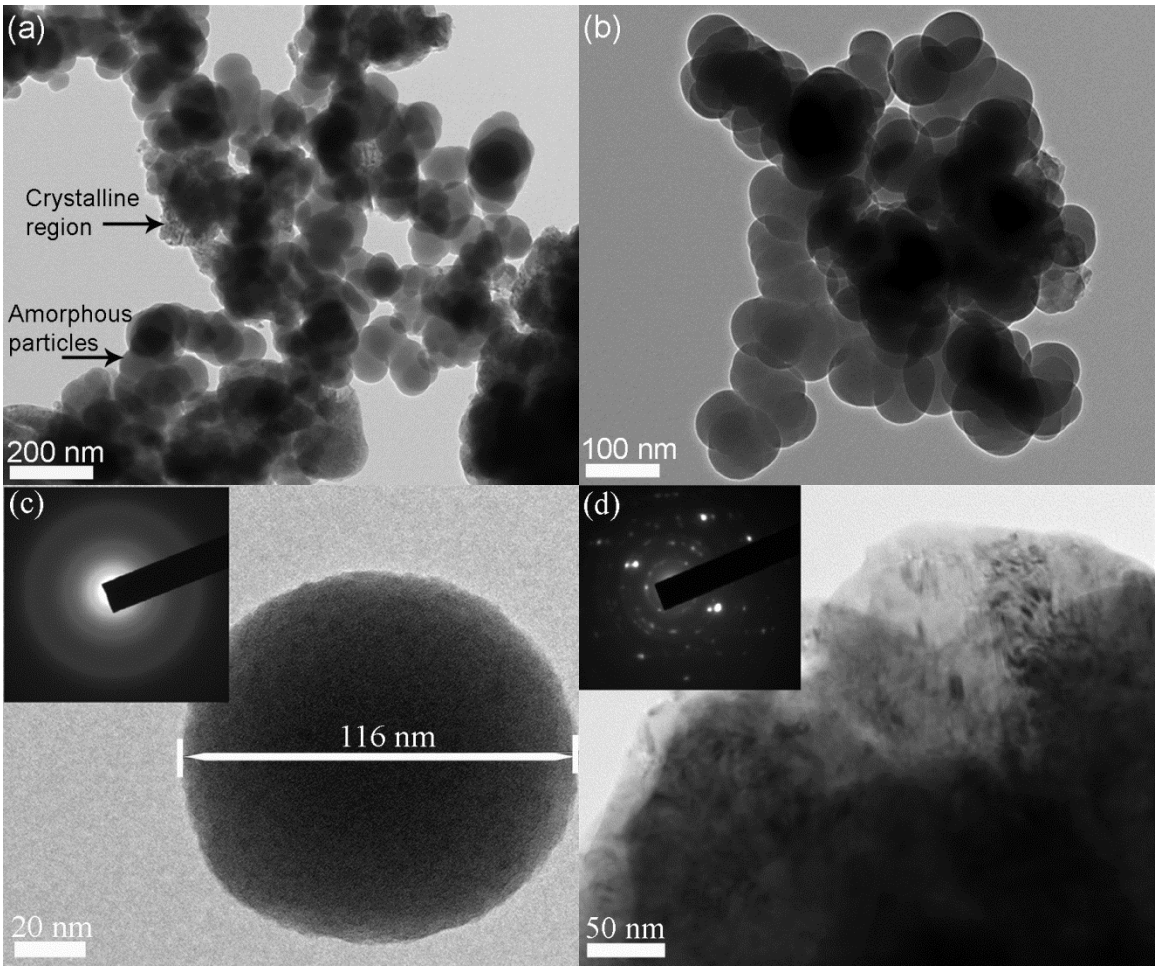

Figure 7-2. TEM images of the homogeneously nucleated nano Si particles. (a) Typical distribution of amorphous particles with some crystalline regions. (b) A different size distribution of amorphous particles and agglomerates from the same growth run. (c) Nano Si particle with its corresponding diffraction pattern showing that it is amorphous. (d) Another Si particle where its diffraction pattern shows it is crystalline.

The size distribution of the homogeneous nucleated nanoparticles can vary depending on the production process that can be controlled by certain parameters, as

temperature and time. The overall average diameter from the commercial system collected here was measured to be 120 nm. However, because the particles agglomerate, the surface area of the units which would incorporate into a coating would effectively have a different surface area than if the particles were isolated individually. Therefore, Brunauer–Emmett–Teller (BET) technique was used to determine the surface area and the pore size of the homogeneously nucleated nano Si. The pore size in agglomerated nano Si represents the ability of the particles to interact together; it is effectively a measurement of the open spaces in the agglomerates and to first order reflects how well agglomerated the structures are. Large pores and surface areas mean the agglomerates are open and only loosely connected, while smaller effective pores means the agglomerates are more densely packed. The nano Si powders were put in a glass tube and tested in a nitrogen gas tank that is heated to a temperature of 473 K, and the measurements were done using the a TriStar 3000 system. The BET surface area and the pore diameter were measured to be 6.4 m^2/g and 9.8 nm. The average pore diameter matches with overall distribution of the particle and pore sizes shown in Fig. 7-2; both images show porosity on the order of 10 nm in between individual particles. This suggests that using BET provides a relatively rapid sampling method that correlates well to the more time consuming TEM studies. The average overall agglomerate size in the homogeneous nucleated nanoparticles is approximately 1 μm.

7.2.3. Nanoparticles Formed via Attrition

Fig 7-3. shows nano Si spherical particles and angular-shaped particles. The spherical particles are mostly amorphous, as shown in Fig. 7-3a, with an average diameter of 95 nm. A small number of the spherical particles are crystalline, as shown in

Fig. 7-3b, with an average diameter of 150 nm. Our group previously showed that amorphous nanopowders can crystallize at temperatures within the process window [18]. This suggests that the crystalline spherical particles may have encountered a region of the reactor that was at a higher temperature during the growth process in the FBR chamber. However, the angular-shaped particles have crystalline regions with an average size substantially larger than 300 nm, and their morphology is reminiscent of a fracture specimen. These angular-shaped particles exhibit twinning and grain sizes similar to as-grown material shown in Fig 7-1b, suggesting that this type of angular-shaped nano Si particles are attrition products due to fracture during growth.

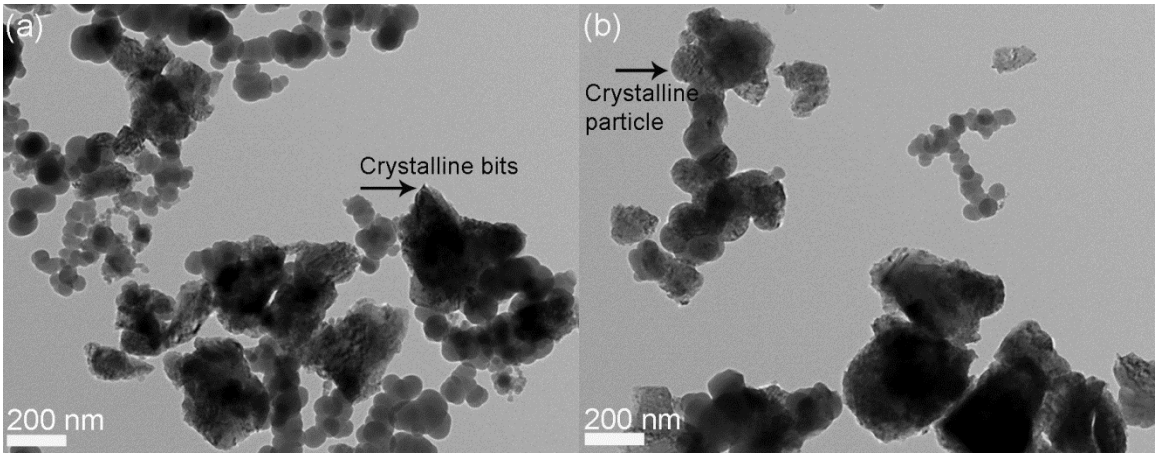

Figure 7-3. TEM images showing the distribution of the attrition particles (mostly amorphous particles with some crystalline particles). (a) The label "bits" refers to a product of attrition, with an angular shape, (b) while the "particle" is likely a formerly amorphous particle that has crystallized during processing. The key differences are particle morphology, internal twin density, and the overall size distribution.

7.3. Incorporating Nano Si Powder Into Metal-Coated Carbon Fibers (CFs)

One of the ways to enhance photocurrent in silicon based solar cells is by incorporating nanoparticles into composites; there are many reports of this in the literature. A few examples include one case in which Si particles that have been obtained

from solid Si waste of organosilane industry were used with graphite microspheres as high capacity anodes for Li-ion batteries [19]. Other examples include the pairing of carbon nanotubes/Si composites that were obtained by growing coiled carbon nanotubes on Si particles (using a CVD process); these systems showed good electric contact performance during cycling [20]. Another example of a nano Si composite has been demonstrated by mixing pure nano Si (78 nm diameter spheres) and carbon black as high capacity anodes where Si powders were manufactured by laser induced silane gas reaction [21].

Our experiment used the homogeneous nucleated nano Si particles that were embedded into commercial carbon fiber (CF) composites that have been electroplated with Ni. Prior to plating, CFs were separated manually from tows used for composite manufacturing, baked for 20 minutes at 673 K, and then boiled in a solution of 40% nitric acid and 60% DI water for 40 minutes. The CFs were placed into a loosely packed bed of nano Si particles, removed, and then the separated tows were suspended in a Watts bath solution at pH 4 (Ni Watts bath contents in [22]), and Ni was plated onto the CF at room temperature. A Ni sheet was used as the anode, and the current was controlled to deposit a nominally sub-1000 nm thick Ni coating in an effort to surround, but not completely cover, residual nano Si particles that would adhere to the CF.

Fig. 7-4. shows an SEM image of the agglomerates of the silicon particles along the Ni-coated CFs, with an average agglomerate size of 1 μm. This size is similar to the size of agglomerates that were shown in Fig. 7-2b and Fig 7-3. where the structure can be identified. The Si was able to adhere to the CF, and some particles remain during the electroplating process as they are partially embedded in the plating. The electrical

resistivity of the Ni-coated CFs was measured after embedding them with nano Si. The measurements were taken when the samples were exposed to light. Our preliminary results show that the average electrical resistance of Ni-coated CFs is 0.4 Ω and for the non-coated CFs is 0.8 Ω using a simple two point probe. The electrical resistivity of the Ni-coated CFs locally changes depending on the distribution of the Si agglomerates on the composite, leading to relatively large scatter in these preliminary measurements. Samples with a relatively uniform distribution of nano Si particles showed electrical resistivity lower than 0.4 Ω, suggesting it is possible to enhance light extraction of silicon solar cells using these Si nanoparticles, due its moderate surface area.

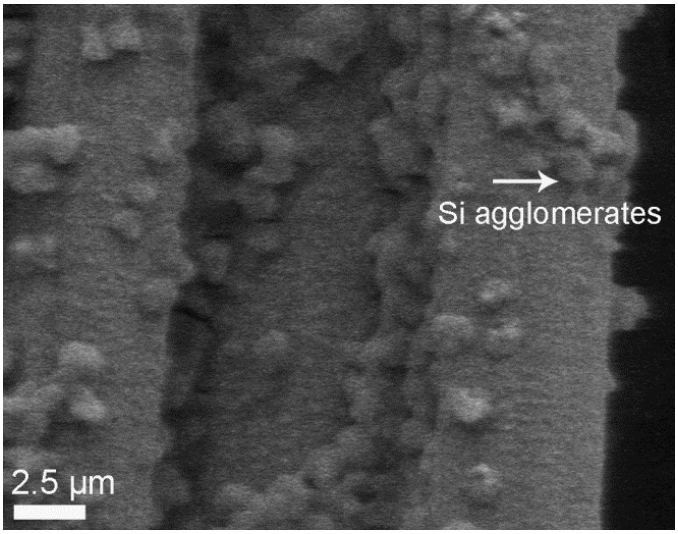

Figure 7-4. SEM images showing Si agglomerates (~1µm) along the Ni-coated carbon fibers.

7.4. Conclusions

Two types of silicon nanoparticles (30-300 nm) that form in an FBR have been identified, homogenous nucleated nanoparticles (spherical amorphous particles with some crystalline regions), and attrition agglomerates (spherical amorphous particles with larger, non-uniform crystalline particles within the agglomerate). These agglomerated Si

nanoparticles can be embedded into nickel-coated carbon fibers; this has been demonstrated using a composite electroplating method as a new technique in enhancing the photocurrent of silicon solar cells. Improving the uniformity of the nano Si particles distribution along the CFs appears to lower the electrical resistivity of the composite. Future work will include more measurements of the photocurrent of the metal-coated composites embedded with nano Si particles.

Acknowledgments

We would like to thank REC Silicon, Moses Lake WA, for providing the Si materials. Also, we thank MM Dahl for some of the microscopy images shown in this paper.

Bibliography

1. Kato K., and Wen C.Y. Bubble assemblage model for fluidized bed catalytic reactors. *Chem Eng Sci* 24, 1351-1369 (1969).
2. Caussat B., Hemati M., Couderc J.P. Silicon deposition from silane or disilane in a fluidized bed-Part I: Experimental study. *Chemical Engineering Science.* 50, 3615-3624 (1995).
3. Nijenhuis J., Korbee R., Lensselink J., Kiel J.H.A, van Ommen J.R. A method of agglomeration detection and control in full-scale biomass fired fluidized beds. *Chem Eng Sci*. 62:644-654 (2007).
4. Ohman M, & Nordin A.A New method for quantification of fluidized bed agglomeration tendencies: A sensitivity analysis. *Energy Fuels* 12, 90-94 (1998).
5. Chirone R., Miccio F., Scala F. Mechanism and prediction of bed agglomeration during fluidized bed combustion of a biomass fuel: Effect of the reactor scale. *Chem Eng J.* 123, 71-80 (2006).
6. Atwater H. A. & Polman A. Plasmonics for improved photovoltaic devices. *Nature Mater*. 9, 205-213 (2010).
7. Matheu P., Lim S.H., Derkacs D., McPheeters C., Yu E. T. Metal and dielectric nanoparticle scattering for improved optical absorption in photovoltaic devices. *Appl. Phys. Lett*. 93, 113108-1 – 113108-3 (2008).
8. Chen X., Jia B., Saha J. K., Cai B., Stokes N., Qiao Q., Wang Y., Shi Z., Gu M. Broadband enhancement in thin-film amorphous silicon solar cells enabled by nucleated silver nanoparticles. *Nano Lett*. 12, 2187-2192 (2012).
9. Spinelli P., Hebbink M., de Waele R., Black L., Lenzmann F., Polman A. Optical impedance matching using coupled plasmonic nanoparticle arrays. *Nano Lett*. 11, 1760-1765 (2011).

10. Pillai S., Catchpole K. R., Trupke T., Green M. A. Surface plasmon enhanced silicon solar cells. *J. Appl. Phys*. 101, 093105-1 – 093105-8 (2007).

11. Fahim N., Ouyang Z., Jia B., Zhang Y., Shi Z., Gu M. Enhanced photocurrent in crystalline silicon solar cells by hybrid plasmonic antireflection coatings. *Appl. Phys. Lett.* 101, 261102-1 – 261102-5 (2012).

12. Fang C.Y., Liu Y.L., Lee Y.C., Chen H.L., Wan D.H., Yu C.C. Nanoparticle stacks with graded refractive indices enhance the omnidirectional light harvesting of solar cells and the light extraction of light-emitting diodes. *Adv. Funct. Mater.* 23, 1412–21 (2013).

13. Lee S.H., Lee I., Yi J. Silicon nitride films prepared by high-density plasma chemical vapor deposition for solar cell applications. *Surf. Coat. Technol*. 153, 67-71 (2002).

14. Nagel H., Aberle A.G., Hezel R. Optimised Antireflection coatings for planar silicon solar cells using remote PECVD silicon nitride and porous silicon dioxide. Prog. Photovoltiacs.7, 245-60 (1999).

15. Peng K.Q., Wang X., Li L., Wu X.L., Lee S.T. High-Performance Silicon Nanohole Solar Cells. *J. Am. Chem*. Soc.132, 6872-6873 (2010).

16. Xi J.Q., Kim J.K., Schubert E.F. Silica nanorod-array films with very low refractive indices. *Nano Lett.* 5, 1385-87 (2005).

17. Kelzenberg M.D., Boettcher S.W., Petykiewicz J.A., Turner-Evans D.B., Putnam M.C., Warren E.L., Spurgeon J.M., Briggs R.M., Lewis N.S., Atwater H.A. Enhanced absorption and carrier collection in Si wire arrays for photovoltaic applications *Nat. Mater*. 9, 239-44 (2010).

18. Zbib M.B., Dahl M.M, Sahaym U., Norton M.G., Osborne E.W., Bahr D.F. Characterization of granular silicon, powders, and agglomerates from a fluidized bed reactor. *Journal of Materials Science.* 47, 2583–2590 (2012).

19. Yu J., Zhan H., Wang Y., Zhang Z., Chen H., Li H., Zhong Z., Su F. Graphite microspheres decorated with Si particles derived from waste solid of organosilane industry as high capacity anodes for Li-ion batteries. *J. Power Sources.* 228, 112-119 (2013).

20. Shu J., Li H., Yang R., Shi Y., Huang X. Cage-like carbon nanotubes/Si composite as anode material for lithium ion batteries. *Electrochem. Commun*. 8, 51-54 (2006).

21. Li H., Huang X.J., Chen L.Q., Wu Z.G., Liang Y. A high capacity nano-Si composite anode material for lithium rechargeable batteries. *Electrochem. Solid-State Lett.* 2, 547-549 (1999).

22. Arghavanian R. and Parvini-Ahmadi N. The effect of co-electrodeposited ZrO2 particles on the microstructure and corrosion resistance of Ni coatings. *J Solid State Electrochem*. 15, 2199–2204 (2011).

CHAPTER 8. CONCLUSIONS

This thesis focused on characterizing the microstructure and studying the effects of solute hydrogen on fracture toughness of polycrystalline granular silicon grown with a commercial FBR. Based on these analyses new attrition parameters were identified to better understand the fracture behavior of silicon and other brittle materials. Si nanopowders were incorporated with carbon composites for new applications. New testing methods were developed to assess the mechanical properties of granular materials that are difficult or impossible to test in conventional ASTM-approved geometries.

Granular polysilicon grown in current commercial FBR reactors is mostly crystalline with some amorphous regions near small pores, where porosity ranges between 1-4 volume percent. The crystallite sizes reach up to 250 nm with the presence of high twin density. The Si nanopowders collected in the filtration system during growth are mainly amorphous spherical particles with an average diameter of 80 nm (range between 30-300 nm) and they form agglomerates that can reach up to 10's of μm in size. There is some crystalline particulate matter that co-agglomerates with the amorphous nanopowders; these particulates are larger than the nanopowders and have non-uniform shapes. Based on the microstructural observations it was suggested that the primary growth mechanism of the granular Si from FBR is CVD occurring on the surface of the granule with minor agglomeration around small pores. The amorphous nanopowders can crystallize when

annealing to 650 °C, with no significant changes in particle size. The crystalline regions in agglomerated nanopowders are most likely formed from fracture and chipping of the granular material during processing.

It was found that solute hydrogen has a significant effect on the fracture toughness of granular polysilicon. When the amount of solute hydrogen decreases, the toughness value increases. Also, the crystallite size is inversely related to the toughness. Reducinghydrogen in the production and increasing the crystallite size can result in a better toughness of FBR silicon. Hydrogen can be reduced by annealing the polysilicon at temperatures at or above 1000°C, where the toughness of the final product is increased up to 43%. These results are important for the polycrystalline and solar cell industries when handling and transporting their materials.

Testing the fracture behavior of polysilicon using both micro-scale (Vickers) and macro-scale (Rockwell) indentation techniques resulted in similar behavior. High toughness polysilicon (0.86 $MPa.m^{0.5}$) were able to withstand up to 60 kg load, and low toughness polysilicon (0.6 $MPa.m^{0.5}$) were able to withstand up to 45 kg load. Microstructural analysis showed that the presence of pores does not influence the crack morphology and the fracture behavior of polysilicon in micro-scale or macro-scale analyses. Using a simple technique as the Rockwell hardness test is an efficient qualitative technique to get a rapid assessment of the quasi-static fracture behavior of polysilicon, and other brittle granular materials.

A new dimensionless attrition propensity parameter (ή) was developed in order to better understand the quasi-static fracture behavior of polysilicon. This parameter is defined as

$$\acute{\eta} = \frac{lH^2}{T^2} \qquad \text{(Eq. 8-1)}$$

where l is the diameter of the granular silicon, H is the measured hardness, and T is the calculated fracture toughness. The ή term is used to indicate the likelihood of a given lot of material to generate dust and particulate matter during handling at quasi-static conditions (such as during shipping or during pouring or filling containers). Polysilicon with a lower toughness has a higher attrition parameter, and smaller sized granular Si shows lower attrition parameter.

Another attrition parameter was proposed to have a relationship between fracture mechanisms under high speed impact testing and mechanical properties of brittle microshperes, and to suggest possible morphologies of the fracture process. This model is represented by pulverization parameter ($\mathcal{P}$) that is related to the hardness (H), elastic modulus (E), fracture toughness (T), and the size (d) of the particles assuming a fixed grips loading condition with excess loads applied. It is identified as

$$\mathcal{P} = \frac{Hd}{TE^{5/3}} \qquad \text{(Eq. 8-2)}$$

Three different failure mechanisms were identified based on the pulverization model. These mechanisms are defined as pulverization, major cracking, and single cracking for high, medium, and low $\mathcal{P}$ values respectively. This model is shown to predict failure morphology after high strain rate loading of spherical particles.

A new demonstration was done on using the by-products of FBR growth, Si nanopowders, in new markets rather than being waste materials. The agglomerated Si nanoparticles were embedded into nickel-coated carbon fibers, using electroplating

method as a new technique in enhancing the photocurrent of silicon solar cells. The silicon particles were able to adhere to the carbon composites forming agglomerates of sizes ~1 μm. The coated CFs showed better electrical resistivity compared to the non-coated ones. The uniformity of the distribution of the nano Si particles along the CFs appears to lower the electrical resistivity of the composite. This suggests that nano-Si powders may be incorporated into other fibrous, woven, or mat-like structures of future solar cell geometries. To use these nano Si powders more efficiently in the solar market, further investigation and analysis should be done. Currently, it is unlikely to use such nanopowders because they exhibit relatively high amount of silicon oxide compared to granular materials. Future analysis could include reducing the amount of oxides on the powders to make them more valuable materials.

VITA

VITA

MOHAMAD B. ZBIB

Originally from Lebanon, Mohamad came to the U.S. in January 2008 where he earned a B.S. degree in Materials Science and Engineering from Washington State University (Pullman, WA) in May 2011. He started Ph.D. immediately after his B.S. at the same school. Then he decided to move to Purdue University (West Lafayette, IN) with his adviser Dr. David Bahr, in January 2013, and continued the Ph.D. program in the School of Materials Engineering. The research work focused on characterizing polycrystalline silicon used for solar cell applications using structural, mechanical and chemical analysis. He also proposed different attrition parameters that relate the fracture behavior to materials properties. Other projects included processing new carbon-composite and steel composite materials using electro-deposition for mechanical, electrical and magnetic applications.